FINAL REPORT

STABILITY ENHANCING MEASURES FOR WEAK GRIDS STUDY

https://www.monash.edu/energy-institute/grid-innovation-hub/home/stability-enhancing-project

Organisation:

Monash University - Grid Innovation Hub

Authors:

Dr Behrooz Bahrani
Dr Nabil Mohammed
Dr Mohammad Hasan Ravanji
Dr Weihua Zhou
Dr Milad Zarif Mnasour
Dr Sajjad Hadavi
Dr Dayan Rathnayake
Mr Si Phu Me

10 March 2023

DISCLAIMER:

ACKNOWLEDGEMENT:

This project received funding from the Australian Renewable Energy Agency (ARENA) as part of ARENA's Advancing Renewables Program. Grant number: 2020/ARP007.

The project was conducted with the collaboration of the following partners, which their assistance is acknowledged and appreciated:

List of Acronyms

ACC	Alternating Current Control
APC	Active Power Controller
AdVR	Adaptive Virtual Resistor
AEMO	Australian Energy Market Operator
AR	Admittance Representation
ARENA	Australian Renewable Energy Agency
AVR	Automatic Voltage Regulator
AVSG	Adaptive Virtual Synchronous Generator
BESS	Battery Energy Storage Systems
CGVSG	Compensated Generalised Virtual Synchronous Generator
CC	Current Control
CCM	Component Connection Method
DS-PSGFLI	Double-Synchronous-Reference-Frame-based Power-Synchronised Grid-Following Inverter
EMT	Electro-Magnetic Transient
ePSGFLI	Enhanced Power-Synchronised Grid-Following Inverter
ERCOT	Electric Reliability Council of Texas
FFT	Fast Fourier Transform
FVR	Fixed-value Virtual Resistor
FRD	Frequency Response Data
FRT	Fault Ride-Through
GCM	Grid-Connected Mode
GFMI	Grid-Forming Inverter
GNC	Generalized Nyquist Criterion
GFLI	Grid-Following Inverter
GIE	Grid Impedance Estimation
GSC	Grid-Side Converter Controller
GVSG	Generalised Virtual Synchronous Generator
HVRT	High-Voltage Ride Through
IBR	Inverter-Based Resource
IEEE	Institute of Electrical and Electronics Engineers
LCL	Inductor-Capacitor-Inductor
LMI	Linear Matrix Inequality

LPV-PSGFLI	Linear Parameter-Varying Controlled Power-Synchronised Grid-Following Inverter
LTI	Linear Time-Invariant
MPTC	Maximum Power Transfer Capability
MSC	Machine-Side Converter Controller
MSMC	Machine-Side Master Controller
NEM	National Electricity Market
NSP	Network Service Provider
OMPC	Optimization-based Multivariable Primary Controller
OCC	Output Capability Curve
OEM	Original Equipment Manufacturer
PAC	Pitch-Angle Controller
PCC	Point of Common Coupling
PEC	Power Electronic Converter
PI	Proportional Integral
PLL	Phase-Locked Loop
PMSG	Permanent-Magnet Synchronous Generator
PoC	Point of Connection
PPC	Power-Plant Controller
PRBS	Pseudo-Random Binary Sequence
PSGFLI	Power-Synchronised Grid-Following Inverter
PWM	Pulse-Width Modulation
RPC	Reactive Power Controller
RER	Renewable Energy Resource
REZ	Renewable Energy Zone
RMS	Root Mean Square
RoCoF	Rate of Change of Frequency
SCR	Short-Circuit Ratio
SDP	Semi-Definite Program
SI	Stability Index
SSM	Small-Signal Model
SSO	Sub-Synchronous Oscillation
SSR	State-Space Representation
SM	Standalone Mode

SMIB	Single Machine Infinite Bus
STATCOM	STATic synchronous COMpensator
SynCon	Synchronous Condenser
SRF	Synchronous Reference Frame
SRF-PLL	Synchronous Reference Frame Phase-Locked Loop
TNSP	Transmission Network Service Provider
VID	virtual Inductor-based Decoupling
VR	Virtual Resistor
VSC	Voltage Source Converter
VSG	Virtual Synchronous Generator

Executive Summary

Australia's power system is undergoing a significant transformation, with anticipated thermal generation retirements and a rise in renewable Inverter-Based Resource (IBR)s. Many regions in the National Electricity Market (NEM) are experiencing system strength-related problems, which are likely to worsen in the coming years. The rapid growth of IBRs also has tangible commercial impacts on operating generators, as some areas with high IBRs share see connection delays or curtailment.

To assist both network owners and operators in ensuring customers get the maximum value from the renewable solar and wind farms located in weak parts of the grid, and increase the reliability and security of the grid in such areas, Australian Renewable Energy Agency (ARENA) funded a two and a half year project, entitled "Stability Enhancing Measures for Weak Grids Stud". The project, led by Monash University, had three partners: Australian Energy Market Operator (AEMO), Hitachi Energy, and AusNet Services. It also had a larger stakeholder reference group with many industry partners who were involved in quarterly meetings. The total budget was $559k from ARENA and $160k cash from Monash University, with the main partners contributing $641k in-kind combined.

Three post-doc researchers and four Ph.D. students conducted extensive desktop research dividing the project into three main tasks: 1) Weak Grids Classification and Test-bed Development, 2) Grid-Strengthening-based Solutions: Synchronous Condenser (SynCon)s and Grid-Forming Inverter (GFMI)s, and 3) Internal Control of Wind/Solar Farms and their Interactions with other Power Electronic Converter (PEC)-Connected Assets, to characterise system strength problems and assess a variety of design, control scheme and configuration solutions. Several key innovations are developed in this project to ensure reliable operation of IBRs and maintain the stability of weak-grid-connected wind and solar farms under various conditions. These innovations are categorized into four groups: SynCons, Grid-Following Inverter (GFLI)s, Power-Synchronised Grid-Following Inverter (PSGFLI)s and GFMIs.

For the first category, SynCons, the project proposes optimal sizing and allocation of SynCons based on heuristic optimization algorithms and mixed-integer convex optimization. This aims to maintain Short-Circuit Ratio (SCR) in the system greater than pre-defined values, while minimizing the investment and operation costs of SynCons, and voltage deviation in the system. Additionally, a robust exciter controller design for SynCons in weak grids is proposed.

The second category, GFLIs, involves several key innovations. Firstly, a nonlinear control method for assessing system stability is proposed, providing system planners and operators with better insights on their system stability status. Secondly, a new system strength index is developed to address SCR index shortcomings. Thirdly, a nonlinear controller is proposed to expand the traditional Phase-Locked Loop (PLL)s capabilities, enabling the connection of renewables in very weak grids. Additionally, the project presents two comprehensive studies on the output capability curves and admittance modeling of GFLIs, followed by designing auxiliary controllers (e.g., passivation design) to maximize their maximum transferable power.

The third category introduces the innovative PLL-less control structure called PSGFLIs, enabling seamless operation of GFLIs in both strong and weak grids without being prone to instability. Three different control strategies are developed for tuning the outer power controller parameters of the PSGFLIs: Optimized-based control strategy, First-order linear parameter-varying-based control strategy, Second-order linear parameter-varying-based control strategy. Furthermore, the positive-negative control strategy for the PSGFLIs is proposed to enhance the reliable and stable operation during asymmetrical faults/unbalanced grid voltage events.

Lastly, the fourth category presents several innovations for GFMIs to enhance their operation in various grid conditions. First, an adaptive-based control method for the Virtual Synchronous Generator (VSG)-Based GFMIs is proposed to permit accurate control, meeting the desired/pre-defined dynamic performance regardless of the grid strength (strong vs weak) or type (inductive vs resistive). Second, a novel controller for GFMIs, namely Compensated Generalised Virtual Synchronous Generator (CGVSG), is proposed to achieve low overshoot and short settling time in step response in the Grid-Connected Mode (GCM) while adhering to the Rate of Change of Frequency (RoCoF) relay limit in the Standalone Mode (SM). Third, a convex optimization-based and a novel discrete-time multivariable controller methods are proposed to enhance damping and virtual inertia and to completely decouple the active and reactive loops, respectively. Fourth, the project studies thoroughly the concept of upgrading Type 4 grid-following wind turbine generators to operate in the grid-forming mode by developing the required control blocks. Lastly, an adaptive virtual resistor method is proposed for GFMIs to enhance the damping of post-fault oscillations and smoothing fault recoveries, which is robust against changes in the grid condition.

The outcomes of this project include increased penetration of solar/wind farms, maximized generation capacity of existing wind/solar farms located in weak parts of the grid, and increased reliability, security, and stability of the grid as the renewable energy penetration grows. Overall, this project has contributed significantly to the renewable energy industry by providing solutions to the stability issues faced by renewable energy farms in weak grids. The research activities have led to a number of journal and conference publications, and the outcomes of this project contribute to the Advancing Renewables Program's outcomes.

The project was conducted mainly as an R&D project, and the risk of non-completion was low. However, the COVID-19 pandemic posed challenges in hiring the right staff and researchers for the project, which caused a delay in the beginning. Despite the challenges, the project successfully identified the stability issues faced by renewable energy farms in weak grids and proposed add-on solutions to maintain their stability.

This project was mainly focused on GFLIs/GFMIs control design and SynCons control/placement. However, with the increasing number of IBRs in the NEM, the risk of interactions between various IBRs and other grid components is increasing, leading to low-frequency oscillations, particularly in weak parts of the network. By leveraging the knowledge and expertise that the Grid Innovation Hub created during this project and to address low-frequency oscillations in multiple-inverter systems, one promising area for future research is the development of tools and methodologies aimed at identifying root causes and developing effective solutions. Such solutions may include tools for identifying the primary root causes of such oscillations by employing several techniques and developing various user-friendly time-domain and frequency-domain simulation tools, and providing various solutions for mitigating the oscillations, such as developing novel controllers for IBRs.

This final report presents the key findings during this project in four different themes: SynCons, GFLIs, PSGFLIs, and GFMIs. The following table gives an overview of the project. Although this project was originated from challenges and difficulties in the West Murray Region, the project findings and the developed concepts are applicable to any weak area of the NEM.

Project Title	Stability Enhancing Measures for Weak Grids Study
Start date	18 June 2020
End date	10 March 2023
Budget	$559k Funded by ARENA - $1.36m Total project cost
ARENA Program	Advancing Renewables Program
Lead Organisation	Monash University
Project Partners	AusNet Services, Australian Energy Market Operator (AEMO), Hitachi Energy (formerly Hitachi ABB)
Audience	AEMO, Original Equipment Manufacturer (OEM)s, Consultants, and Transmission Network Service Provider (TNSP)s
Team Members	Dr Behrooz Bahrani (Senior Lecturer – Team Leader) Dr Mohammad Hasan Ravanji (Post-doc Research Fellow) Dr Nabil Mohammed (Post-doc Research Fellow) Dr Weihua Zhou (Post-doc Research Fellow) Dr Gamini Jayasinghe (Post-doc Research Fellow) Dr Dayan B. Rathnayake (PhD Student) Dr Sajjad Hadavi (PhD Student) Dr Milad Zarif Mansour (PhD Student) Mr Si Phu Me (PhD Student)
Main Outcomes	1. increased penetration of solar/wind farms in particular in weak parts of the networks unlocking future investments, 2. maximized generation capacity of existing wind/solar farms located in weak parts of the grid, and 3. increased reliability/security/stability of the grid as the renewable energy penetration grows.
Publications	Research articles have been published in Institute of Electrical and Electronics Engineers (IEEE) journals in: • IEEE Transactions on Power Systems, • IEEE Transactions on Power Electronics, • IEEE Transactions on Sustainable Energy, • IEEE Transactions on Energy Conversion, • IEEE Transactions on Power Delivery, • IEEE Journal of Emerging and Selected Topics in Power Electronics, • IEEE Journal on Emerging and Selected Topics in Circuits and Systems, • IEEE Access

Contents

1 Introduction

This ARENA-funded project "Stability Enhancing Measures for Weak Grids Study" began in June 2020 and was led by Monash University with the collaboration of AEMO, AusNet Services and Hitachi Energy as the project partners. Three post-doc researchers and four Ph.D. students conducted extensive research to address the three main tasks of this project: 1) Weak Grids Classification and Test-bed Development, 2) Grid-Strengthening-based Solutions: SynCons and GFMIs, and 3) Internal Control of Wind/Solar Farms and their Interactions with other PEC-Connected Assets. This final report presents the work carried out during this project in relation to the above-mentioned three tasks.

1.1 Background

Australia is one of the leading countries in the field of renewable energy integration over the last two decades. As a result, the Australian grid is undergoing a major transformation where fossil fuels such as coal-fired power stations are being replaced by renewable energy resources such as solar and wind. However, three major concerns for increasing renewable energy penetration are associated with weak grid integration. First, the Australian electricity grid is a radial and very long network, making it difficult for the meshed and interconnected networks which increase grid stability and reliability. Second, the optimal locations of several of the renewable energy resources (e.g., solar farms) are located in weak areas of the grid and far from load centres, posing various stability problems to the Australian NEM. Finally, the extensive integration of renewable energy resources using GFLIs and fast pace retiring of synchronous generators further intensify associated problems with weak grid integration, especially for large-scale solar and wind farms.

1.2 Project Outcomes & Outputs

1.2.1 Project Outputs

The main outputs and industrial impacts of this project are

- installing SynCons based on Network Service Provider (NSP)s, Renewable Energy Zone (REZ)s, or NEM point of view instead of project-based SynCons installation,
- considering committed and upcoming projects for the SynCon installation planning,
- considering pre-full impact assessment studies with the installed SynCons,
- collaborating with OEMs of SynCons and other strengthening assets like STATic synchronous COMpensator (STATCOM) to update their models and controller based on NSPs, REZs, and NEM issues,
- considering the impact of X/R ratio and impedance-based stability analysis instead of using only SCR,
- developing a nonlinear control method for assessing the system stability, domain of attraction, etc. that provides the system planners and operators with better insights on their system stability status,
- developing a new system strength index (Disturbance Tolerance) to address the SCR index shortcomings,
- developing a nonlinear controller to expand traditional PLLs capabilities and enable the connection of renewables in very weak parts of the network,

- quantifying the impact of network-caused limitation (grid strength) and IBR-caused limitation (IBR control system) on the maximum transferable power of GFLIs and GFMIs by using output capability curves,
- proposing an auxiliary controller for GFLI inverters to maximise their maximum transferable power considering their thermal limit,
- investigating the benefits of PLL re-tuning, PLL passivation technique, and employing PLL-less control structures to enhance GFLIs' maximum transferable power,
- comprehensively deriving the Small-Signal Model (SSM)s including the state-space models and admittance models of eleven commonly-adopted GFLIs,
- comparatively analysing the effects of the GFLIs inner current and outer power control bandwidths on the maximum allowable power injection, which pointed out that large current and power bandwidths help improve the small-signal stability,
- developing a PLL passivation module, which can stabilise the GFLI under weak grids, high active power output, and large PLL bandwidth,
- proposing the single-node-based multiple-node impedance measurement method, which can release the computational burden and is cost-effective,
- proposing an innovative PLL-less control structure called PSGFLIs, which enables seamless operation of GFLIs in both strong and weak grids without being prone to instability. Three different control strategies are developed for tuning the outer power controller parameters of the PSGFLIs. Furthermore, a control strategy is proposed to enable reliable and stable operation of the PSGFLI during asymmetrical faults/unbalanced grid voltage events. The developed four control strategies for PSGFLIs are as below:
    - Optimized-based control strategy,
    - Linear parameter-varying-based control strategy,
    - Enhanced frequency control strategy,
    - Double-synchronous-reference-frame-based control strategy,
- proposing an Adaptive Virtual Synchronous Generator (AVSG) control based on online grid impedance estimation to permit accurate control of the VSG by mitigation of the inherent power coupling. The control parameters of the primary control loop of the AVSG are being adaptively tuned to meet the desired/pre-defined dynamic performance (e.g., settling time and damping) regardless of the grid strength (strong vs weak) or type (inductive vs resistive),
- implementing an online event-based grid impedance estimation technique into the control loop of the AVSG, enabling the AVSG to estimate the real values of the grid impedance without the need for additional hardware and reducing the associated impacts on power quality,
- a comprehensive review paper on the latest developments in grid-forming inverter modelling, control, and applications was published, providing a single source for state-of-the-art modelling and control techniques, a critical evaluation of strengths and limitations, key trends, challenges and opportunities, and future research directions for researchers, engineers, and professionals in the power electronics and electrical power systems industries,

- proposing two novel controllers for GFMIs to achieve low overshoot and short settling time in step response in the GCM while adhering to the RoCoF relay limit in the SM,
- developing a seamless transition strategy for GFMIs to switch from the SM to GCM,
- proposing a convex optimization-based method for GFMIs to design robust active power controllers with enhanced damping and virtual inertia, which can work with both parametric and experimentally identified non-parametric models of the system and allows classical performance specifications such as maximum closed-loop response time, maximum overshoot, and maximum RoCoF in the SM to be easily formulated as constraints in the frequency domain in the design process,
- proposing a novel discrete-time multivariable controller for GFMIs to completely decouple the P and Q loops, and a methodical formulation of the performance specifications such as rise-time and overshoot as frequency-domain constraints on the ∞-norm of open-loop transfer functions,
- developing the concepts and providing the required control blocks to upgrade Type 4 grid-following wind turbine generators to operate in the grid-forming mode,
- studying the impact of replacing scalable Type 4 grid-following wind farms with Type 4 grid-forming wind farms in small and large-scale power systems,
- proposing an adaptive virtual resistor for GFMIs to enhance the damping of post-fault oscillations and smoothening fault recoveries, which is robust against changes in the grid condition.

1.2.2 Project Outcomes

The main outcomes of this project were

- increased penetration of solar/wind farms in particular in weak parts of the networks and unlocking future investments,
- maximal generation capacity of existing wind/solar farms located in weak parts of the grid, and
- increased reliability/security/stability of the grid as the renewable energy penetration grows.

1.2.3 Publications

One significant outcome of this project is the high-quality research articles published in prestigious journals. A list of published articles is provided below.

1. B. Bahrani, "Power-synchronized grid-following inverter without a phase-locked loop," IEEE Access, vol. 9, pp. 112 163–112 176, 2021.
2. N. Mohammed, M. H. Ravanji, W. Zhou, and B. Bahrani, "Online grid impedance estimation-based adaptive control of virtual synchronous generators considering strong and weak grid conditions," IEEE Transactions on Sustainable Energy, vol. 14, no. 1, pp. 673–687, 2022.
3. N. Mohammed, W. Zhou, and B. Bahrani, "Comparison of PLL-based and PLL-less control strategies for grid-following inverters considering time and frequency domain analysis," IEEE Access, vol. 10, pp. 80 518– 80 538, 2022.
4. W. Zhou, N. Mohammed, and B. Bahrani, "Comprehensive modeling, analysis, and comparison of state-space and admittance models of PLL-based grid-following inverters considering different outer control modes," IEEE Access, vol. 10, pp. 30 109–30 146, 2022.

5. S. Hadavi, M. Z. Mansour, and B. Bahrani, “Optimal allocation and sizing of synchronous condensers in weak grids with increased penetration of wind and solar farms,” IEEE Journal on Emerging and Selected Topics in Circuits and Systems, vol. 11, no. 1, pp. 199–209, 2021.
6. S. Hadavi, D. B. Rathnayake, G. Jayasinghe, A. Mehrizi-Sani, and B. Bahrani, “A robust exciter controller design for synchronous condensers in weak grids,” IEEE Transactions on Power Systems, vol. 37, no. 3, pp. 1857–1867, 2021.
7. S. Hadavi, J. Saunderson, A. Mehrizi-Sani, and B. Bahrani, “A planning method for synchronous condensers in weak grids using semi-definite optimization,” IEEE Transactions on Power Systems, 2022.
8. M. Z. Mansour, S. P. Me, S. Hadavi, B. Badrzadeh, A. Karimi, and B. Bahrani, “Nonlinear transient stability analysis of phased-locked loop-based grid-following voltage-source converters using Lyapunov’s direct method,” IEEE Journal of emerging and selected topics in Power Electronics, vol. 10, no. 3, pp. 2699–2709, 2021.
9. M. Z. Mansour, N. Mohammed, M. H. Ravanji, and B. Bahrani, “Output impedance derivation and small-signal stability analysis of a power- synchronized grid following inverter,” IEEE Transactions on Energy Conversion, vol. 37, no. 4, pp. 2696–2707, 2022.
10. M. Z. Mansour, M. H. Ravanji, A. Karimi, and B. Bahrani, “Linear parameter-varying control of a power-synchronized grid-following inverter,” IEEE Journal of Emerging and Selected Topics in Power Electronics, vol. 10, no. 2, pp. 2547–2558, 2022.
11. M. Z. Mansour, M. H. Ravanji, A. Karimi, and B. Bahrani, “Small-signal synchronization stability enhancement of grid-following inverters via a feedback linearization controller,” IEEE Transactions on Power Delivery, 2022.
12. D. B. Rathnayake, R. Razzaghi, and B. Bahrani, “Generalized virtual synchronous generator control design for renewable power systems,” IEEE Transactions on Sustainable Energy, vol. 13, no. 2, pp. 1021– 1036, 2022.
13. D. B. Rathnayake et al., "Grid forming inverter modeling, control, and applications," IEEE Access, vol. 9, pp. 114781-114807, 2021.
14. D. B. Rathnayake, S. P. Me, R. Razzaghi and B. Bahrani, "H_∞-based control design for grid-forming inverters with enhanced damping and virtual inertia," IEEE Journal of Emerging and Selected Topics in Power Electronics, 2022.
15. D. B. Rathnayake and B. Bahrani, "Multivariable control design for grid-forming inverters with decoupled active and reactive power loops," IEEE Transactions on Power Electronics, vol. 38, no. 2, pp. 1635-1649, 2023.
16. S. P. Me, S. Zabihi, F. Blaabjerg and B. Bahrani, "Adaptive virtual resistance for postfault oscillation damping in grid-forming inverters," IEEE Transactions on Power Electronics, vol. 37, no. 4, pp. 3813-3824, 2022.
17. M. H. Ravanji, D. B. Rathnayake, M. Zarif Mansour and B. Bahrani, "Impact of Voltage-Loop Feedforward Terms on the Stability of Grid-Forming Inverters and Remedial Actions," IEEE Transactions on Energy Conversion, 2023.

1.3 Report Outlines

During this project, several weak grid stability issues associated with the integration of inverter-based resources such as batteries, solar and wind into weak electricity grids are revealed and quantified. Furthermore, innovative solutions and control strategies for grid-connected inverters are proposed and tested in simulation and laboratory experiments. Sections 2-5 of this final report present the key findings during this project in four different themes as follows:

1. **Synchronous Condensers:**
   This section presents different aspects related to adopting SynCon in the NEM. First, an optimisation approach based on the meta-heuristic and the semi-definite convex optimisation approach is proposed to optimally allocate and size SynCons in weak grids with high penetration of renewable energy resources. Then, a robust control design approach for SynCons exciter is proposed to increase the robustness and stability of a weak grid with high penetration of renewable energy resources. The proposed controller improves the performance of a SynCon and damps the oscillations introduced by renewable energy resources in weak grids. Finally, the interaction of SynCons and existing Renewable Energy Resource (RER)s and assets in a power system is formalised, and a new index for stability analysis is introduced. The new index can analyse a black-box model, a SynCon, or other strengthening assets.

2. **Grid-Following Inverters:**
   GFLIs are currently the mainstream technology used for the integration of large-scale solar and wind farms. This technology is also used for the integration of rooftop photovoltaic systems. Despite the good performance of GFLIs in strong grids, they are prone to stability issues in weak grids, mainly caused by the PLL. Section 3 of the report starts with a nonlinear transient stability analysis of PLL-based GFLIs using Lyapunov's direct method and proposes an enhancement method using the feedback linearisation technique. Then, the impact of grid strength such as SCR on the stability and output power capability of GFLIs and GFMIs proposed some enhancement solutions are presented. Finally, the SSM including the state-space and admittance model of GFLIs is presented. Based on the derived SSMs, a comparative analysis on the stability limits of GFLIs is investigated using both the eigenvalues and impedance methods. The derived SSMs are also used to develop small-signal stability enhancement strategies for GFLIs.

3. **Power-Synchronised Grid-Following Inverters:**
   Owing to the PLL-based stability issues of conventional GFLIs, a PLL-less control strategy referred to as PSGFLIs is proposed during this project. This control strategy enables the seamless operation of GFLIs in both weak and strong grids without being prone to instability, especially in weak grid conditions. In PSGFLI, the Synchronous Reference Frame (SRF) is aligned with the inverter output current instead of the grid voltage as in the conventional GFLIs, where the 2-by-2 outer power control loop generates the estimated grid frequency (ω) and the d-component of the current reference ($i_{\mathrm{d,ref}}$). During this project, three different strategies are developed for tuning the 2-by-2 parameters of the outer power controllers of the PSGFLI. Furthermore, a Double-Synchronous-Reference-Frame-based Power-Synchronised Grid-Following Inverter (DS-PSGFLI) is proposed for faults/unbalanced grid voltage events. The four strategies are explained next.

4. **Grid-Forming Inverters:**
   GFMIs are considered the silver bullet for addressing the issues caused by the high penetration of GFLIs in power systems. While GFMIs are fundamentally similar to GFLIs in their circuit, they have a different control system enabling them to operate in the SM and also form the frequency and voltage at their terminal in the GCM. In this project, GFMIs are studied from different aspects,

and several innovative control techniques are developed to improve their performance in various operating conditions. To this end, in one study, an adaptive virtual-synchronous-generator control strategy is developed for GFMIs based on estimating the grid impedance in real-time (without additional hardware). This control strategy permits full accurate control of the VSG by mitigation of the inherent power coupling which exhibits desired predefined dynamic performance (e.g., settling time and damping) regardless of the grid strength (strong vs weak) or type (inductive vs resistive). In another study, the conventional VSG technique used in the primary control level of GFMIs is upgraded to the proposed CGVSG to address the high oscillatory behaviours of GFMIs connected to very strong grids. AVSG also enables the IBR control to accurately follow the power reference commands in the GCM and provide the required amount of virtual inertia in the SM. H_∞-based and multivariable control strategies for GFMIs are also proposed during this project. Another study in this project investigated the possibility, benefits, and limitations of providing grid-forming capabilities for conventional wind turbine generators. Eventually, one study developed a method for damping the post-fault oscillations of grid-connected inverter-based resources by using an adaptive virtual resistor focusing on the droop-based GFMIs.

2 Synchronous Condensers

The increasing number of weak-grid-connected renewable energy resources in various power systems has created challenges in recent years. The worldwide electricity network roadmap is to replace the critical role of synchronous generator-based plants such as coal-fired power plants with low-emission renewable, PEC- connected energy resources such as wind and solar farms. The transition from traditional plants to renewable energy resources introduces new challenges to power systems. For instance, un-damped voltage oscillations in the Electric Reliability Council of Texas (ERCOT), sub-synchronous resonance in the North-China power grid, and the 2016 blackout in South Australia are caused by the high penetration of renewable energy resources. There are different assets to improve stability and solve the challenges introduced by PEC-converters into the system, such as SynCons and GFMIs. However, assets installation cost, their control approach, and the interaction of the assets with existing renewable resources and upcoming new renewable energy resources must be taken into account. Hence the mentioned aspect of utilising a system-strengthening asset must be investigated [1].

2.1 Optimal Allocation and Sizing of SynCons

This section presents an optimization method to determine the optimal number, allocation, and sizing of SynCons to enhance the system strength and stability in a large weak power system in the presence of wind and solar farms. The proposed method minimizes the investment, operation, and maintenance costs of SynCons, and voltage deviation in a system while the SCR of the system is maximized at different nodes. Two different approaches are taken into account for the SCR calculation to ensure that the system strength is maximized. Since the SCR calculation based on SynCon allocation and sizing is a nonlinear problem, linear programming optimization approaches, such as convex optimization, are the complex solution. Therefore, in this section, three meta-heuristic optimization algorithms are adopted to implement the proposed optimization method with the lowest complexity and without any linearization. As the proposed method is simple and not time-consuming, it can be used for the system planning stage. Moreover, the optimized allocation/sizing of SynCons is compared with a random allocation/sizing. Then, there is a need for convex optimization to obtain global optimality. In the rest of this section, under appropriate modelling assumptions, SynCons optimal allocation, sizing, and number in a system with high penetration of Renewable Energy Resources is formulated as a mixed-integer convex optimization problem. The proposed optimization method improves the strength and stability of a large power system with high penetration of RERs. Furthermore, the proposed optimization method maintains SCR above desired values for all Point of Connection (PoC)s, while costs of investment, operation, and maintenance are minimized. The results are verified with Electro-Magnetic Transient (EMT) simulation in PSCAD/EMTDC software. The reduction of the SCR to values less than 3 and the low inertia in a power system create weak grids [2], which can lead to new challenges, such as Sub-Synchronous Oscillation (SSO)s [3–7]. In recent years, there has been an increasing interest in weak grid integration and operation enhancement of RERs [8–11]. One possible solution for overcoming the shortcomings caused by high penetration of RERs in weak grids and enhancing system strength is SynCons [12–16].

SynCon is a synchronous machine without a prime-mover, which is used in power systems to provide inertia, regulate voltage with absorption or injection of reactive power, and increase system strength [17–19]. Furthermore, SynCons can contribute to fault current. However, one of the main obstacles in utilising SynCons is their capital and operational cost, which highlights the importance of their optimal sizing and allocation [13, 20–25].

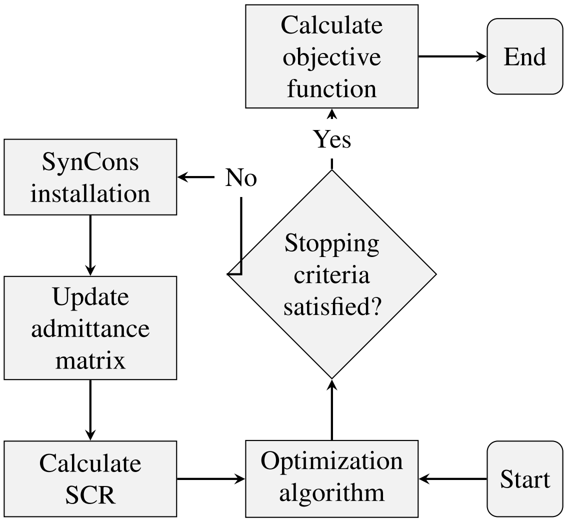

Figure 1: Flowchart of existing optimization procedures.

2.1.1 Weak Grid Definition and SynCons Impact

In this project, for the integration of RERs into a power system, the SCR is used as an index for weak grid classification. A grid with an SCR of less than three is defined as a weak grid, and a grid with an SCR less than two is defined as a very weak grid. The SCR at the PoC is calculated as:

$$\mathrm{SCR} = \frac{1}{|Z_{\mathrm{eq}}|}, \tag{1}$$

where Z_{eq} is the equivalent impedance of the grid as seen from the PoC, which is calculated from the admittance matrix. The admittance matrix Y_{bus} is a $|V| \times |V|$ matrix, where $|V|$ is the number of buses in the grid. The (i, j) element of Y_{bus} is

$$[Y_{\mathrm{bus}}]_{i,j} = \begin{cases} y_i + \sum\limits_{n\neq i,\ n\in V} y_{in}, & \text{if } i = j \\ -\,y_{ij}, & \text{if } i \neq j, \end{cases} \tag{2}$$

where y_i is the self-admittance at the ith bus, and y_{ij} is the admittance between buses i and j. The impedance matrix Z_{bus} for the grid is the inverse of Y_{bus}. The equivalent impedance for each PoC is called $[Z_{\mathrm{eq}}]$ and defined as

$$[Z_{\mathrm{eq}}]_i = [Z_{\mathrm{bus}}]_{ii}, \tag{3}$$

the ith diagonal element of the impedance matrix. Generally, to study the impact of a SynCon on the SCR, the SynCon is modeled as a current source and a parallel impedance as shown in Fig. 2. Installing a SynCon with reactance X_{sc} at bus i causes the diagonal values in the admittance matrix to change as

$$[Y^{\mathrm{new}}_{\mathrm{bus}}]_{ii} = [Y^{\mathrm{old}}_{\mathrm{bus}}]_{ii} + \frac{1}{jX_{\mathrm{sc}}}, \tag{4}$$

but it does not change the off-diagonal entries of the admittance matrix. Therefore, Z_{eq} changes with SynCons installation.

Using meta-heuristic optimization algorithms [13] to solve this optimal sizing and allocation problem for SynCons does not guarantee that optimal solutions can be found. In this project, in contrast, it is shown

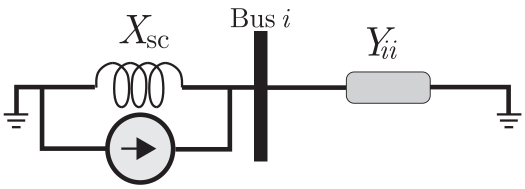

Figure 2: SynCon impedance model.

how this problem can be reformulated as a convex optimisation problem to provide global optimality using commonly available software. Since the X/R ratio is high in a high-voltage power system, transmission lines are assumed to be purely inductive. Since Y_{bus} is purely inductive, it is convenient to define the real symmetric matrix $W_{\text{bus}}{=}j[Y_{\text{bus}}]$, a notation used next. Since the matrix Y_{bus} is invertible in a power system with non-transformer zero-impedance loops [26, 27], W_{bus} is also invertible. Since W_{bus} is diagonally dominant, it follows from the Gershgorin circle theorem [28] that W_{bus} is positive semi-definite. Since W_{bus} is both invertible and positive semi-definite, it is, in fact, strictly positive definite.

2.1.2 Preliminaries on Semi-Definite Programming

A Semi-Definite Program (SDP) is a type of convex optimization problem of the form

$$\min_{x} \quad \sum_{i=1}^{n} d_i x_i \tag{5a}$$

$$\text{s.t.} \quad A_0 + \sum_{i=1}^{n} A_i x_i \succeq 0, \tag{5b}$$

$$Bx = C, \tag{5c}$$

where x is a decision variable of size n, d is a fixed vector with a size equal to n, B and C are fixed matrices, and A_is are fixed symmetric matrices. Here and throughout, the notation $A \succeq 0$ means that the symmetric matrix A is positive semi-definite. As such, an SDP involves minimizing a linear objective function subject to linear equality constraints (5c) and Linear Matrix Inequality (LMI) constraints (5b).

Semi-definite optimization problems can be solved efficiently to global optimality using off-the-shelf software (such as the commercial solver MOSEK [29]).

Optimal Sizing with Fixed Locations Suppose the locations of the SynCons are fixed, and the aim is to reduce the installation, operation, and maintenance costs of the SynCons while maintaining the SCR for all PoCs above the desired values. The decision variables are the SynCon capacities, denoted S_{syn_i} for $i \in V$. The objective function is

$$\min_{S_{\text{syn}}} \sum_{i \in V} c_i S_{\text{syn}_i}, \tag{6}$$

where c_i is the cost coefficient of the installation, operation, and maintenance cost of SynCons. The constraint is

$$\text{SCR}_k \geq a_k \quad \text{for } k \in V, \tag{7}$$

where SCR_k is the kth PoC SCR, and a_k is its desired minimum value. Define $W_{\text{bus}}^{\text{new}}{=}jY_{\text{bus}}^{\text{new}}$, and note that $W_{\text{bus}}^{\text{new}}{=}W_{\text{bus}} + \text{diag}(W)$ where $\text{diag}(W)$ is a diagonal matrix with diagonal elements are given by the vector W. The entries of this vector are obtained by re-scaling the SynCon capacity and system base MVA as follows:

$$W_k = \frac{S_{\mathrm{syn}_k}}{X_{\mathrm{sc}^k_{pu}} \times S_{\mathrm{base}}} \quad \text{for } k \in V, \tag{8}$$

where S_{syn_k} is the capacity of the kth SynCon, $X_{\mathrm{sc}^k_{pu}}$ is the impedance of the kth SynCon in pu, and S_{base} is the base apparent power of the system. Note that diag(W) is linear in the decision variable S_{syn}. By combining (1) with (4) and (7) in one equation, the SCR constraint can be expressed as

$$\frac{1}{[W^{\mathrm{new}}_{\mathrm{bus}}]^{-1}_{kk}} \geq a_k. \tag{9}$$

Since W_{bus} is strictly positive definite and diag(W) is positive semi-definite, the left-hand side of (9) is strictly positive. Therefore,

(9) can be written as

$$[W^{\mathrm{new}}_{\mathrm{bus}}]^{-1}_{kk} \leq b_k, \tag{10}$$

where $b_k = \frac{1}{a_k}$ for the kth PoC.

There are upper and lower bounds on the capacity of the SynCons, which are formulated in one equation with the location of the SynCons. Let $s_i \in \{0, 1\}$ indicate whether a SynCon will be installed at bus i. The capacity constraints are then

$$s_i \underline{S_{\mathrm{syn}_i}} \leqslant S_{\mathrm{syn}_i} \leqslant s_i \overline{S_{\mathrm{syn}_i}} \quad \text{for } i \in V, \tag{11}$$

where $\underline{S_{\mathrm{syn}_i}}$ and $\overline{S_{\mathrm{syn}_i}}$ are the minimum and maximum available capacity of ith SynCon. Note that if $s_i = 0$, indicating that a SynCon is not installed at bus i, the constraint (11) is equivalent to $S_{\mathrm{syn}_i} = 0$.

To formulate the the optimization problem defined by (6) to (11) as an SDP, an acLMI-based reformulation of the constraint (10) is used.

Overall, then,the optimization problem defined by (6) to (11) can be written as a semi-definite program in the decision variables S_{syn_i} (a vector of length $|V|$) and T (a symmetric $|V| \times |V|$ matrix) as follows

$$\min_{S_{\mathrm{syn}}, T} \quad \sum_{i \in V} c_i S_{\mathrm{syn}_i}, \tag{12a}$$

$$\text{s.t.} \quad \begin{bmatrix} T & I \\ I & \mathrm{diag}(W) + W_{\mathrm{bus}} \end{bmatrix} \succeq 0, \tag{12b}$$

$$T_{ii} \leqslant b_i \quad \text{for } i \in V, \tag{12c}$$

$$W_i = S_{\mathrm{syn}_i} / (X_{\mathrm{sc}^i_{pu}} S_{\mathrm{base}}) \quad \text{for } i \in V, \tag{12d}$$

$$s_i \underline{S_{\mathrm{syn}_i}} \leqslant S_{\mathrm{syn}_i} \leqslant s_i \overline{S_{\mathrm{syn}_i}} \quad \text{for } i \in V. \tag{12e}$$

(Here and throughout, I denotes the identity matrix of appropriate dimensions.) Strictly speaking, W is also a decision variable; however, it can clearly be rewritten in terms of S_{syn} and eliminated from the formulation using (12d). It is included in the formulation above only to simplify the notation.

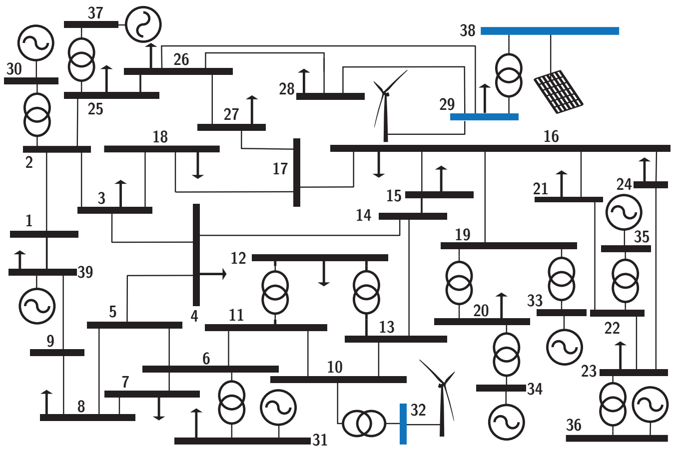

Figure 3: The configuration of modified IEEE 39-bus System.

2.1.3 Optimal Sizing and Allocation

In the previous section, the vector s is fixed. To simultaneously optimize over SynCon locations and sizes, s_i is allowed to be a binary decision variable. If at most N SynCons should be installed, the constraint

$$s_i \in \{0,1\} \quad \text{for } i \in V \quad \text{and} \quad \sum_{i \in V} s_i \leq N, \tag{13}$$

is added to (12) to model the problem of optimal sizing and allocation of SynCons. However, adding this constraint turns the problem into a mixed-integer SDP due to the binary decision variables. This can be solved to global optimality using a branch-and-bound scheme, where each sub-problem is an SDP. The branch-and-bond method is used to solve the exact mixed-integer SDP.

2.1.4 Performance Evaluation

In this section, the performance of the proposed optimization algorithm is validated based on the tests recommended by the Australian National Electricity Rules [30]. The proposed optimization is implemented in a large weak and low-inertia grid with high penetration of renewable energy. The system with the optimized location and size of SynCons is modeled in the time-domain simulation environment, PSCAD/EMTDC.

Study System Description:
The modified IEEE 39-bus system with three RERs (two wind farms and one solar farm) as shown in Fig. 3 is used as the testbed described in [13]. The nominal powers of the added RERs are 200 MW (bus 29), 500 MW (bus 32), and 200 MW (bus 38). IEEE 39-bus system is modified to have an SCR less than 3 at all PoCs to ensure that the system is weak.

Optimization Results:
The optimization results are given in Table 1 and 2. The optimized sizes of SynCons with the convex optimization are significantly less than the sizes obtained via the meta-heuristic optimization methods.

Time-Domain Simulation Verification:
PSCAD/EMTDC does the Time-domain simulation to evaluate the optimized results. Therefore, the modified IEEE 39-bus is modeled in PSCAD/EMTDC. Generic models for a solar farm and a Type IV wind turbine are used. The SynCons exciter is considered an AC1A model [31, 32].

Bus Number	10	29	32	38
Size of SynCon (MVA)	13	16	25	42

Table 1: Optimization Results

Optimization Method	**Bus Number**	**Size**	$F(x)$	**SCR**
GA	29, 29, 38, 38	13, 10, 118, 43	2.04	3.09
Bat	1, 38	11, 177	4	3
HSS	38, 38, 38	46, 10, 130	2.1	3.03

Table 2: Optimization Result For the Augmented IEEE 39-Bus

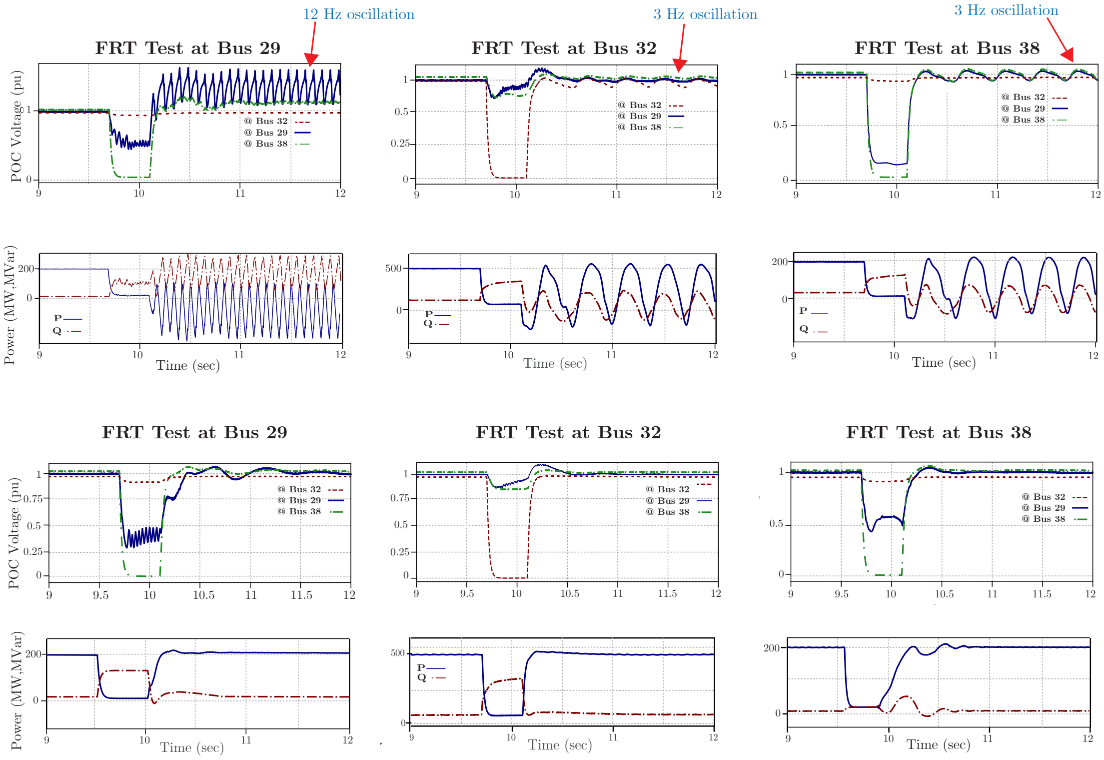
12 Hz oscillation
3 Hz oscillation
3 Hz oscillation
FRT Test at Bus 29
FRT Test at Bus 32
FRT Test at Bus 38
FRT Test at Bus 29
FRT Test at Bus 32
FRT Test at Bus 38

Figure 4: FRT test results with the meta-heuristic approach

The contingencies applied to the modified IEEE 39-bus system are as follows

- Fault Ride-Through (FRT) Test: In this contingency, a three-phase fault is applied at all RERs' PoCs at t=9.7 s and cleared after 430 ms. According to the National Electricity Rules [30, 33], RERs must ride through such a contingency.

2.2 A Data-Driven SynCon Exciter Controller Design

This section focuses on the internal structure of SynCons and designs a robust controller for them to improve stability in weak grids. Even though the exciter control of SynCons is a well-established technology, further developments are required to guarantee the stability of post-fault operations, particularly in weak grids. This section proposes a data-driven approach for designing higher-order optimized exciter controllers to meet this requirement. A Pseudo-Random Binary Sequence (PRBS)-based system identification method is used to obtain the frequency response data of the power system from the exciter point of view, which is

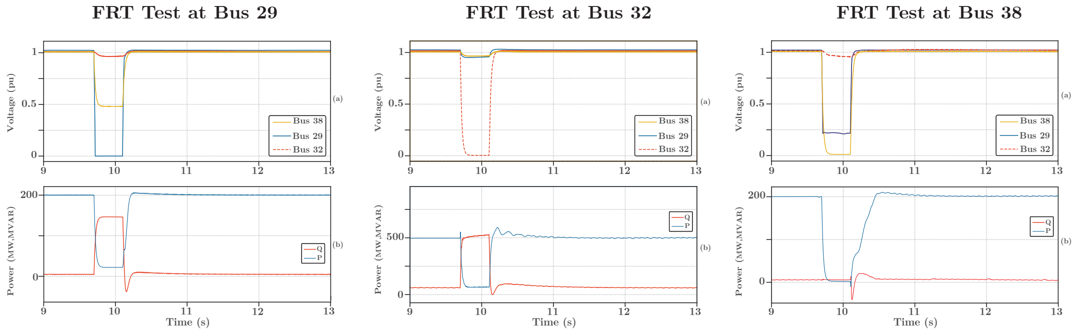

Figure 5: FRT test results with convex approach

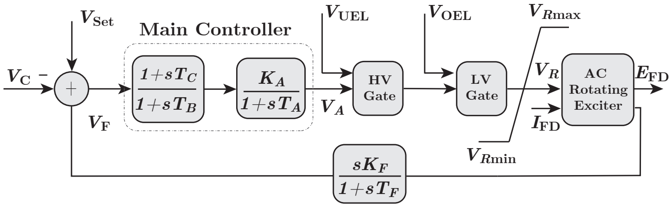

Figure 6: The AC1A exciter diagram.

then fed into the proposed optimal control design procedure.

The system's input can be perturbed in a specific frequency with a magnitude equal to the PRBS method. Then, with the Fast Fourier Transform (FFT) algorithm, the system's output can be calculated in the perturbed frequency. Then, the identified model can be validated for that specific frequency [34].

2.2.1 Data-Driven Model Identification

Typically, robust control design methods require a parametric model of the plant, e.g., its state-space model. Nevertheless, only the Frequency Response Data (FRD) of the system to be controlled is required for the control design methodology proposed in this project. Even though the proposed control design method is fully capable of working with the parametric model (e.g., transfer function) of the system, a non-parametric model (e.g., FRD model), which is identified based on simulation, is used. Typically, power systems comprise a multitude of different types of components. Some of these components are black boxes. Therefore, if a parametric model is derived using the first principles, the dynamics of these black boxes are typically approximated or ignored. Hence, an accurate Linear Time-Invariant (LTI) model of the system ($G(j\omega) \in \mathbb{C}$) that incorporates otherwise hard-to-model dynamics is derived by identifying the model of the system. The LTI model of the system is defined as

$$V_c(j\omega) = G(j\omega)V_A(j\omega), \tag{14}$$

where $V_c(j\omega)$ and $V_A(j\omega)$ are the frequency-domain quantities of the signal points V_c and V_A in the exciter, as shown in Fig. 6. To identify the LTI model of the system, a signal injection-based method is used to perturb the system, and a cross-correlation-based method is used to identify the FRD of the system using the corresponding input and output signals.

2.2.2 Frequency Response Data

Once the output data that correspond to the input PRBS perturbations are retrieved, the FRD can be identified. In this project, a cross-correlation-based identification method is used to reject the noise sources and identify an accurate FRD model of the system [35]. The power grid is a complex system composed of various components with linear and nonlinear characteristics. However, in steady-state, and for small-signal perturbations, the power grid can be assumed to be an LTI discrete-time system. Hence, the sampled system can be described as follows

$$y(n) = \sum_{k=1}^{\infty} g(k)u(n-k) + v(n) \tag{15}$$

where $y(n)$, $u(k)$, $g(k)$, and $v(n)$ are the sampled output signal, the sampled input signal, the impulse response of the system, and the noise, respectively. The cross-correlation operation performed between the output and the input signals is

$$R_{y,u}(m) = \sum_{n=1}^{\infty} g(m)R_{u,u}(m-n) + R_{v,u}(m) \tag{16}$$

where $R_{y,u}$, $R_{u,u}$, and $R_{v,u}$ are the cross-correlation between the output and the input signals, the auto-correlation of the input signal, and the cross-correlation between the noise and the input signal, respectively.

If a white noise signal is used to perturb the system, the term $R_{v,u}(m)$ falls to zero, and $R_{u,u}(m)$ becomes the Kronecker delta function ($\delta(m)$). The PRBS signal used to perturb the system is an approximation of white noise, which is much easier to practically implement than white noise. Therefore, the above assumptions on $R_{v,u}(m)$ and $R_{u,u}(m)$ still hold. The frequency-domain model of the system can be found by applying the discrete Fourier transform to (16). The FRD of the system is identified as follows

$$\hat{G}(j\omega) = \frac{\sum_{i=1}^{r} \mathcal{F}\left\{R_{y,u}^{i}\right\}}{\sum_{i=1}^{r} \mathcal{F}\left\{R_{u,u}^{i}\right\}} \quad \forall\omega \in \Omega \tag{17}$$

where $\hat{G}(j\omega) \in \mathbb{C}$ is the identified FRD, $\mathcal{F}\{\cdot\}$ stands for the discrete Fourier transform, and r is the number of PRBS periods used for identification. Increasing r attenuates the noise effects, especially in the high-frequency range of the frequency response. However, it also increases the identification time. Therefore, there is a trade-off between the number of PRBS periods to be used and the attenuation of the noise effects. Five periods of the PRBS signal are used for the identification. Fig. 7 shows the identified FRD, which covers the frequency spectrum from 0.0614 rad/s to 31.4 rad/s. The identification is carried out when a SynCon is installed in different systems as follows: 1. a stronger Single Machine Infinite Bus (SMIB) case with an SCR equal to 10, 2. a weaker SMIB case with an SCR equal to 1, and 3. at Bus 29 in the modified IEEE 39-bus system. As shown in Fig. 7, the FRD response for these different scenarios is similar, and it is sufficient to identify it only once. If the SynCon's structure or exciter structure changes significantly, the new system must be identified again, and the control design should be done based on the newly identified system.

2.2.3 Frequency-Domain Performance Specifications

In this project, an H_∞ based control design method is presented to design a controller for the exciter of the SynCon. The required performance of the controller is defined in terms of constraints on the ∞-norm of the weighted sensitivity functions. To this end, first, to reject the impact from disturbances on the output, the ∞-norm of the weighted output sensitivity function ($\mathcal{S}$) is minimized. $\mathcal{S}$ is defined as $\mathcal{S}=(I+GK)^{-1}$, where G, K, and I are the plant, controller, and identity transfer function matrix, respectively. To curtail

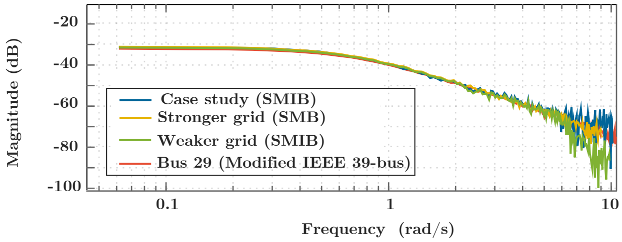

Figure 7: The identified frequency response of the system for several scenarios.

the control effort of the controller in certain frequency regions, the infinity norm of the weighted input sensitivity function ($\mathcal{U}$) is minimized. $\mathcal{U}$ is defined as $\mathcal{U}=K\mathcal{S}$. Therefore, the complete mixed sensitivity problem is as follows

$$\min_{K} \left\| \begin{matrix} W_1\mathcal{S} \\ W_2\mathcal{U} \end{matrix} \right\|_{\infty} \tag{18}$$

where W_1 is the performance weighting function, and W_2 is the input weighting function. Disturbance rejection performance specifications of the system can be realized through the frequency domain quantities such as bandwidth (ω_b) and peak sensitivity (M_s) of $\mathcal{S}$. Such requirements can be roughly shown as $|\mathcal{S}| \leq \frac{1}{|W_1|}$ [36]. Therefore, W_1 is chosen as

$$W_1 = \left(\frac{s/\sqrt[\lambda]{M_s} + \omega_b}{s + \omega_b\sqrt[\lambda]{\varepsilon_s}} \right)^{\lambda} \tag{19}$$

where ε_s is the minimum allowable steady-state error for a step disturbance. $\lambda \in \mathbb{Z}^+$ determines the sharpness of the roll-off from low to high-frequency; for a quicker roll-off, λ can be increased. The control effort performance specifications are realized through $\mathcal{U}$. Typically, the high-frequency gain of $\mathcal{U}$ is restrained to achieve superior noise attenuation. These specifications can be roughly denoted as $|\mathcal{U}| \leq \frac{1}{|W_2|}$ [36]. Therefore, W_2 is chosen as

$$W_2 = M_u, \tag{20}$$

where M_u is the peak input sensitivity. The ∞-norm of a stable function $\mathcal{S}(e^{j\omega})$, i.e., $\|\mathcal{S}\|_{\infty}$ is defined as

$$\|\mathcal{S}\|_{\infty} = \sup_{\omega} \bar{\sigma}[\mathcal{S}(e^{j\omega})]$$

where $\bar{\sigma}$ is the maximum singular value.

Finally, the steady-state gain of the controller (K_{ss}) is chosen by evaluating the controller at z=1 (ω=0). This can be formulated as a linear equality constraint as

$$K_{\mathrm{ss}} = \frac{x_p + x_{(p-1)} + \cdots + x_0}{1 + y_{(p-1)} + \cdots + y_0}. \tag{21}$$

K_{ss} is equal to the voltage regulator gain of the conventional AC1A exciter [37]. The designed H_{∞} controller resulted from solving the optimization problem ($K_{H_{\infty}}$) is as follows

$$K_{H_{\infty}} = \frac{47.34z^4 + 57.94z^3 + 0.9156z^2 - 53.29z - 41.39}{z^4 + 1.167z^3 - 0.0646z^2 - 1.163z - 0.8621}. \tag{22}$$

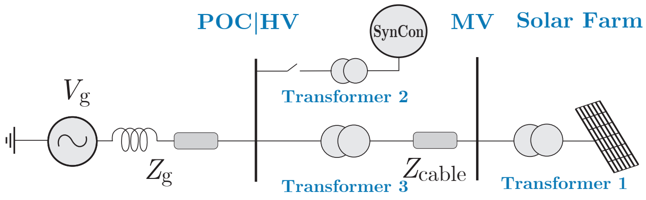

Figure 8: SMIB model configuration with a SynCon.

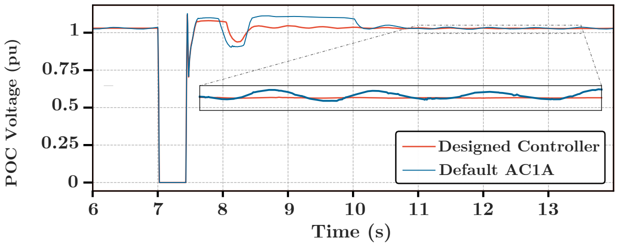

Figure 9: Simulation results of the SMIB test-bed PoC voltage when the FRT test is applied at PoC at t=7 s with a duration of 430 *ms with the proposed exciter control and AC1A exciter.*

2.2.4 Performance Evaluation

In this section, the effectiveness of the proposed exciter controller is evaluated with a focus on weak grids with high penetration of renewable energy resources. PSCAD/EMTDC is used for time-domain simulation, which allows electromagnetic-transient network modelling. EMT-based simulation can accurately represent the dynamics of system elements such as inverters and synchronous machines.

To verify the effectiveness of the proposed exciter design, a SynCon with the proposed exciter is implemented, and its performance is compared with a SynCon equipped with the conventional AC1A exciter in a strong grid and different scenarios of weak grids.

Weak Grid Scenario:
In this part, adopting the system of Fig. 8, the proposed exciter is compared with the conventional AC1A exciter in a weak grid. The FRT test, the High-Voltage Ride Through (HVRT) test, and the V_{ref} test are applied to validate the performance of the proposed exciter.

FRT Test:
The FRT test is applied at t=7 s. The solar farm injects its nominal power, and the system is stable before the fault in both cases of conventional AC1A exciter and with the proposed exciter. Fig. 9 depicts the PoC voltage prior to and subsequent to the FRT test for both exciters. As illustrated in Fig. 9, with the AC1A exciter, 1 Hz oscillation exists in the PoC voltage, however, the PoC voltage oscillation is damped by the proposed exciter controller subsequent to the fault. Moreover, with the proposed exciter, the system reaches the steady-state in 1 s while the system with the AC1A exciter reaches the steady-state in 3 s after the fault clearance.

HVRT Test:
The HVRT test is applied at t=15 s. The PoC voltage is increased from 1 to 1.05 pu. The solar farm must reduce the reactive power at the PoC based on its controller. Fig. 10 shows reactive power at PoC prior to and subsequent to the test with both the proposed exciter and the conventional AC1A exciter. As illustrated in Fig. 10, in the system with the proposed exciter, the system is stable after the HVRT test. However,

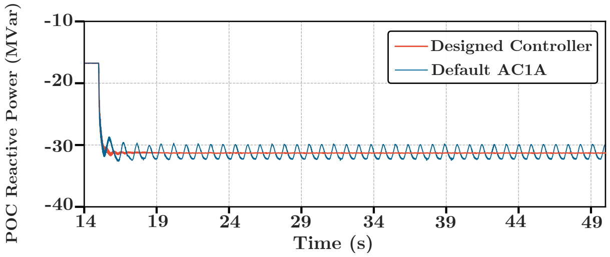

Figure 10: Simulation results of the SMIB test-bed PoC reactive power when the five percent HVRT test is applied at t=15 s with the proposed exciter and AC1A exciter.

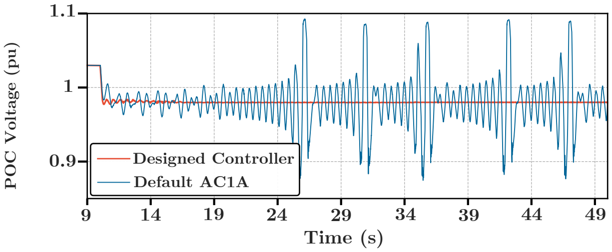

Figure 11: Simulation results of the SMIB test-bed PoC voltage when the five percent V_{ref} test is applied at t=10 s with the proposed exciter and AC1A exciter.

with the AC1A exciter, the reactive power at the PoC has post-disturbance oscillations.

V_{ref} Test:
The V_{ref} test is applied at t=10 s. The reference voltage is dropped from 1.03 pu to 0.98 pu at t=10 s. Fig. 11 depicts the PoC voltage prior and subsequent to the V_{ref} test for both exciters. The solar farm in a system with the proposed exciter can follow the new reference voltage. However, in the system with the conventional AC1A exciter, the solar farm cannot follow the reference and causes instability in the system.

2.3 Quantifying Stability in Inverter-based Weak Grids

This section investigates the impact of the SCR, X/R ratio, and SynCon utilisation on the stability of IBRs in a weak grid based on a quantified Stability Index (SI), which is derived based on the impedance-based stability analysis. Compared to previous works on the impedance-based stability analysis of IBRs, in this chapter, the grid impedance is not a simple RL impedance, and it can have different combinations. The PRBS identification method is applied to calculate the dq-domain impedance of a SynCon, an IBR, and a system. In addition, the proposed index is validated in several scenarios where IBRs are integrated into a weak grid in PSCAD/EMTDC software.

2.3.1 G-Norm Criterion and the Stability Index

Generally, in the impedance-based stability analysis, the system is divided into two subsystems of a load (an IBR with the dq-domain admittance of Y_{c}) and a source (with a dq-domain impedance of Z_{g}), and the impedance ratio, which is defined as

$$L = Z_{\text{g}} Y_{\text{c}}, \tag{23}$$

must satisfy the Nyquist Criterion.

Since L is a 2×2 matrix, the characteristic loci satisfies the Nyquist criterion if the largest magnitude is restricted to less than $\frac{1}{2}$ for all frequencies. Therefore, if G-norm of L is less than $\frac{1}{2}$ for all frequencies, the integration of an IBR to a system is stable. The G-norm of the matrix L is defined as

$$||L||_{\mathrm{G}} = ||Z_g Y_c||_{\mathrm{G}} = \max_{1\leq j\leq 2, 1\leq i\leq 2}(|l_{i,j}|) < \frac{1}{2}, \tag{24}$$

where $l_{i,j}$ is the ijth element of the matrix L. However, (24) is in a coupled form based on the matrix L, and the impact of Y_{c} and Z_{g} on the system stability is not clear. It is possible to decouple L based on the individual G-norm of Y_{c} and Z_{g}. By considering

$$Z_{\mathrm{g}} Y_{\mathrm{c}} = \begin{bmatrix} a_1 & a2 \\ a3 & a4 \end{bmatrix} \begin{bmatrix} b_1 & b2 \\ b3 & b4 \end{bmatrix}, \tag{25}$$

L can satisfy (24) if

$$|a_1 b_1 + a_2 b_3| < \frac{1}{2}, \tag{26}$$

$$|a_1 b_2 + a_2 b_4| < \frac{1}{2}, \tag{27}$$

$$|a_3 b_1 + a_4 b_3| < \frac{1}{2}, \tag{28}$$

$$|a_3 b_2 + a_4 b_4| < \frac{1}{2}. \tag{29}$$

Eqs. (26) to (29) are satisfied if

$$|a_1||b_1| + |a_2||b_3| < \frac{1}{2}, \tag{30}$$

$$|a_1||b_2| + |a_2||b_4| < \frac{1}{2}, \tag{31}$$

$$|a_3||b_1| + |a_4||b_3| < \frac{1}{2}, \tag{32}$$

$$|a_3||b_2| + |a_4||b_4| < \frac{1}{2}. \tag{33}$$

Therefore, based on Cauchy–Schwarz inequality, the return ratio norm condition G-norm criterion can be decoupled based on the individual norms of Y_{c} and Z_{g}. Consequently, the SI is defined as

$$\mathrm{SI} = ||Z_{\mathrm{g}}||_{\mathrm{G}}.||Y_{\mathrm{c}}||_{\mathrm{G}}, \tag{34}$$

and a system is stable if

$$\mathrm{SI} < \frac{1}{4} \; \omega \in (-\infty, \infty). \tag{35}$$

It must be noted that upon adding a system strengthening asset, Z_{g} is not an RL load anymore. Therefore, the dq-domain impedance of Z_{g} is not necessarily a symmetric matrix. For instance, by adding a SynCon at the PoC, the new grid impedance is defined as

$$Z_{\mathrm{gnew}} = Z_{\mathrm{g}} || Z_{\mathrm{sync}}, \tag{36}$$

where Z_{sync} is the SynCon dq-domain impedance matrix. Since a SynCon can be modelled with a source and impedance, the equivalent impedance as described in (36), by installing the system strengthening assets, the stability margin is increased by decreasing the grid impedance.

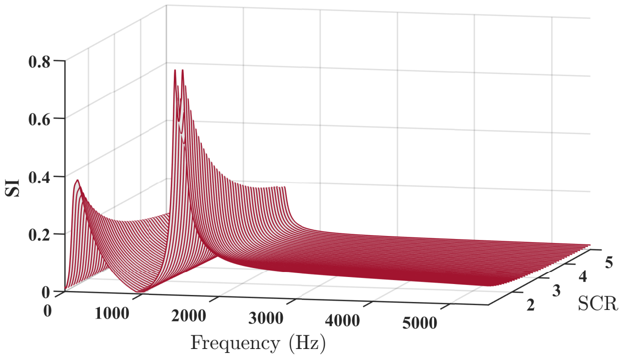

Figure 12: The SI for different ranges of frequency in the SMIB case with the X/R ratio of 8 and different SCRs from 1.1 to 5.

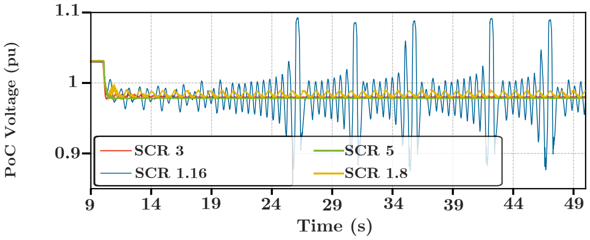

Figure 13: Time-domain simulation results of the SMIB PoC voltage with different SCRs when the five percent V_{ref} test is applied at t=10 s.

2.3.2 Performance Evaluation

This part validates the performance of the stability index and impedance identification with time-domain simulation. Different scenarios of weak grid integration of wind and solar farms are investigated. Furthermore, the impact of SynCon size on the proposed stability index is studied. In this study for the time-domain EMT simulation, PSCAD/EMTDC is utilised to accurately represent the dynamics of system elements such as IBRs and SynCons.

2.3.3 SCR Impact on Stability

In this scenario, a 400 MW solar farm is connected to a SMIB setup as shown in Fig. 8. The SMIB case SCR changes from 1.1 to 5 with the step of 0.1, and the X/R ratio is assumed to be constant and equal to 8. Fig. 12 illustrates the SI for different ranges of frequency. As shown in Fig. 12, in the SMIB case below a specific SCR, the SI is greater than 0.25, which means the system is not stable. As expected, by increasing the SCR value, the SI decreases. To validate the SI for two unstable scenarios and stable scenarios based on Fig. 12, small-signal tests such as active power reference step and reference voltage step are applied.

As illustrated in Fig. 13, the reference voltage step test is applied to the SMIB case with the SCR of 1.16, 1.8, 3, and 5. As a result, both expected stable scenarios as predicted by the SI, i.e., the cases with SCR equal to three and five, are stable subsequent to the disturbance, and the solar farm can follow the 5% voltage reference step. On the other hand, the predicted unstable scenarios (SCR = 1.16 and 1.8) are unstable subsequent to the 5% voltage reference step, and the reference voltage step causes sustained oscillations on the PoC voltage.

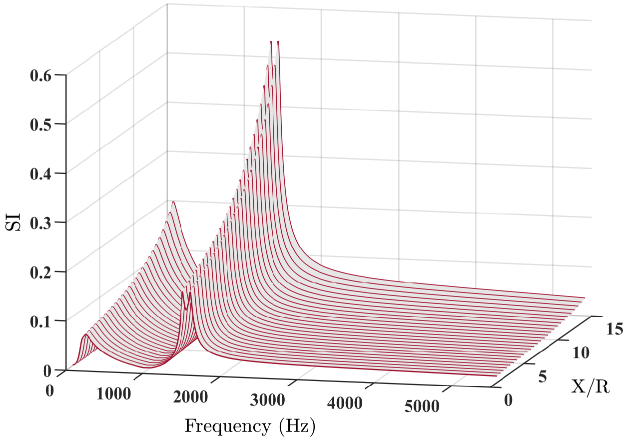

Figure 14: The SI for different ranges of frequency in the SMIB case with the SCR of 2 and different X/R from 2 to 14.

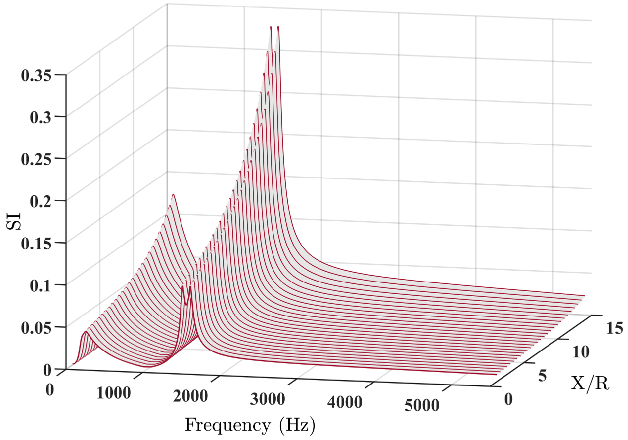

Figure 15: The SI for different ranges of frequency in the SMIB case with the SCR of 4 and different X/R from 2 to 14.

2.3.4 X/R Ratio Impact on Stability

In this part, the X/R ratio of the system shown in Fig. 8 changes from 2 to 14 with the step of one. Two SCRs of two and four are considered for this study, and the SI is calculated in each scenario. Fig. 14 shows the SI for the system with the SCR of two and different X/R ratios. As illustrated in Fig. 14, the SCR is not a sufficient index for the stability analysis. In the same system with the SCR of two, considered as a weak grid, the SI is greater or lower than 0.25 depending on the X/R ratio. That is, with the same SCR, the system can be stable or unstable by changing the X/R ratio. By decreasing the X/R ratio, the resistive part of the system impedance increases. Therefore, the damping factor in the system increases and makes the system stable. Fig. 15 depicts the SI for different ranges of frequencies in a system with an SCR of 4 and different X/R ratios from 2 to 14. As shown in Fig. 15, the system can be unstable also in a system with a high SCR, which is considered as a strong grid. By increasing X/R ratio, the SI increases and makes the system unstable.

2.3.5 SynCon Impact on Stability

In this part, the impact of a SynCon on the SI for a SMIB system shown in Fig. 8 is studied. By adding a SynCon, the grid impedance is not a simple RL load, and, a SynCon impacts the system impedance.

Furthermore, the impact of SynCon size on the SI is investigated. A SynCon is added to the unstable condition observed in previous studies based on the SI value (SCR=2 and X/R=10). By adding a 10 MVA

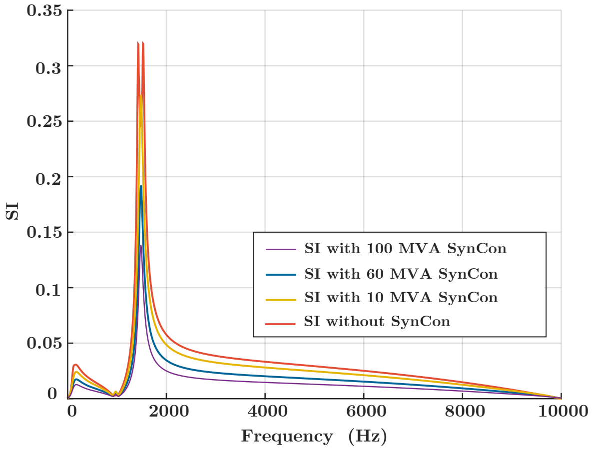

Figure 16: Impact of SynCon installation on the SI in a system with the SCR of 2 and X/R ratio of 10.

SynCon, the SCR does not change noticeably. On the other hand, a 60 MVA SynCon increases the SCR from 2 to 2.15, and adding a 100 MVA SynCon increases the SCR to 2.25. Therefore, it is expected that by adding a 60 MVA and a 100 MVA SynCon, the solar farm integration becomes stable.

Fig. 16 shows the SI for the SMIB case with the SCR of 2, X/R ratio of 10, and adding SynCon at the PoC with different sizes. Adding 100 MVA and 60 MVA SynCons reduces the SI significantly compared to the system without any SynCon (as expected from the SCR calculation). By installing the 100 MVA and 60 MVA SynCons, the SI is decreased and kept below 0.25, which is the stability margin of the SI. However, by adding a 10 MVA, the SI is not reduced enough to stabilize the solar farm integration. However, adding a larger SynCon means an additional expense. Therefore, a suitable size must be chosen based on the SI and cost per size of SynCons.

3 Grid-Following Inverters

Currently, GFLIs are the prevalent IBRs worldwide and the leading technology for controlling large-scale solar and wind farms. Despite the excellent GFLIs performance in strong grids, they are prone to stability issues in weak grids, mainly caused by their PLL. This section studies GFLIs from different aspects and proposes several analyses and solutions to enhance their performance.

3.1 Nonlinear Transient Stability Analysis of the PLL-Based GFLIs Using Lyapunov's Direct Method

In this subsection, using Lyapunov's stability theorem, the transient stability conditions for a grid-following Voltage Source Converter (VSC) are found. These conditions take into account both the grid specifications and the VSC's dynamics. The derived conditions are based on a well-known nonlinear model of the VSC's PLL. To evaluate the stability of the nonlinear system, Lyapunov's direct method is employed. To this end, a new Lyapunov function is proposed, and its characteristics are analysed. Using this Lyapunov function, the domain of attraction of the system's equilibrium point is calculated. Additionally, a novel system strength index based on the domain of attraction of the system is proposed. The privilege of this index over the conventional indices are absoluteness, VSC's dynamics consideration, and comparability of different VSCs with each other from a stability point of view. In the end, the correctness of the proposed stability analysis is validated via simulation in MATLAB/PLECS and experiment.

3.1.1 Nonlinear Model of a PLL

The block diagram of a grid-following VSC is shown in Fig. 17. This block diagram is composed of various parts such as a current control unit, employing a voltage feed-forward controller, and a grid-synchronisation unit. A factor that plays a vital role in the stability of the system is the grid synchronisation unit. For grid-synchronisation of grid-connected VSCs, various synchronisation methods, including PLLs and Fourier Transformation-based methods, are proposed. In this study, without loss of generality, a Synchronous Reference Frame Phase-Locked Loop (SRF-PLL) is considered. The block diagram of the SRF-PLL is depicted in Fig. 18. Using this block diagram, the nonlinear differential equation related to the PLL and the grid can be derived as

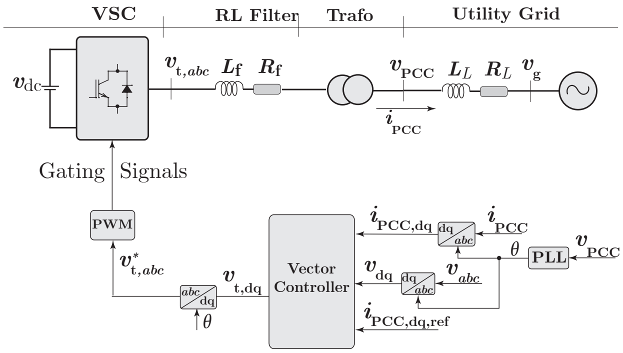

Figure 17: A SMIB model of a grid-following VSC with its vector current control. The output filter of the VSC is an RL filter, and the grid is modeled as an inductor and a resistor in series with an ideal voltage source.

$$\ddot{\delta} = -K_p V_{\mathrm{g}} \dot{\delta} \cos\delta + K_p L_L I_{\mathrm{PCC}} \cos\theta_I \ddot{\delta} + K_i R_L I_{\mathrm{PCC}} \sin\theta_I + K_i L_L \omega_0 I_{\mathrm{PCC}} \cos\theta_I + K_i L I_{\mathrm{PCC}} \cos\theta_I \dot{\delta} - K_i V_{\mathrm{g}} \sin\delta. \tag{37}$$

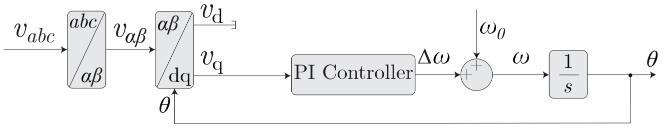

Figure 18: The block diagram of a sample SRF-PLL.

In (37), by setting $\hat{x}_1$=δ and $\hat{x}_2$=$\dot{\delta}$, the state-space model can be written as

$$\begin{cases} \dot{\hat{x}}_1 = \hat{x}_2, \\ \dot{\hat{x}}_2 = B - D\sin\hat{x}_1 + (A\cos\hat{x}_1 + C)\hat{x}_2, \end{cases} \tag{38}$$

where A, B, C and D are

$$\begin{aligned} A &= \frac{-K_p V_g}{1 - K_p L_L I_{\text{PCC}} \cos\theta_I}, \quad B = \frac{K_i R_L I_{\text{PCC}} \sin\theta_I + K_i L_L \omega_0 I_{\text{PCC}} \cos\theta_I}{1 - K_p L_L I_{\text{PCC}} \cos\theta_I}, \\ C &= \frac{K_i L_L I_{\text{PCC}} \cos\theta_I}{1 - K_p L_L I_{\text{PCC}} \cos\theta_I}, \text{ and } D = \frac{K_i V_g}{1 - K_p L_L I_{\text{PCC}} \cos\theta_I}. \end{aligned} \tag{39}$$

The equilibrium points of the system shown in (38) can be found by setting $\dot{\hat{x}}_1$ and $\dot{\hat{x}}_2$ equal to zero. Thus, the equilibrium points are calculated as $(\hat{x}_1^e, \hat{x}_2^e)$=$(\sin^{-1}(\frac{B}{D}), 0)$ and $(\hat{x}_1^e, \hat{x}_2^e)$=$(\pi - \sin^{-1}(\frac{B}{D}), 0)$.

3.1.2 Stability Analysis of a GFLI

Contrary to linear systems, there are multiple stages in assessing the stability of a nonlinear system equilibrium points. These steps can be briefed as:

- equilibrium points presence,
- equilibrium points stability, and
- stable equilibrium points domain of attraction.

The initial part of a nonlinear system stability assessment is to evaluate whether the system has an equilibrium point. In (38), the condition for having equilibrium points is $|B| < |D|$. Then, the stability of the equilibrium point should be assessed using Lyapunov's linearization method. For the system under study, the stability necessary and sufficient conditions can be derived as

$$K_i L_L I_{\text{PCC}} \cos\theta_I < K_p \sqrt{V_g^2 - I_{\text{PCC}}^2 (R_L \sin\theta_I + X_{L_0} \cos\theta_I)^2}. \tag{40}$$

And finally, unlike linear systems, nonlinear systems stable equilibrium points do not have infinite domain of attractions, i.e., there is no guarantee that the states could converge to the equilibrium point for any arbitrary initial condition. Therefore, it is essential to find the biggest neighbourhood around each equilibrium point that if the states are located in, they eventually end up at that equilibrium point. This neighbourhood has been named the domain of attraction. This domain can be found by employing Lyapunov's direct method. For this purpose, this section proposes a Lyapunov function as

$$V(x) = -Bx_1 + D(\cos(\alpha) - \cos(x_1 + \alpha)) + \frac{1}{2}x_2^2. \tag{41}$$

This function can be used for finding the radius of the domain of attraction by solving the conditional equations

$$R_1 = \min \sqrt{(x_1^2 + x_2^2)} \text{ s.t. } V(x) = 0, \forall x \neq 0 \text{ and } R_2 = \min \sqrt{(x_1^2 + x_2^2)} \text{ s.t. } \dot{V}(x) = 0, \forall x \neq 0 \tag{42}$$

And the domain of attractions radius is

$$\rho = \min\{R_1, R_2\}. \tag{43}$$

In practice, finding the radius of the domain of attraction of this system can be done easier. It can be seen that the second state (x_2) cannot make either of $V(x)$ and $\dot{V}(x)$ negative, because, in both equations, x_2 only appears in the form of x_2^2. Hence, it is sufficient to find R_1 based on $f(x_1)$ (by finding the biggest circle's radius in which $f(x_1) > 0$), and R_2 based on $g(x_1)$ (by finding the biggest circle's radius in which $g(x_1)<0$). Then, by replacing R_1 and R_2 into (43), the radius of the domain of attraction can be found. The required steps to this end can be summarized in the following steps:

- Form $f(x_1)$ and $g(x_1)$.
- Find the smallest $|x_1|$ that makes $f(x_1)=0$. This $|x_1|$ is R_1.
- Find the smallest $|x_1|$ that makes $g(x_1)=0$. This $|x_1|$ is R_2.
- The radius of the domain of attraction is then calculated as $\rho = \min\{R_1, R_2\}$.

3.1.3 Disturbance Tolerance

The domain of attraction of an equilibrium point shows the disturbance tolerance of the system. Hence, the domain of attraction can be the base of a system strength index. The conventional system strength indices, such as SCR, do not consider the dynamics of the VSC. Additionally, these indices do not provide any information about when the system becomes unstable. Based on its internal controls, one VSC can work properly in a grid with a certain SCR, although another VSC might not be able to do so. Therefore, in this part, a novel system strength index based on the domain of attraction of the equilibrium point of the system is defined.

In a very strong grid, i.e., a grid with negligible impedance,

$$f(x_1) = K_i V_g (1 - \cos(x_1)) > 0, \ \forall x_1 \in [-\pi, \pi], \tag{44}$$

and

$$g(x_1) = -K_p V_g \cos(x_1) < 0, \ \forall x_1 \in [\frac{-\pi}{2}, \frac{\pi}{2}]. \tag{45}$$

Hence, in this case, the domain of attraction of the equilibrium point is $\frac{\pi}{2}$. Thus, by normalization of the radius of the domain of attraction, a new system strength index ζ can be defined as

$$\zeta = \frac{2}{\pi}\rho. \tag{46}$$

By this definition, the shortcomings of the previous indices can be rectified. This index has a value between 0 and 1. ζ=0 corresponds to an unstable system, ζ=1 corresponds to a very strong system in which the grid impedance is negligible, and $0 < \zeta < 1$ corresponds to a stable system. Note that the larger ζ is, the more stable the system will be. Therefore, in contrast to previous indices, this index can anticipate the stability and instability of the system, and also, can compare the strength of two different systems with each other.

Parameters	Value	Description
f_s	5 kHz	Switching Frequency
L_f	5 mH / 0.5 pu	Filter Inductance
R_f	0.5 Ω / 0.05 pu	Filter Resistance
V_dc	200 V	DC Link Voltage
V_g	50 V / 1 pu	Grid Root Mean Square (RMS) Voltage
f	50 Hz	Grid Frequency
S_nominal	250 VA / 1 pu	VSC Nominal Power
R_L	0.5 Ω / 0.05 pu	Grid Resistance
L_L	3.8 mH / 0.38 pu	Grid Inductance
SCR	7.75	Short Circuit Ratio
X/R	2.38	X/R ratio

Table 3: Study System Parameters.

3.1.4 Performance Evaluation

In this section, the simulation and experimental results of a grid-following VSC are presented to validate the effectiveness of the proposed Lyapunov function, and study the influence of the grid inductance on the domain of attraction of the system's stable equilibrium point and ζ. The results verify the proposed method, and the index's capability and accuracy.

In this part, the grid-following VSC shown in Fig. 17 with parameters presented in Table 3 is simulated in PLECS for different cases. In the following simulation test cases, the PLL's coefficients are chosen as $K_p = 10\ \frac{rad}{V.s}$ and $K_i = 400\ \frac{rad}{V.s^2}$. Additionally, the Proportional Integral (PI) controllers employed in the current controller are chosen as $K_{\mathrm{PI,CC}}(s)$=$500\frac{0.005s+0.5}{s}$. In the first simulation scenario, a three-phase fault occurs in the system. It is shown that since the states of the system at the end of the fault are in the domain of attraction of the equilibrium point after the fault, the system will converge to this equilibrium point. In the second scenario, for different grid resistances, the grid reactance that makes the system unstable is found and compared with the results from the proposed analysis method. Finally, the effect of increasing the grid inductance on the domain of attraction and ζ is studied. It is shown that increasing the grid inductance shrinks the domain of attraction; hence, ζ is reduced. At the end of this part, a discussion about the second equilibrium point of the system is presented.

Stability Analysis upon a Three-phase Fault:
In this test, the VSC is initially in the steady-state and does not inject any current. Also, X_{L_0} is set to 5 Ω, and R_L is 1 Ω. Therefore, D is a positive value. At t=0.1 s, the VSC's injected RMS current steps up to 7 A with θ_I=$\frac{\pi}{6}$. For these operating conditions, ζ=0.51; hence, this operating point is stable. The simulation results for this scenario are shown in Fig. 19. Fig. 19(a) and (b) show the VSC's instantaneous and dq currents, respectively. The grid frequency extracted by the PLL is shown in Fig. 19(c). At t=0.1 s, the set-points of i_d and i_q are changed from zero to $3.5\sqrt{6}$ A and $3.5\sqrt{2}$ A, respectively. As shown in Fig. 19, in this scenario, the system maintains its stability. This matches the result of ζ anticipation. In this scenario, the stable equilibrium point of the system is $(0.74, 0)$. The other equilibrium point in which δ is located between $\frac{\pi}{2}$ and π is unstable. At t=0.2 s, a three-phase fault occurs in the middle of the line, causing the voltage to drop to 0.1 pu with a duration of 80 ms. Also, the impedance seen from the output terminal of the VSC becomes 0.1 pu during the fault. As shown in Fig. 19, the system can maintain its stability both during and subsequent to the fault clearance. The reason for which the system remains stable after the fault clearance should be looked for in the domain of attraction of the system's equilibrium point

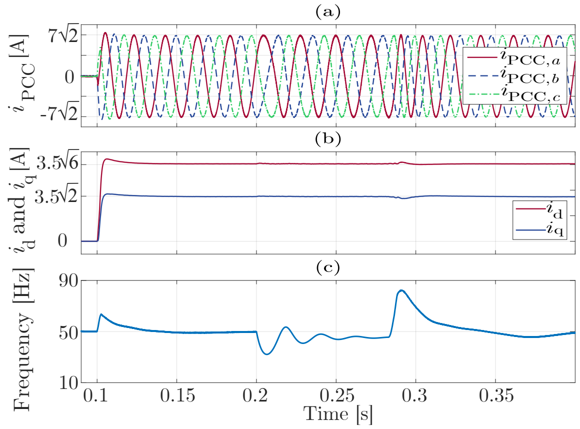

Figure 19: The simulation results of the system with I_{PCC}=7 A, X_{L_0}=5 Ω, R_L=1 Ω, and $\theta_I=\pi/6$ upon a step-change in the current at t=0.1 s, a three-phase solid fault at t=0.2 s, and fault clearance at t=0.28 s: a) three-phase grid currents (i_{PCC}), b) the dq-components of the grid current (i_{dq}), and c) the estimated grid frequency by the PLL.

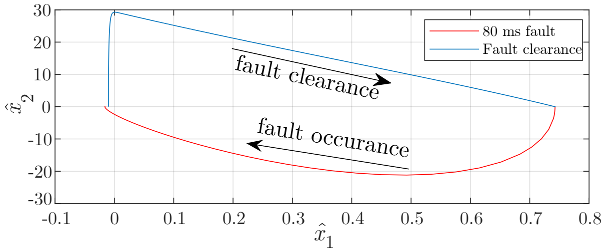

Figure 20: The treatment of the states of the system prior, during and after an 80 *ms solid fault.*

after the fault. Fig. 20 shows the change in the states of the system during the fault and after the fault clearance. As it is seen in this figure, the system is in its equilibrium point prior to the fault. After the fault is cleared, the states of the system are restored to the initial equilibrium point. The stable equilibrium point of the system after the fault is cleared is $(0.74, 0)$, which is the initial equilibrium point. This is because the structure of the system and the variables prior and after the fault are the same. If the states at the end of the fault are located in the domain of attraction of the post-fault's equilibrium point, they will converge to it. As discussed, to find a domain of attraction of the system, it is sufficient to evaluate $V(x_1, 0)$ and $\dot{V}(x_1, 0)$.

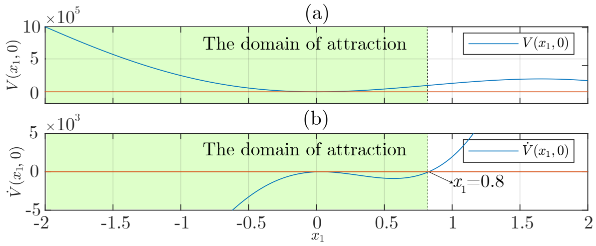

Figure 21: The domain of attraction of the equilibrium point of the system: a) a positive $V(x_1, 0)$ shows that the Lyapunov function does not impose a limitation on the radius of the domain of attraction, and b) $\dot{V}(x_1, 0)$ shows that there exists a ball with radius ρ=0.8 around the origin in which any initial condition necessarily is attracted to the equilibrium point. If the first state's initial condition (x_1^0) is located inside the green area, the states ultimately converge to the origin.

Fig. 21 shows $V(x_1, 0)$ and $\dot{V}(x_1, 0)$ of the system around the equilibrium point (for the equilibrium point transferred to the origin). It is seen that the radius of the domain of attraction is ρ=0.8. Thus, the states at

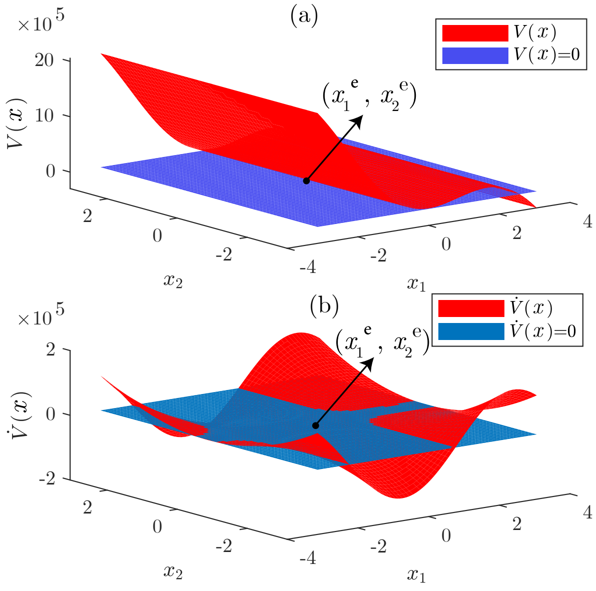

Figure 22: The chosen Lyapunov function and its derivative with respect to time: a) $V(x)$ and b) $\dot{V}(x)$.

the end of the fault are inside the post-fault's equilibrium point's domain of attraction. Hence, it is expected that after the fault clearance, the system recovers and operates at the pre-fault equilibrium point. This matches the simulation results as well. In Fig. 21, the area colored with green is inside the equilibrium point's domain of attraction, meaning any initial condition inside this region eventually converges to the origin. Also, Fig. 22 shows $V(x)$ and $\dot{V}(x)$ in a neighborhood around the equilibrium point. It is seen that, as expected, $V(x)$ is locally positive definite and $\dot{V}(x)$ is negative definite around the origin.

Experimental Results:

For validating the theory and the simulation results, an experimental platform based on a Semikron Semiteach converter, a NI CompactRio controller, and a Regatron AC power supply is used. The experimental setup is shown in Fig. 23, and its block diagram is similar to that of Fig.17. The control loops are implemented in LabVIEW. To control the VSC's current, a conventional vector current controller is used, and its PI controllers are chosen as $1000\frac{0.015s+1}{s}$. Three scenarios are considered for validating the correctness of the proposed method and ζ. In the first scenario, keeping all parameters constant, the RMS value of the injected current to the grid is increased. In the second scenario, the inductance of the grid is increased, and in the last scenario, the effectiveness of the proposed method in the presence of a fault is validated. In all cases, the initial condition of the system is stable with a non-zero ζ. In the first two scenarios, after the change is applied in the system, ζ becomes zero, indicating an unstable system. However, in the last scenario, it is shown that the system is stable prior to, during, and after the fault. Also, it is shown that based on the domain of attraction's radius, the states should be recovered to the pre-fault equilibrium point. The experimental results show that when the ζ becomes zero, the system becomes unstable.

Increasing the RMS Value of the Injected Current to the Grid:

In this test, the impact of changes in the VSC's injected current on the system stability is experimentally evaluated. The system of Fig. 17 is implemented, and its parameters are set according to Table 4. Initially, the VSC injects 12 A with θ_I=0. For these initial operating conditions, $D > 0$, and ζ is 0.1, which is a positive value. Therefore, it is expected to have a stable equilibrium point. At t=0.4 s, I_{PCC} is increased to 13 A, while θ_I is kept at zero. This makes ζ zero; hence, the system will become unstable. Fig. 24(a) depicts the dq-components of the VSC's current while the system's frequency extracted by the PLL is

Figure 23: The experimental setup used for validating the performance of the feedback linearization compensator.

Parameters	**Value**	**Description**
f_s	20 kHz	Switching Frequency
L_f	15 mH / 0.94 pu	Filter Inductance
R_f	1 Ω / 0.2 pu	Filter Resistance
V_dc	480 V	DC Link Voltage
V_g	100 V / 1 pu	Grid RMS Voltage
f	50 Hz	Grid Frequency
S_nominal	2 kVA / 1 pu	VSC Nominal Power
R_L	0.347 Ω / 0.07 pu	Grid Resistance
L_L	7.5 mH / 0.47 pu	Grid Inductance
SCR	2.1	Short Circuit Ratio
X/R	6.78	X/R Ratio
K_p	$0.04\ \frac{\mathrm{rad}}{V.s}$	PLL's Proportional Gain
K_i	$400\ \frac{\mathrm{rad}}{V.s^2}$	PLL's Integral Gain

Table 4: Experimental Setup's Parameters.

illustrated in Fig. 24(b). As predicted by ζ, the extracted frequency verifies the system loses its stability upon this change.

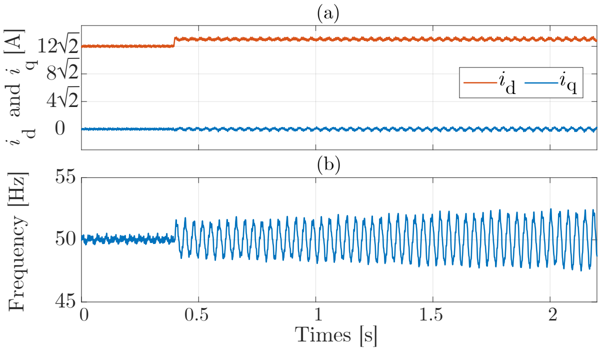

Figure 24: The experimental results of the system when I_{PCC} changes from 12 A to 13 A, at t=0.4 s, leading ζ=0: (a) the dq-components of the grid current (i_{dq}) and (b) the estimated grid frequency by the PLL.

Fault Occurrence:
In this test, the performance of the proposed method and index in the presence of a grid fault is experimentally evaluated. Similar to the previous tests, the system of Fig. 17 is implemented, and its parameters are

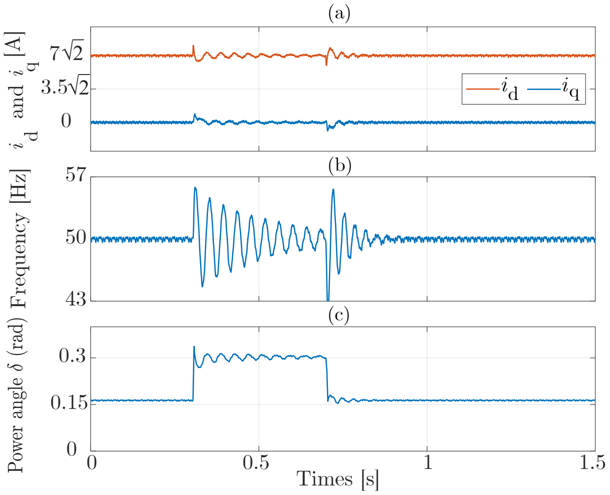

Figure 25: The experimental results of the system when I_{PCC}=7 A in the presence of a three-phase fault at the grid side: (a) the dq-components of the grid current (i_{dq}), (b) the estimated grid frequency by the PLL, and (c) the power angle.

set based on Table 4. In this test, the injected RMS current into the grid is 7 A. At t=0.3 s, a three-phase fault occurs at the grid side and is cleared after 400 ms. Upon this fault, the grid voltage drops to 0.6 pu during the fault and recovers after its clearance. The reason a deeper fault is not chosen is based on the system parameters, a deeper fault results in a system with no equilibrium point; hence, the system does not converge to any operating point during the fault. The initial operating point of the system is $(0.17, 0)$, and the domain of attraction's radius is ρ=0.84. During the fault, the operating point moves to $(0.3, 0)$, which is located inside the initial operating point's domain of attraction. Hence, it is expected that after the fault clearance, the states converge to the pre-fault equilibrium point. Fig. 25(a) depicts the dq-components of the VSC's current while the system's frequency extracted by the PLL is illustrated in Fig. 25(b). Additionally, the power angle is shown in Fig. 25(c). As predicted by the domain of attraction's radius, the states return to the initial equilibrium point after the fault is cleared.

3.2 Impact of PLL Dynamics and Grid Strength on the Stability and Output Power Capability of IBRs

This subsection examines the impact of PLL dynamics and grid strength on the stability and output power capability of inverter-based resources. Like the previous subsection, the main focus of this subsection is on GFLIs; however, GFMIs are also briefly discussed as a way of improving the GFLIs performance.

As shown in Fig. 26, the projected NEM maximum, average, and minimum instantaneous renewable penetration all show that while the renewable penetration is increasing, potential constraints are expected to decelerate the pace (see the shaded areas in the figure) [38]. This subsection discusses some of the primary sources of these constraints and how to address them.

While there are different types of limitations and constraints on the way toward 100% renewable penetration, synchronisation issues are focused on in this subsection. Synchronisation issues are categorised into two distinct groups. The first group of constraints is caused by the connected network, i.e., the connected grid strength, which is discussed in the previous subsection and will be explained here again with a new formulation. The other group of constraints is the constraints caused by the IBR itself, i.e., the IBR control system and, more specifically, the PLL impact. These constraints are discussed here because, for the highly penetrated networks with a high level of IBRs, these constraints may result in the installed renewable farms

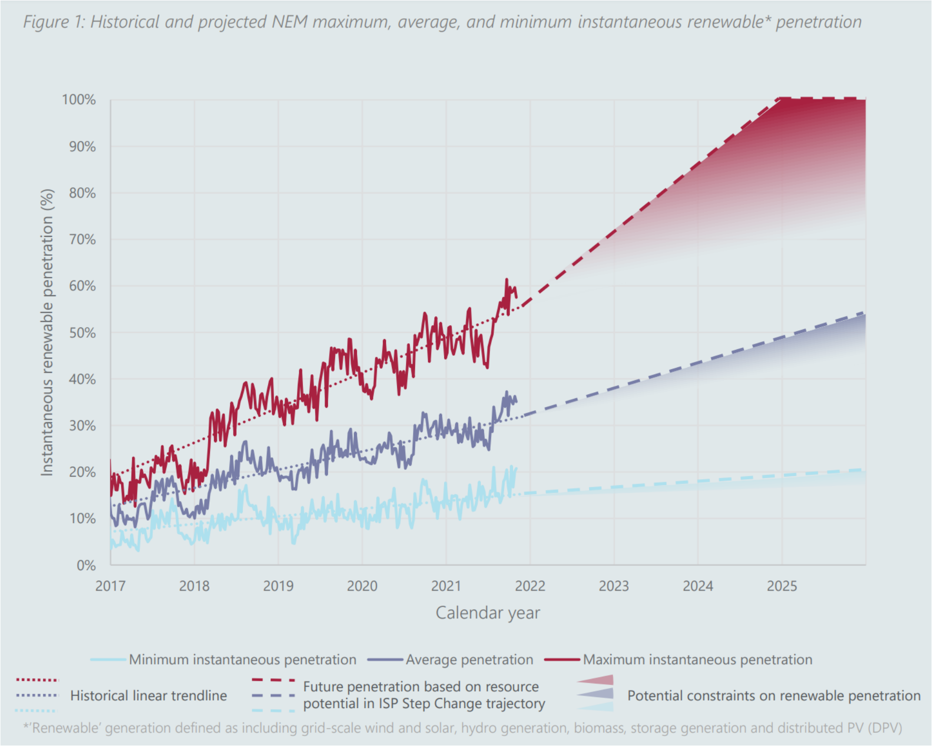

Figure 26: Historical and projected NEM instantaneous penetration [38].

not operating even at their rated power, and also, new farms cannot be installed anymore. Thus, these constraints are quantified in this study, and then some solutions will be provided.

3.2.1 Output Capability Curve

The tool used in this subsection is the OCC since the current study has come up with many complicated equations that will not be presented in this knowledge-sharing report. Instead, OCC can graphically illustrate the results of these derived equations. OCC defines the permitted active-reactive operating region for any generating unit in a system. As shown in Fig. 27(a), for a simple voltage source with nominal apparent power of S_{nom}, the very first limit for the operation is the thermal limit which can be shown with a circle, and the OCC of such a voltage source is the region inside this circle. For a synchronous generator, however, there are several limits rather than the thermal limit. Fig. 27(b) depicts some of them, including but not limited to the turbine limit (energy resource limit) and excitation system and armature limits. As shown in this figure, owing to the considered limits, the synchronous generator OCC is more confined and is not a circle anymore.

3.2.2 OCC of a GFLI

In this section, the OCC of an IBR is obtained. For an IBR, the operation mode, i.e., GFLIs, has a remarkable impact on the OCC. Starting from the SMIB case of a GFLI connected to an ideal grid through a transmission line shown in Fig. 28, five limits including 1) thermal limit, 2) stability (PLL) limit, 3) energy resource limit, 4) voltage limit and 5) static limit are considered and categorised into two categories: 1) caused by the inverter itself (limits 1-3) and 2) caused by the grid (limits 4 and 5). To obtain these limits for this system, several complicated equations have been derived in this study which, as mentioned earlier, are out of the scope of this report. Instead, only the corresponding curves on the OCC are shown in the following figures of this subsection. Moreover, owing to the importance of the static limit, (47) is provided

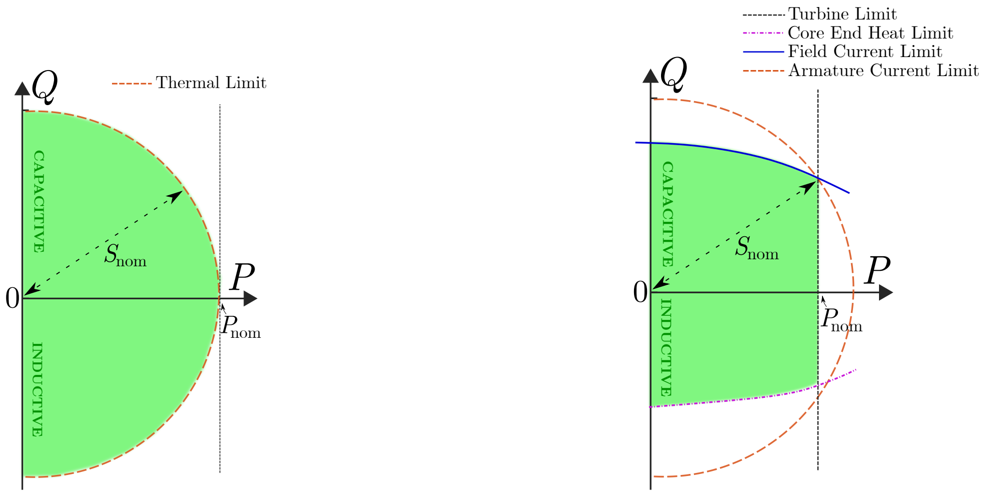

(a) *(b)*

Figure 27: OCC Curves of: a) a typical voltage source with only thermal limit, and b) a typical synchronous generator.

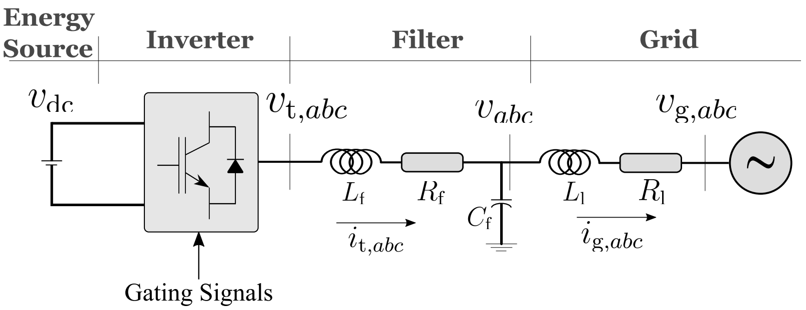

Figure 28: One-line diagram of the SMIB study system.

here, which shows the maximum transferable power of an IBR connected to a grid with short-circuit ratio of SCR and reactance to resistance ratio of $X_{\text{l}}/R_{\text{l}}$ when Q reference (Q_{ref}) is zero.

$$P_{\text{max}}^{\text{st}} = \frac{\text{SCR}}{2(1-\frac{1}{\sqrt{1+(\frac{X_{\text{l}}}{R_{\text{l}}})^2}})} P_{\text{nom}}, \tag{47}$$

According to this equation, if the grid is inductive (X/R is very high), then the IBR nominal power cannot be transferred for weak grids with $SCR \leq 2$. However, by injecting reactive power into the grid, this limit increases. Fig. 29 shows the OCC of a grid-following IBR for a typical case, and when the grids become weaker and the incorporated PLL is not tuned. As shown in Fig. 29(a), in addition to the thermal limit, other limits are also confining the GFLI OCC. For a normal IBR with a well-tuned PLL connected to a strong grid, the energy resource limit restricts the IBR output power; thus, the maximum transferable power of the IBR (when $Qref \geq 0$) is its nominal power, P_{nom}. However, as shown in Fig. 29(b), when the connected grid is very weak, the static limit trace goes upward in the Q-P plane and results in $P_{max}^{@Q=0} < P_{\text{nom}}$, which is in accordance with (47). Also, as shown in Fig. 29(c), if the PLL is not tuned, the PLL stability limit goes leftward and can be the active constraint and restrict the IBR output power to lower values.

Fig. 30(a) illustrates the Q-P trajectory of a grid-following IBR when it is controlled in the constant Q control mode. As shown in this figure, in this mode of control, the trajectory is a straight line and when the IBR is connected to a weak grid, if Q_{ref}=0, the maximum transferable power would be less than P_{nom},

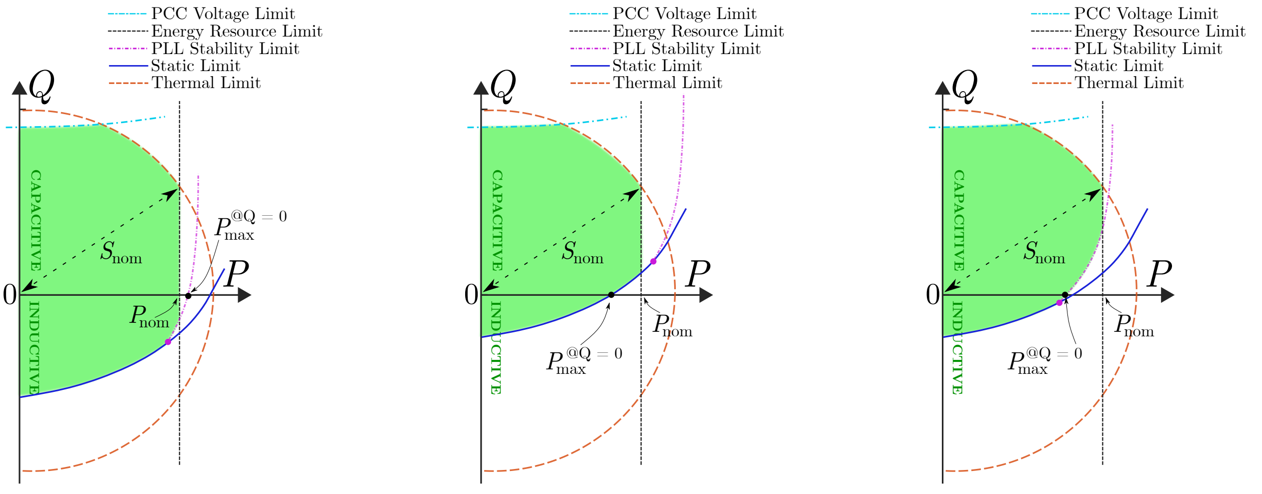

(a) *(b)* *(c)*

Figure 29: OCC Curves of a grid-following IBR: a) a typical case, b) when connected to a weaker grid, and c) when the PLL is also not tuned.

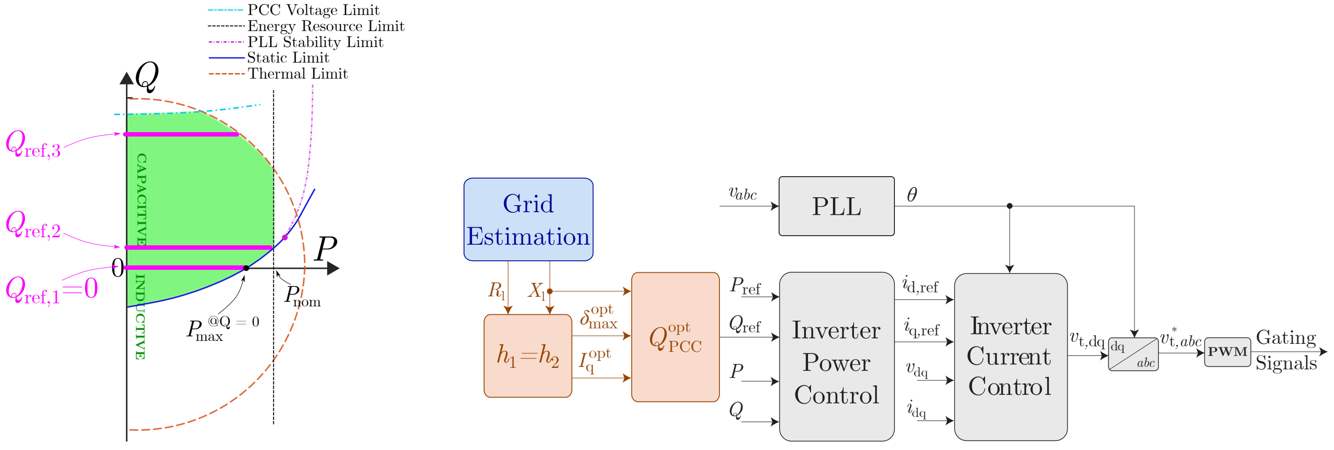

(a) *(b)*

Figure 30: (a) Q-P trajectory of a GFLI controlled in constant Q control mode and b) the proposed auxiliary controller for maximising the static limit.

and by increasing Q_{ref}, the maximum transferable power increases. However, as can be seen in Fig. 30(a), if Q_{ref} is too high ($Q_{\text{ref},3}$), the nominal power cannot be generated due to the presence of the thermal limit. Thus, there is an optimal value for injecting the reactive power for a specific case. In the current study, a control system has been proposed which can provide the optimal reference of Q to maximise the IBR static limit. Fig. 30(b) shows the block diagram of the proposed controller. As shown in this figure, the proposed controller includes an auxiliary loop that provides the optimal Q_{ref} for the conventional control units of a conventional GFLI.As can be seen, this control system requires estimating the grid impedance, which is discussed in other subsections of this report and is not discussed here.

3.2.3 Other Solutions for Increasing the GFLI Maximum Transferable Power

In the previous part, an auxiliary controller was proposed to address the static limit caused by the grid with low SCR. This part aims at providing some solutions for the PLL stability limit to increase the maximum transferable power of a GFLI.Since by changing the PLL gains the PLL stability limit can be pushed rightward in the OCC of a GFLI, re-tuning the PLL can be assumed to be the first solution. However, this method is not the best way since while the optimum PLL gains are functions of the grid impedance, the PLL gains are usually not changed after commissioning the IBR. The second solution is PLL passivation which is proposed and discussed in the following subsection of this report and is not discussed here. The third solution is to utilise PLL-less structures instead of conventional GFLIs.PSGFLIs and GFMIs are two PLL-less structures that can address the limitations caused by the PLL stability limit. These structures are also discussed in detail in the following parts of this report and are not the focus of the current section. However, owing to the importance of the grid-forming control mode, the OCC of a GFMI is also obtained here.

Two categories of limits can be considered for a GFMI , similar to the GFLIs.The first category includes the limits caused by the IBR control system, i.e., 1) the thermal limit and 2) the energy resource limit. The second category comprises the limits caused by the connected grid strength, i.e., 3) the voltage limit and 4) the static limit. As can be seen, there is no PLL limit which is one of the benefits of using GFMIs. Similar to the discussion for GFLIs, deriving and presenting the related equations for these limits is out of the scope of this report. Only the equation representing the static limit is presented here. Other limits are graphically illustrated as the OCC of the GFMI , shown in Fig. 31. Fig. 31 also depicts the Q-P trajectories of a GFMI for various GFMI voltage references V_{ref}. It can be seen that unlike Q-controlled GFLIs, the GFMI trajectories are not straight lines, and unless for very low V_{ref}s or very high V_{ref}s ($V_{\mathrm{ref},3}$), the nominal power can be transferred to the grid. The static limit of a GFMI can be obtained as

$$P_{\mathrm{max}}^{\mathrm{st}} = \mathrm{SCR}\Big(\frac{V_{\mathrm{ref}}}{V_{\mathrm{g}}} + (\frac{V_{\mathrm{ref}}}{V_{\mathrm{g}}})^2 \frac{1}{\sqrt{1+(\frac{X_{\mathrm{l}}}{R_{\mathrm{l}}})^2}}\Big) P_{\mathrm{nom}}. \tag{48}$$

where V_{g} denotes the grid voltage. It can be seen that if $V_{\mathrm{ref}}=V_{\mathrm{g}}$, for SCR$\leq$1, P_{max} is less than P_{nom} for an inductive grid, while for a GFLI, this condition was SCR$\leq$2, meaning that despite GFLIs which are not capable of transferring their nominal power for 1$\leq$SCR<2, GFMIs have not such limitation which is another benefit of employing GFMIs instead of GFLIs in weak parts of the grid.

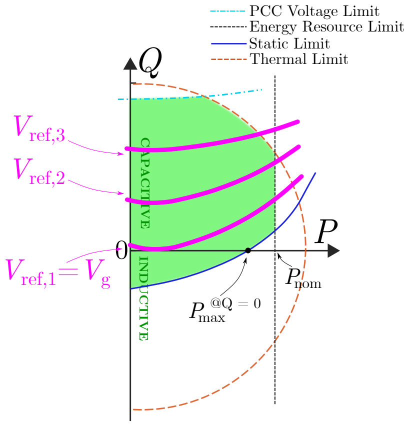

Figure 31: A typical GFMI OCC and its Q-P plane trajectories for various V_{ref} values.

3.2.4 Performance Evaluation

To verify the obtained findings of this study, a 1 MW battery system controllable in both grid-following and grid-forming modes with the structure shown in Fig. 28 is simulated in MATLAB/Simulink. Table 5 represents the parameters used in the simulations. A 2.2 kW experimental setup consisting of a Regatron AC Power Supply and an Imperix inverter with the parameters presented in Table 6 shown in Fig. 32 is

Quantity	Value (GFLI)	Value (GFMI)	Description
S_{nom}	1.0 MVA	1.0 MVA	Inverter Nominal Power
I_{rd}	836.7 A	836.7 A	Inverter Rated Current
V_{g}	690 V	690 V	Grid Voltage
V_{dc}	1150 V	1150 V	DC Bus Voltage
f_{sw}	5 kHz	5 kHz	Inverter Pulse-Width Modulation (PWM) Carrier Frequency
f	50 Hz	50 Hz	Nominal Frequency
L_{f}	95 μH	95 μH	Filter Inductance
R_{f}	0.01 Ω	0.01 Ω	Filter Resistance
C_{f}	-	1 mF	Filter Capacitance
L_{1}	417.7 μH	-	Grid Inductance (Stronger Grid)
R_{1}	16.4 mΩ	-	Grid Resistance (Stronger Grid)
L_{1}	1.253 mH	1.253 mH	Grid Inductance (Weaker Grid)
R_{1}	49.2 mΩ	49.2 mΩ	Grid Resistance (Weaker Grid)
K_p	0.3142	-	PLL Proportional Gain (Well-tuned PLL)
K_i	39.4784	-	PLL Integral Gain (Well-tuned PLL)
K_p	0.0628	-	PLL Proportional Gain (minimally-tuned PLL)
K_i	39.4784	-	PLL Integral Gain (minimally-tuned PLL)

Table 5: Parameters of the study system.

also assembled and utilised to validate the simulation results. In the simulations, six cases are simulated. In the first four cases, the IBR is controlled as a GFLI, and in the subsequent two cases, it is controlled as a GFMI . In all scenarios, the active power reference (P^*) is increased stepwise with the steps of 0.2 pu every second. The above cases are repeated in the experiments on a reduced IBR with a nominal power of 2.2 kW. In the first four cases, the experimental setup is controlled as a GFLI, and the reference of the d-component of the current is increased stepwise every 5 seconds with the steps of 3.26 A. In the last two cases, the experimental setup is in the grid-forming mode, and its active power reference is increased stepwise every 5 seconds with steps of 440 W.

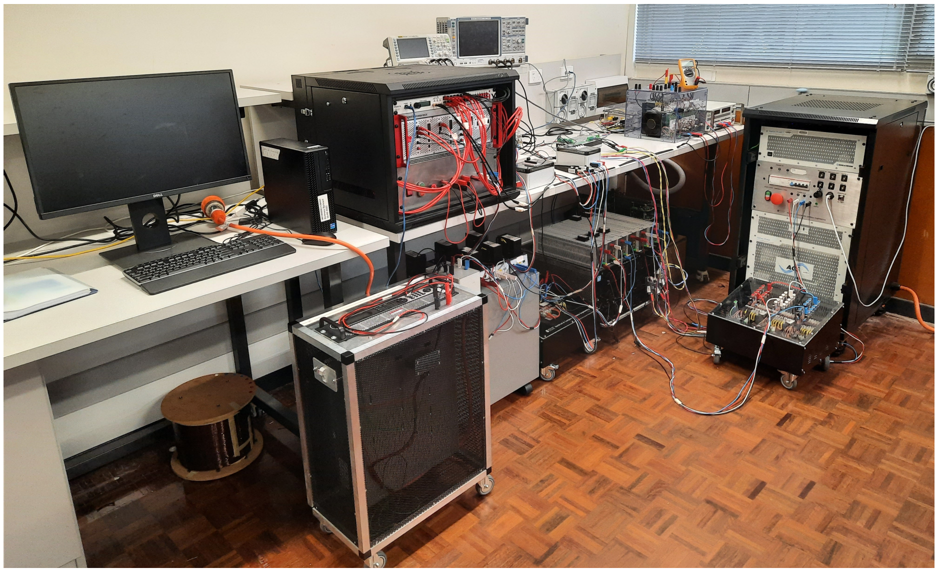

Figure 32: The experimental setup.

Figs. 33 and 34 illustrate the simulation and experimental results for all six cases, respectively. In Case 1, the IBR is in the grid-following mode, connected to a strong grid (SCR = 3.6), has a well-tuned PLL, and its reactive power reference is zero. In Case 2, the IBR is in the grid-following mode, connected to a weak grid (SCR = 1.2), has a minimally-tuned PLL, and its reactive power reference is zero. In Case 3, the IBR is in the grid-following mode, connected to a weak grid (SCR = 1.2), has a well-tuned PLL, and its reactive power reference is zero. In Case 4, the IBR is in the grid-following mode, connected to a weak grid (SCR = 1.2), has a well-tuned PLL, and its reactive power reference is determined by the proposed auxiliary controller. In Case 5, the IBR is in the grid-forming mode, connected to a weak grid (SCR = 1.2), and its voltage reference is 1.0 pu. In Case 6, the IBR is in the grid-forming mode, connected to a weak grid (SCR = 1.2), and its voltage reference is 0.9 pu. As can be seen in Figs. 33(a), (e), and (f) and 34(a), (e), and (f), unlike Case 1, in which the maximum transferable power is the IBR nominal

Quantity	Value (GFLI)	Value (GFMI)	Description
S_{nom}	2.2 kVA	2.2 kVA	Inverter Nominal Power
I_{rd}	11.5 A	11.5 A	Inverter Rated Current
V_{g}	110 V	110 V	Grid Voltage
V_{dc}	320 V	320 V	DC Bus Voltage
f_{sw}	20 kHz	20 kHz	Inverter PWM Carrier Frequency
f	50 Hz	50 Hz	Nominal Frequency
L_{f}	15 mH	15 mH	Filter Inductance
R_{f}	0.5 Ω	0.5 Ω	Filter Resistance
C_{f}	-	25 μF	Filter Capacitance
L_{l}	5.5 mH	-	Grid Inductance (Stronger Grid)
R_{l}	0.5 Ω	-	Grid Resistance (Stronger Grid)
L_{l}	16.3 mH	16.3 mH	Grid Inductance (Weaker Grid)
R_{l}	1.0 Ω	1.0 Ω	Grid Resistance (Weaker Grid)
K_p	0.2	-	PLL Proportional Gain (Well-tuned PLL)
K_i	40	-	PLL Integral Gain (Well-tuned PLL)
K_p	0.05	-	PLL Proportional Gain (Minimally-tuned PLL)
K_i	40	-	PLL Integral Gain (Minimally-tuned PLL)

Table 6: Parameters of the experimental setup.

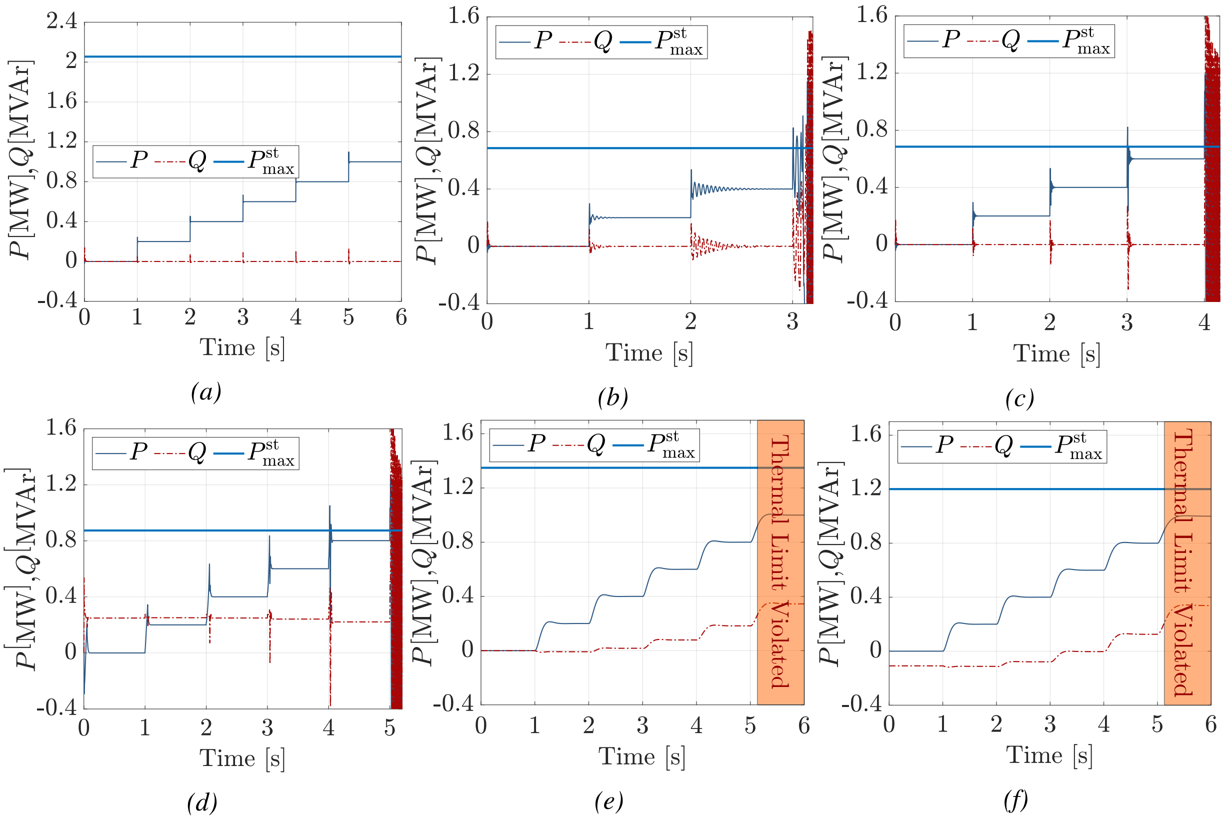

(a) (b) (c)

(d) (e) (f)

Figure 33: Simulation results for: a) Case 1, b) Case 2, c) Case 3, d) Case 4, e) Case 5, and f) Case 6.

power, in other cases, the maximum transferable power reduces, and only in the grid-forming mode the IBR can generate its nominal power by violating its thermal limit. Also, comparing Figs. 33(b) and 34(b) with Figs. 33(c) and 34(c) shows that tuning the PLL can improve the IBR maximum transferable power. Additionally, by optimally determining the IBR Q reference, Figs. 33(d) and 34(d) show that the proposed auxiliary controller increases the IBR maximum transferable power to that of Cases 5 and 6, where the IBR is in the grid-forming mode, and its thermal limit is not violated. All these cases explicitly comply with the study findings and validate the obtained equations.

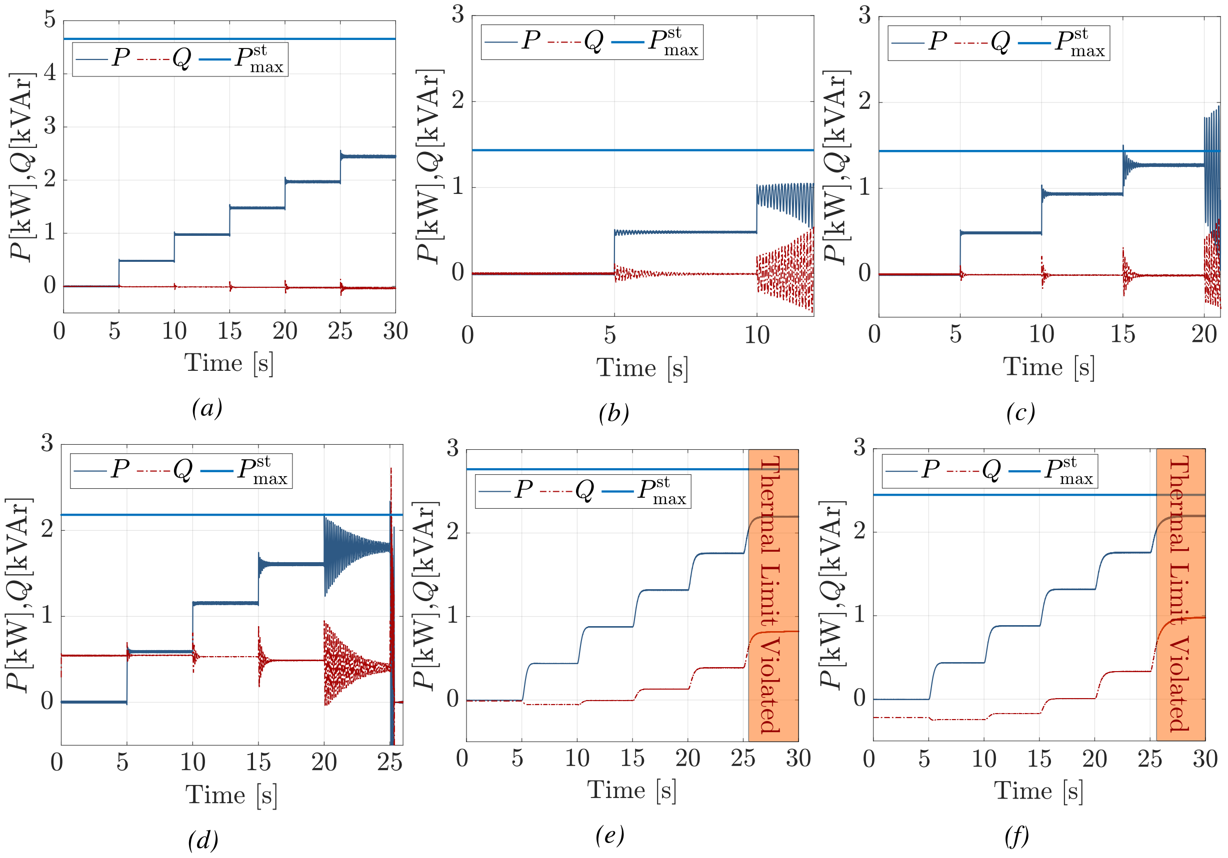

(a) (b) (c)

(d) (e) (f)

Figure 34: Experimental results for: a) Case 1, b) Case 2, c) Case 3, d) Case 4, e) Case 5, and f) Case 6.

3.3 Small-Signal Modelling, Stability Analysis, and Stability Enhancement of PLL-Based GFLIs

3.3.1 Small-Signal Modelling of GFLIs

Fig. 35(a) shows the block diagram of a typical Inductor-Capacitor-Inductor (LCL)-filtered GFLI equipped with the inner Current Control (CC) and SRF-PLL, of which the block diagrams are shown in Fig. 35(b) and Fig. 35(c), respectively. The inner CC includes the dq-axis decoupling capability and the grid voltage proportional feed-forward with the coefficient β. In addition, the SRF-PLL tracks the grid frequency to provide the reference angle for the current injection. The superscript c denotes that the variables are represented in the controller dq reference frame.

The inner CC loop includes three sub-modules, i.e., the inner CC with current controller $G_i(s) = K_{pi} + \frac{K_{ii}}{s}$ where converter gain $\frac{V_{dc}}{2}$ is considered, the time delay $G_{del}(s) = e^{-T_d s}$, and the LCL filter. T_d includes one sampling period of digital computational delay and a half sampling period of PWM delay, i.e., $T_d = 1.5T_s$. According to Fig. 35(b), the state-variable, input, and output vectors of the inner CC can be defined as $\overrightarrow{x_i} = \overrightarrow{\gamma_{idq}}$, $\overrightarrow{u_i} = \overrightarrow{i^{err}_{2dq}}$, and $\overrightarrow{y_i} = \overrightarrow{v^{c}_{m0dq}}$, respectively, where $\overrightarrow{\gamma_{idq}}$ is the integrator output of $G_i(s)$. The SSM of the inner current controller can then be derived as

$$\Delta \dot{\overrightarrow{x_i}} = A_i \Delta\overrightarrow{x_i} + B_i \Delta\overrightarrow{u_i}, \qquad \Delta\overrightarrow{y_i} = C_i \Delta\overrightarrow{x_i} + D_i \Delta\overrightarrow{u_i}, \tag{49}$$

where the symbol Δ denotes the small-signal perturbation. $A_i = \mathbf{O}_{2\times 2}$, $B_i = [1, 0; 0, 1]$, $C_i = \left[K_{ii}, 0; 0, K_{ii}\right]$, and $D_i = \left[K_{pi}, 0; 0, K_{pi}\right]$.

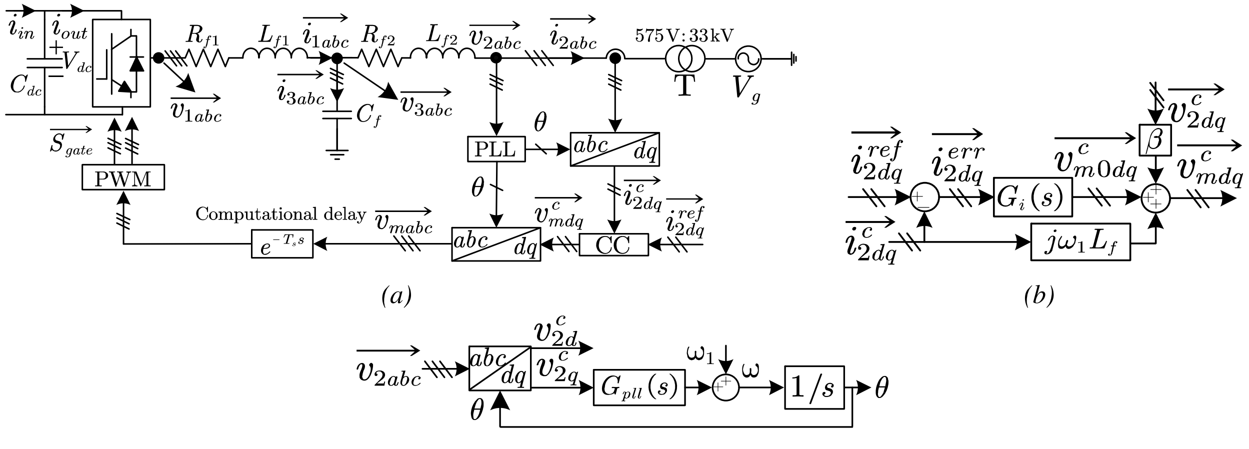

(a)

(b)

(c)

Figure 35: The block diagrams of (a) the GFLI with inner CC and SRF-PLL, (b) the inner CC, and (c) the SRF-PLL.

By using the third-order Pade approximation, $G_{del}(s)$ can be reformulated as

$$G_{del}(s) = e^{-T_d s} \approx \frac{120 - 60T_d s + 12\left(T_d s\right)^2 - \left(T_d s\right)^3}{120 + 60T_d s + 12\left(T_d s\right)^2 + \left(T_d s\right)^3}. \tag{50}$$

According to Fig. 35(a) and (50), the state-variable, input, and output vectors of the time delay can be defined as $\overrightarrow{x_{del}} = \left[x_{del\_d1}; x_{del\_d2}; x_{del\_d3}; x_{del\_q1}; x_{del\_q2}; x_{del\_q3}\right]$, $\overrightarrow{u_{del}} = \overrightarrow{v^c_{mdq}}$, $\overrightarrow{y_{del}} = \overrightarrow{v^c_{1dq}}$, respectively, based on which its SSM can be derived as

$$\Delta \dot{\overrightarrow{x_{del}}} = A_{del}\Delta\overrightarrow{x_{del}} + B_{del}\Delta\overrightarrow{u_{del}}, \qquad \Delta\overrightarrow{y_{del}} = C_{del}\Delta\overrightarrow{x_{del}} + D_{del}\Delta\overrightarrow{u_{del}}, \tag{51}$$

where A_{del}-D_{del} are omitted for brevity. Note that the converter gain is regarded as 1, since its gain $\frac{V_{dc}}{2}$ has been considered in $G_i(s)$.

According to Fig. 35(a), the state-variable, input, and output vectors of the LCL filter can be defined as $\overrightarrow{x_{lcl}} = \left[\overrightarrow{i^c_{1dq}}; \overrightarrow{i^c_{2dq}}; \overrightarrow{v^c_{3dq}}\right]$, $\overrightarrow{u_{lcl}} = \left[\ \overrightarrow{v^c_{1dq}}; \overrightarrow{v^c_{2dq}}\ \right]$, and $\overrightarrow{y_{lcl}} = \overrightarrow{i^c_{2dq}}$, respectively, based on which its SSM can be derived as

$$\Delta \dot{\overrightarrow{x_{lcl}}} = A_{lcl}\Delta\overrightarrow{x_{lcl}} + B_{lcl}\Delta\overrightarrow{u_{lcl}}, \qquad \Delta\overrightarrow{y_{lcl}} = C_{lcl}\Delta\overrightarrow{x_{lcl}} + D_{lcl}\Delta\overrightarrow{u_{lcl}}, \tag{52}$$

where A_{lcl}-D_{lcl} are omitted for brevity. To derive the State-Space Representation (SSR) of the CC-GFLI using the Component Connection Method (CCM) presented by [39], the stacked input and output vectors of the three sub-modules can be defined as $\overrightarrow{u_{stac0}} = \left[\overrightarrow{u_i}; \overrightarrow{u_{del}}; \overrightarrow{u_{lcl}}\right]$ and $\overrightarrow{y_{stac0}} = \left[\overrightarrow{y_i}; \overrightarrow{y_{del}}; \overrightarrow{y_{lcl}}\right]$, respectively. According to Fig. 35(a), the input and output vectors of the whole system can be defined as $\overrightarrow{u_{vsc1}} = \left[\ \overrightarrow{i^{ref}_{2dq}}; \overrightarrow{v^c_{2dq}}\ \right]$ and $\overrightarrow{y_{vsc1}} = \overrightarrow{i^c_{2dq}}$, respectively. By solving

$$\Delta\overrightarrow{u_{stac0}} = R_{-3}\Delta\overrightarrow{y_{stac0}} + R_{-2}\Delta\overrightarrow{u_{vsc1}}, \qquad \Delta\overrightarrow{y_{vsc1}} = R_{-1}\Delta\overrightarrow{y_{stac0}} + R_0\Delta\overrightarrow{u_{vsc1}}, \tag{53}$$

one can derive the relationship between the stacked input/output vectors and the system input/output

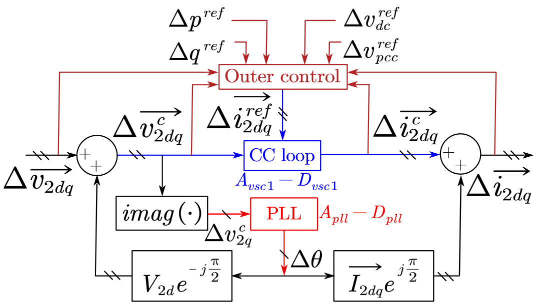

Figure 36: The interconnection relationship between the inner CC loop, PLL, and outer power/voltage control.

vectors as

$$R_{-3}=\begin{bmatrix}0&0&0&0&-1&0\\0&0&0&0&0&-1\\1&0&0&0&0&-\omega_1(L_{f1}+L_{f2})\\0&1&0&0&\omega_1(L_{f1}+L_{f2})&0\\0&0&1&0&0&0\\0&0&0&1&0&0\\0&0&0&0&0&0\\0&0&0&0&0&0\end{bmatrix},\ R_{-2}=\begin{bmatrix}1&0&0&0\\0&1&0&0\\0&0&\beta&0\\0&0&0&\beta\\0&0&0&0\\0&0&0&0\\0&0&1&0\\0&0&0&1\end{bmatrix},$$

$R_{-1}=[0,0,0,0,1,0;0,0,0,0,0,1]$ and $R_0=\mathbf{O}_{2\times4}$. By defining state-variable vector of the whole system as $\overrightarrow{x_{vsc1}}=\left[\overrightarrow{x_i};\overrightarrow{x_{del}};\overrightarrow{x_{lcl}}\right]$ and assuming that the SSR of the CC-GFLI is

$$\Delta\dot{\overrightarrow{x_{vsc1}}}=A_{vsc1}\Delta\overrightarrow{x_{vsc1}}+B_{vsc1}\Delta\overrightarrow{u_{vsc1}},\qquad\Delta\overrightarrow{y_{vsc1}}=C_{vsc1}\Delta\overrightarrow{x_{vsc1}}+D_{vsc1}\Delta\overrightarrow{u_{vsc1}},\tag{54}$$

one can write that

$$\begin{aligned}A_{vsc1}&=A_{stac0}+B_{stac0}R_{-3}(I_{6\times6}-D_{stac0}R_{-3})^{-1}C_{stac0}\\B_{vsc1}&=B_{stac0}R_{-3}(I_{6\times6}-D_{stac0}R_{-3})^{-1}D_{stac0}R_{-2}+B_{stac0}R_{-2}\\C_{vsc1}&=R_{-1}(I_{6\times6}-D_{stac0}R_{-3})^{-1}C_{stac0}\\D_{vsc1}&=R_{-1}(I_{6\times6}-D_{stac0}R_{-3})^{-1}D_{stac0}R_{-2}+R_0,\end{aligned}\tag{55}$$

where A_{vsc1}-D_{vsc1} are omitted for brevity. Based on (54), the small-signal behavior of the inner CC loop is drawn as the blue part in Fig. 36.

Fig. 37(a) shows the time-domain comparison between the MATLAB/Simulink benchmark model with the ideal PLL (i.e., $\overrightarrow{v_{2dq}}=\overrightarrow{v_{2dq}^{c}}$ and $\overrightarrow{i_{2dq}}=\overrightarrow{i_{2dq}^{c}}$) and the linearized 14th-order SSR in (54) for a step up of i_{2d}^{ref} from 3195 A to 3408 A at 10 s and a step up of i_{2q}^{ref} from 0 A to 426 A at 20 s. It can be seen that i_{2d}^{sim} and i_{2q}^{sim} of the simulation model highly agree with i_{2d}^{ssm} and i_{2q}^{ssm} of the derived SSR, which validates the correctness of the derived SSR in (54).

Eq. (54) can be reformulated as

$$\Delta\overrightarrow{y_{vsc1}}=\left(C_{vsc1}\left(sI_{14\times14}-A_{vsc1}\right)^{-1}B_{vsc1}+D_{vsc1}\right)\Delta\overrightarrow{u_{vsc1}}=\left[G_{vsc1}^{cl}\quad -Y_{vsc1}\right]\Delta\overrightarrow{u_{vsc1}},\tag{56}$$

where Y_{vsc1} is the dq-domain input Admittance Representation (AR) of the CC-GFLI. Fig. 37(b) plots the Bode diagrams of the dd-and qq-axis elements of Y_{vsc1} with the current reference point (3195 A, 0 A) and under three current controller configurations (K_{pi}, K_{ii}), i.e., ($1.7391\times10^{-4}\ \Omega$, $3.4782\times10^{-2}\ \Omega/s$),

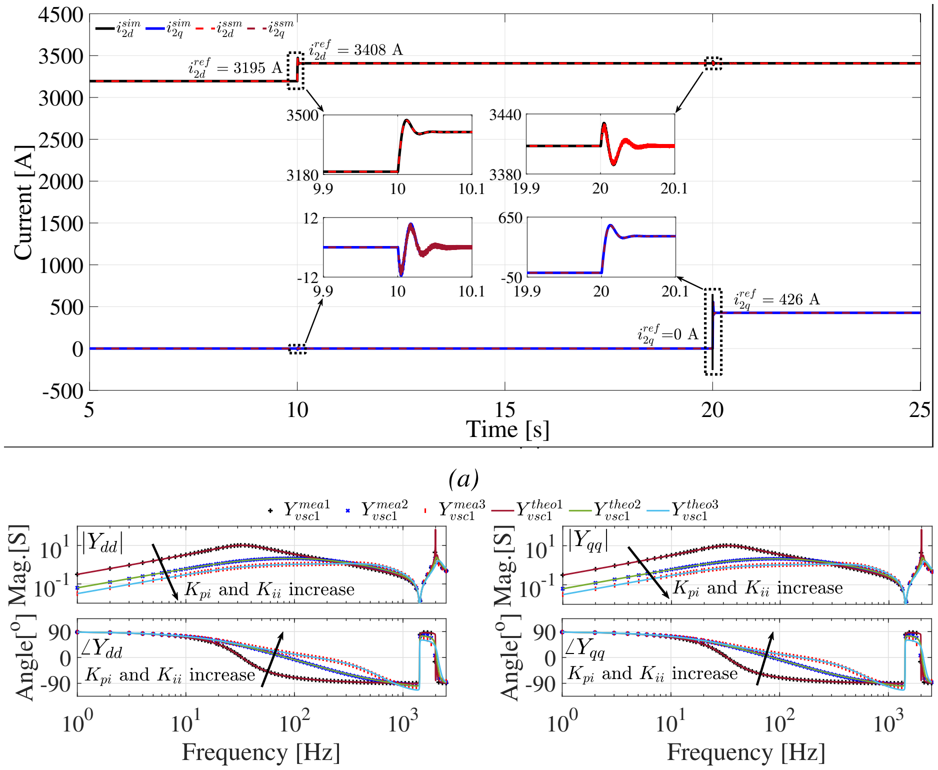

(a)

(b)

Figure 37: (a) Time-domain and (b) frequency-domain verification of the derived SSM of the control mode #1 CC-GFLI.

(8.6955×10^{-4} Ω, 1.7391×10^{-1} Ω$/s$), and (1.7391×10^{-3} Ω, 3.4782×10^{-1} Ω$/s$). It can be seen that the two admittance elements are the same, which results from the symmetric structure of the inner CC loop. In addition, the three measured admittance frequency responses (e.g., Y_{vsc1}^{mea1}, Y_{vsc1}^{mea2}, and Y_{vsc1}^{mea3}) agree with the three theoretical admittance frequency responses (e.g., Y_{vsc1}^{theo1}, Y_{vsc1}^{theo2}, and Y_{vsc1}^{theo3}) very well, which validates the correctness of the derived input AR in (56).

The state-variable vector of the PLL with $G_{pll}(s) = K_{ppll} + \frac{K_{ipll}}{s}$ in Fig. 35(c) can be defined as $\overrightarrow{x_{pll}} = [\theta; \phi_{pll}]$, where $\phi_{pll} = \int v_{2q}^{c} dt$. By further defining the input and output vectors of the PLL as $\overrightarrow{u_{pll}} = v_{2q}^{c}$ and $\overrightarrow{y_{pll}} = \theta$, respectively, one can write that

$$\Delta \dot{\overrightarrow{x_{pll}}} = A_{pll}\Delta\overrightarrow{x_{\text{pll}}} + B_{pll}\Delta\overrightarrow{u_{pll}}, \qquad \Delta\overrightarrow{y_{pll}} = C_{pll}\Delta\overrightarrow{x_{pll}} + D_{pll}\Delta\overrightarrow{u_{pll}}, \tag{57}$$

where $A_{pll} = [0, K_{ipll}; 0, 0]$, $B_{pll} = [K_{ppll}; 1]$, $C_{pll} = [1, 0]$, and $D_{pll} = 0$. Based on (57), the small-signal behavior of the PLL is drawn as the red part in Fig. 36.

Based on the interconnection relationship between the inner CC loop and PLL in Fig. 36, the SSR of the CC-PLL-GFLI can be derived by CCM. Specifically, by defining $\overrightarrow{u_{stac1}} = [\overrightarrow{u_{vsc1}}; \overrightarrow{u_{pll}}]$, $\overrightarrow{y_{stac1}} = [\overrightarrow{y_{vsc1}}; \overrightarrow{y_{pll}}]$, $\overrightarrow{x_{vsc2}} = [\overrightarrow{x_{vsc1}}; \overrightarrow{x_{pll}}]$, $\overrightarrow{u_{vsc2}} = \left[\overrightarrow{i_{2dq}^{ref}}; \overrightarrow{v_{2dq}}\right]$, and $\overrightarrow{y_{vsc2}} = \overrightarrow{i_{2dq}}$, and solving

$$\Delta\overrightarrow{u_{stac1}} = R_1\Delta\overrightarrow{y_{stac1}} + R_2\Delta\overrightarrow{u_{vsc2}}, \qquad \Delta\overrightarrow{y_{vsc2}} = R_3\Delta\overrightarrow{y_{stac1}} + R_4\Delta\overrightarrow{u_{vsc2}}, \tag{58}$$

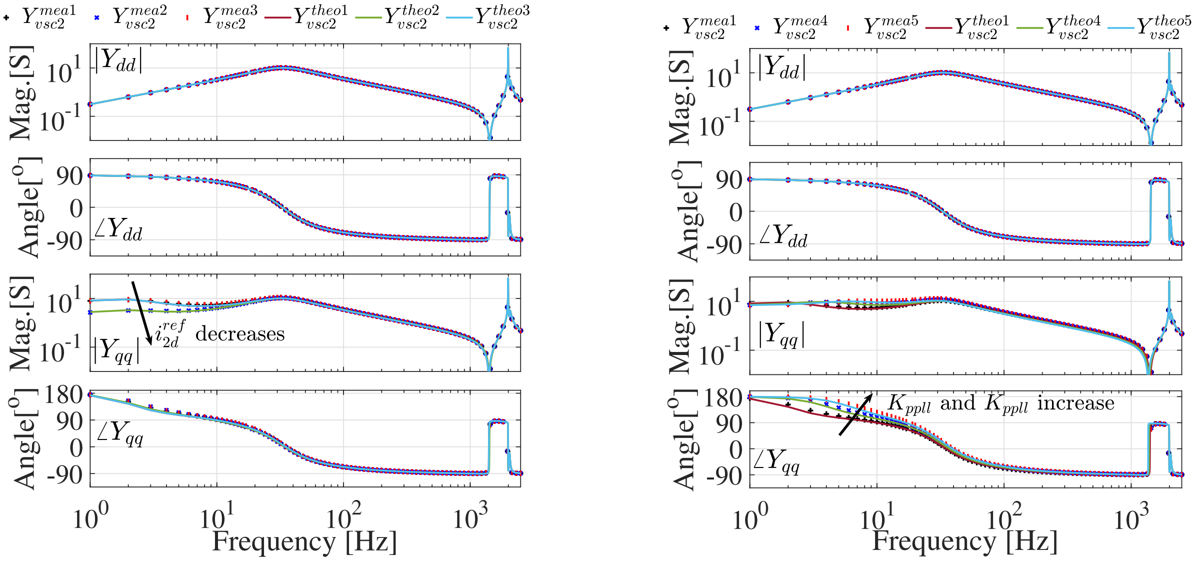

(a) (b)

Figure 38: Frequency-domain verification of the derived SSM of the control mode #2 CC-PLL-GFLI by changing (a) current reference point and (b) PLL parameters.

one can write that

$$R_1 = \begin{bmatrix} 0 & 0 & 0 \\ 0 & 0 & 0 \\ 0 & 0 & 0 \\ 0 & 0 & -V_{2d} \\ 0 & 0 & -V_{2d} \end{bmatrix}, R_2 = \begin{bmatrix} 1 & 0 & 0 & 0 \\ 0 & 1 & 0 & 0 \\ 0 & 0 & 1 & 0 \\ 0 & 0 & 0 & 1 \\ 0 & 0 & 0 & 1 \end{bmatrix}, R_3 = \begin{bmatrix} 1 & 0 \\ 0 & 1 \\ -I_{2q} & I_{2d} \end{bmatrix}^T,$$

and $R_4 = \mathbf{O}_{2\times4}$. Assuming that the SSR of the CC-PLL-GFLI is

$$\Delta \dot{\overrightarrow{x_{vsc2}}} = A_{vsc2}\Delta\overrightarrow{x_{vsc2}} + B_{vsc2}\Delta\overrightarrow{u_{vsc2}}, \qquad \Delta\overrightarrow{y_{vsc2}} = C_{vsc2}\Delta\overrightarrow{x_{vsc2}} + D_{vsc2}\Delta\overrightarrow{u_{vsc2}}, \tag{59}$$

one can write that

$$\begin{aligned} A_{vsc2} &= A_{stac1} + B_{stac1}R_1(I_{3\times3} - D_{stac1}R_1)^{-1}C_{stac1} \\ B_{vsc2} &= B_{stac1}R_1(I_{3\times3} - D_{stac1}R_1)^{-1}D_{stac1}R_2 + B_{stac1}R_2 \\ C_{vsc2} &= R_3(I_{3\times3} - D_{stac1}R_1)^{-1}C_{stac1} \\ D_{vsc2} &= R_3(I_{3\times3} - D_{stac1}R_1)^{-1}D_{stac1}R_2 + R_4, \end{aligned} \tag{60}$$

where $X_{stac1} = diag(X_{vsc1}, X_{pll})(X = A, B, C, D)$, and A_{vsc2}-D_{vsc2} are omitted for brevity.

Eq. (59) can be reformulated as

$$\Delta\overrightarrow{y_{vsc2}} = \left(C_{vsc2}\left(sI_{16\times16} - A_{vsc2}\right)^{-1}B_{vsc2} + D_{vsc2}\right)\Delta\overrightarrow{u_{vsc2}} = \left[G^{cl}_{vsc2} \quad -Y_{vsc2}\right]\Delta\overrightarrow{u_{vsc2}}, \tag{61}$$

where Y_{vsc2} is the dq-domain input AR of the CC-PLL-GFLI. Fig. 38(a) plots the Bode diagrams of the dd-and qq-axis elements of Y_{vsc2} with (K_{ppll}, K_{ipll}) as (20 rad/(Vs), 200 rad/(Vs^2)) and under three current reference points $(i^{ref}_{2d}, i^{ref}_{2q})$, i.e., (3195 A, 0 A), (1065 A, 0 A), and (3195 A, −2132 A). Furthermore, Fig. 38(b) plots the Bode diagrams of the dd-and qq-axis elements of Y_{vsc2} with the current

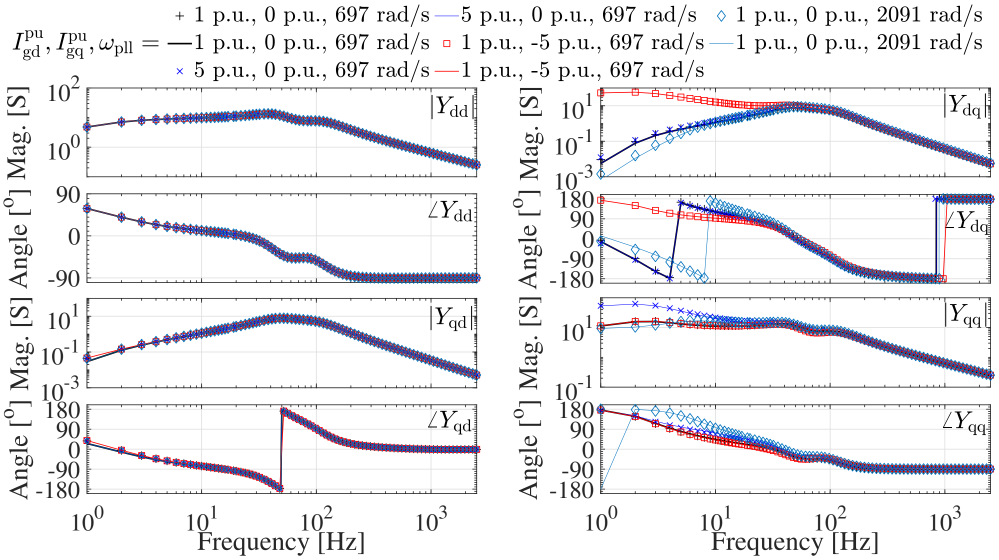

Figure 39: Effects of active current $I_{\mathrm{gd}}^{\mathrm{pu}}$, reactive current $I_{\mathrm{gq}}^{\mathrm{pu}}$, and PLL bandwidth ω_{pll} on input admittance $Y_{\mathrm{cl}}^{\mathrm{pllm}}$ of the ACC-PLL GFLI.

reference point (i_{2d}^{ref}, i_{2q}^{ref}) as (3195 A, 0 A) and under three PLL controller configurations (K_{ppll}, K_{ipll}), i.e., (20 rad/(Vs), 200 rad/(Vs)), (40 rad/(Vs), 800 rad/(Vs^2)), and (60 rad/(Vs), 1800 rad/(Vs^2)). It can be seen that the measured admittance frequency responses (e.g., Y_{vsc2}^{mea1}-Y_{vsc2}^{mea5}) agree with the theoretical admittance frequency responses (e.g., Y_{vsc2}^{theo1}-Y_{vsc2}^{theo5}) very well, which validates the correctness of the derived input AR in (61).

3.3.2 Small-Signal Stability Analysis of GFLIs

Fig. 39 plots the Bode diagrams of the measured (i.e., the marked lines) and the derived (i.e., the solid lines) input admittance $Y_{\mathrm{cl}}^{\mathrm{pllm}}$ of the Alternating Current Control (ACC)-PLL GFLI. Note that the grid is emulated as an ideal voltage source to keep the Point of Common Coupling (PCC) voltage $v_{2\mathrm{d}}$ constant. Clearly, more active power injection increases only qq-axis admittance magnitude, whereas more reactive power absorption increases only dq-axis admittance magnitude. The PLL affects only dq- and qq-axis admittance components.

Fig. 40(a) and (b) illustrate the variation of the maximum transferable active power $p_{\mathrm{gfli1}}^{\mathrm{pu}}$ of the ACC-PLL-GFLI as reactive power q^{pu} and SCR vary, respectively. Fig. 40(a) shows that the PLL-induced Maximum Power Transfer Capability (MPTC) $p_{\mathrm{pll\_max}}^{\mathrm{pu}}$ slightly changes as q^{pu} varies and decreases as the PLL bandwidth ω_{pll} increases. The effects of q^{pu} on $p_{\mathrm{pll\_max}}^{\mathrm{pu}}$ and power-angle-constrained MPTC $p_{\mathrm{max1}}^{\mathrm{pu}}$ are opposite, and the smaller one determines $p_{\mathrm{gfli1}}^{\mathrm{pu}}$. Fig. 40(b) shows that a larger SCR increases both the power-angle-constrained MPTC $p_{\mathrm{max2}}^{\mathrm{pu}}$ and $p_{\mathrm{pll\_max}}^{\mathrm{pu}}$. Specifically, the PLL and the power angle relation determines $p_{\mathrm{gfli1}}^{\mathrm{pu}}$ under small and large SCR grid conditions, respectively.

Fig. 41 shows the eigenvalue loci of the ACC-PLL-GFLI-Grid composite system. Note that constant PCC voltage $v_{2\mathrm{d}}$ is assumed to avoid the power-angle relation violation. It shows that the PLL-induced eigenvalue pair is within the right-half plane if high active power is injected. Fig. 41(a) indicates that decreasing SCR from 3.0 to 2.0 and 1.0 with $\phi = 80°$ decreases $p_{\mathrm{pll\_max}}^{\mathrm{pu}}$ from 2.6 p.u. to 1.1 and 0.1 p.u.. Fig. 41(b) indicates that increasing ω_{pll} from 697 rad/s to 1394 and 2091 rad/s slightly decreases $p_{\mathrm{pll\_max}}^{\mathrm{pu}}$ from 1.1 p.u. to 1.0 and 0.9 p.u.. Fig. 41(c) indicates that increasing q^{pu} from -0.3 p.u. to -0.6 and -0.9 p.u.

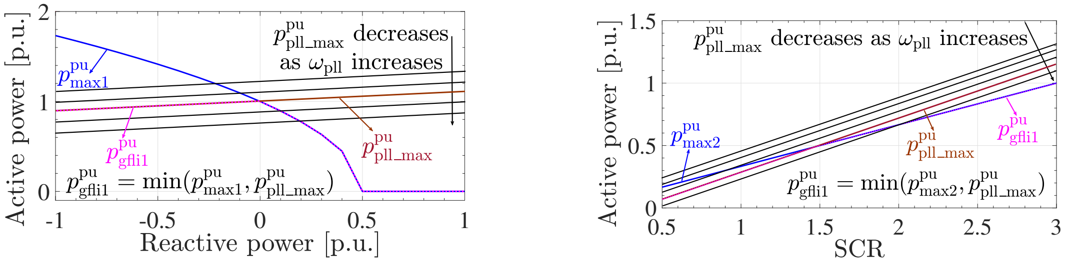

(a) *(b)*

Figure 40: Illustration of (a) reactive power effects under SCR = 3.0 with $\phi = 90°$ and different PLL bandwidth ω_{pll}, and (b) effects of different SCRs with $\phi = 90°$ under different PLL bandwidth ω_{pll} without reactive power injection on the MPTC $p^{\text{pu}}_{\text{gfli1}}$ of the ACC-PLL GFLI.

decreases $p^{\text{pu}}_{\text{pll\_max}}$ from 0.9 p.u. to 0.6 and 0.4 p.u.. These eigenvalue loci agree with the illustrations in Fig. 40. Fig. 41(d) indicates that increasing the ACC bandwidth ω_{acc} from 400 rad/s to 4000 and 8000 rad/s improves low-frequency stability. However, the time-delay-induced high-frequency stability is violated as ω_{acc} increases. A trade-off between high- and low-frequency stability thus needs consideration when tuning ACC.

Fig. 42(a) shows simulation results of ACC-PLL-GFLI-Grid composite system as SCR = 1.0 with $\phi = 80°$ and $\omega_{\text{acc}} = 400$ rad/s. Clearly, when $q^{\text{pu}}_{\text{ref}} = 0$ p.u. and $\omega_{\text{pll}} = 697$ rad/s, system becomes unstable and oscillates at 1.8 Hz if $p^{\text{pu}}_{\text{ref}}$ increases from 0.1 p.u. to 0.15 p.u. at 25 s, which agrees with Fig. 41(a). 0.35 p.u. active power can be injected stably by decreasing ω_{pll} from 697 rad/s to 69.7 rad/s at 30 s, which agrees with Fig. 41(b). The system is unstable as 0.41 p.u. active power is injected at 45 s, and is stable as -0.5 p.u. reactive power is injected at 48 s. The power-angle-constrained MPTC without reactive power injection (i.e., $p^{\text{pu}}_{\text{max2}}$) and with -0.5 p.u. reactive power injection (i.e., $p^{\text{pu}}_{\text{max1}}$) is 0.4 p.u. and 1.6 p.u., respectively. Therefore, the instability behaviors from 25 s to 30 s and from 45 s to 48 s result from adverse control interaction and power-angle-relation violation, respectively. Fig. 42(b) shows simulation results as SCR = 2.0 with $\phi = 80°$, $\omega_{\text{pll}} = 697$ rad/s, $p^{\text{pu}}_{\text{ref}} = 0.1$ p.u., and $q^{\text{pu}}_{\text{ref}} = 0$ p.u.. Clearly, the system oscillates at 240 Hz when ω_{acc} increases from 4000 rad/s to 8000 rad/s at 1 s, which agrees with Fig. 41(d).

Since increasing active power injection under inductive grid slightly decreases PCC voltage $v_{2\text{d}}$, leading to slightly increased PLL-related admittance components and thus slightly decreased stability margin, the PLL-induced MPTC obtained from Fig. 41(a), (b), and (d) may be slightly larger than the actual PLL-induced MPTC. Specifically, PLL-induced MPTC as SCR = 1.0 slightly decreases from 0.119 p.u. in Fig. 41(a) to 0.118 p.u. in Fig. 43(a). Since increasing reactive power absorption under inductive grid condition significantly increases $v_{2\text{d}}$, leading to clearly decreased PLL-related admittance components and thus increased stability margin, the PLL-induced MPTC obtained from Fig. 41(c) may be clearly smaller than the actual PLL-induced MPTC. Specifically, PLL-induced MPTC as q^{pu} is -0.3 and -0.9 p.u. increases from 0.90 and 0.48 p.u. in Fig. 41(c) to 1.00 and 1.00 p.u. in Fig. 43(b). However, the MPTC decreases if reactive power absorption increases to -1.2 and -1.5 p.u.. The oscillation frequency slightly decreases as reactive power absorption increases. Fig. 43(c) shows the simulation verification of Fig. 43(b).

Several insights into the MPTC of the ACC-PLL GFLI can be obtained. First, although ACC itself does not limit the MPTC, the PLL-induced MPTC $p^{\text{pu}}_{\text{pll\_max}}$ decreases as ACC bandwidth ω_{acc} decreases. Second, the power-angle-induced MPTC $p^{\text{pu}}_{\text{max1}}$ can be regarded as the theoretical upper limit whichever control strategy is employed. The maximum transferable active power $p^{\text{pu}}_{\text{gfli1}}$ decreases from $p^{\text{pu}}_{\text{max1}}$ to $p^{\text{pu}}_{\text{pll\_max}}$ if the PLL bandwidth ω_{pll} is large enough. Third, increasing SCR increases both $p^{\text{pu}}_{\text{max1}}$ and $p^{\text{pu}}_{\text{pll\_max}}$, whereas

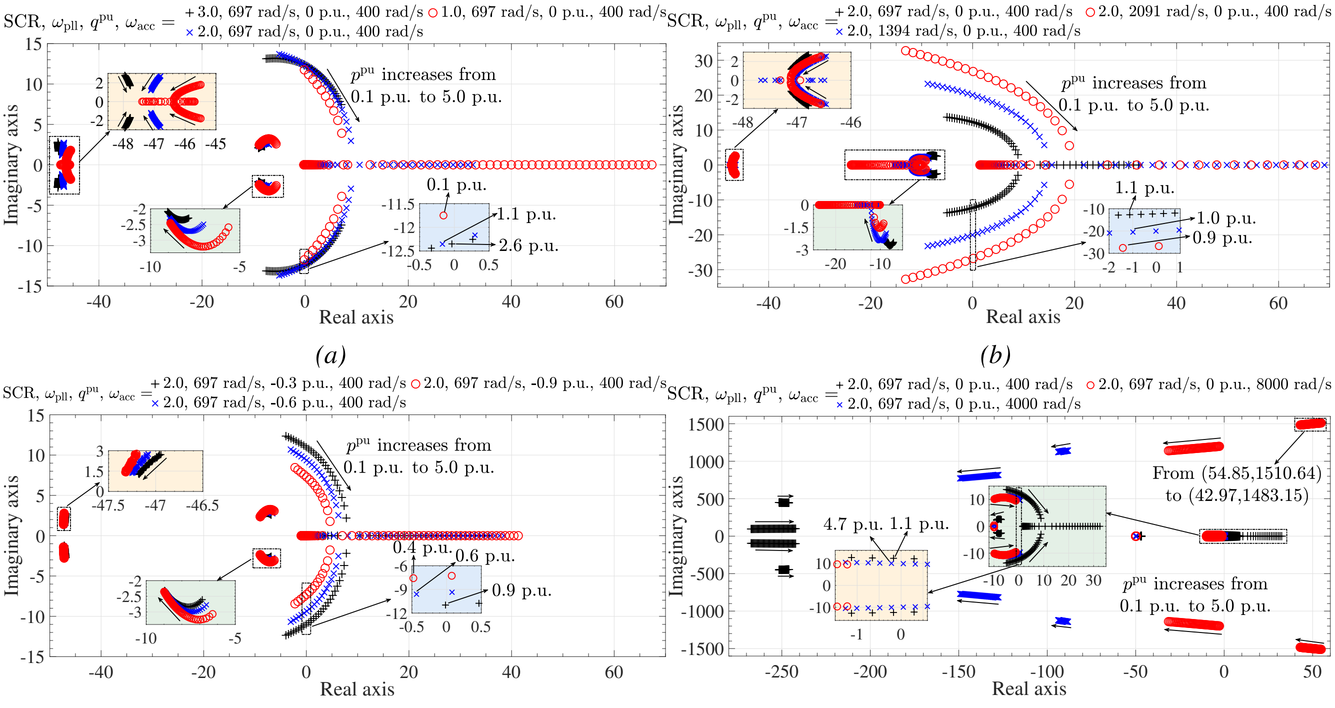

(a) *(b)*

(c) *(d)*

Figure 41: Eigenvalue loci of ACC-PLL-GFLI-Grid composite system as active power p^{pu} increases from 0.1 p.u. to 5.0 p.u. under different (a) SCR, (b) PLL bandwidth ω_{pll}, (c) reactive power q^{pu}, and (d) ACC bandwidth ω_{acc}.

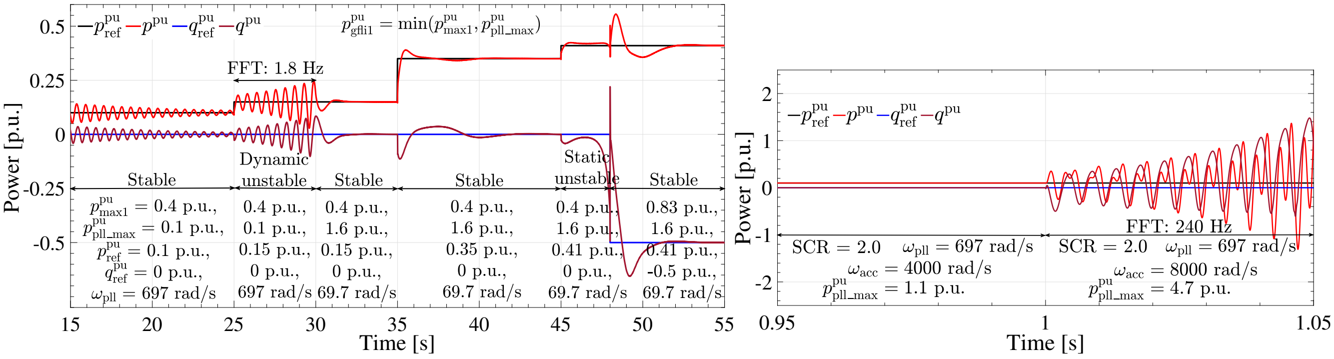

(a) *(b)*

Figure 42: Time-domain simulation verification of ACC-PLL-GFLI-Grid composite system suffering from (a) both power-angle-induced and PLL-induced MPTC issues and (b) ACC-induced high-frequency instability issue.

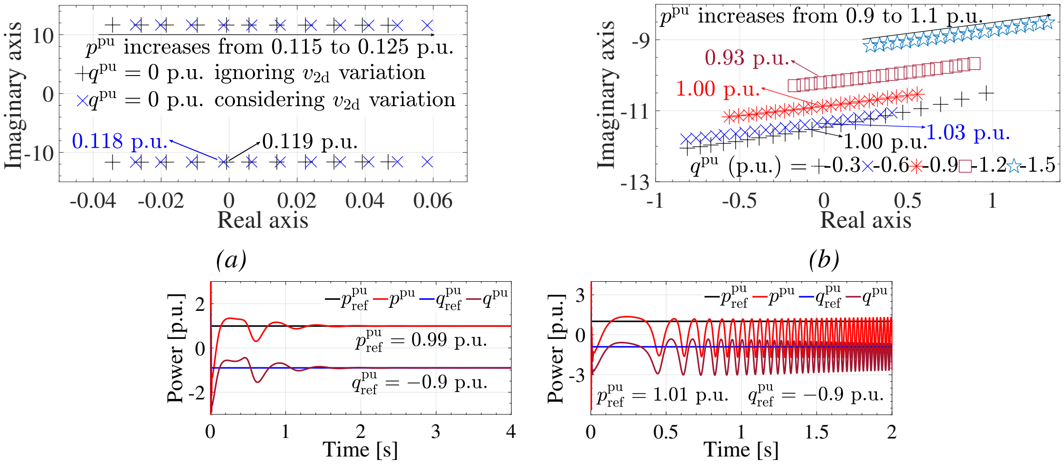

(a) *(b)*

(c)

Figure 43: Eigenvalue loci of ACC-PLL-GFLI-Grid composite system considering PCC voltage v_{2d} variation as (a) SCR = 1.0, $\omega_{pll} = 697$ rad/s, $q^{pu} = 0$ p.u., $\omega_{acc} = 400$ rad/s, and (b) SCR = 2.0, $\omega_{pll} = 697$ rad/s, q^{pu} = -0.3 to -1.5 p.u., $\omega_{acc} = 400$ rad/s. (c) Simulation verification as SCR = 2.0, $\omega_{pll} = 697$ rad/s, q^{pu} = -0.9 p.u., and $\omega_{acc} = 400$ rad/s.

increasing reactive power absorption increases p^{pu}_{max1} and decreases $p^{pu}_{pll\_max}$.

Fig. 44(a)-(d) show the experimental results of the grid current as the inner ACC bandwidth ω_{acc} is 355.2, 414.4, 473.6, and 532.8 rad/s, respectively. It can be seen that the MPTC under the four inner ACC bandwidths is 0.15, 0.3, 0.6, and 0.8 p.u., respectively, which indicates that the MPTC increases as the inner ACC bandwidth increases.

3.3.3 Small-Signal Stability Enhancement of GFLIs

Fig. 45(a) shows the single-line diagram of the PLL-based GFLI connected to a resistive-inductive grid. The high-frequency switching harmonics are filtered by the L-filter with inductance L_f and parasitic resistance R_f. The inner ACC is equipped with cross-decoupling capability and PCC voltage feed-forward path using coefficient γ_{acc}. The SRF-PLL is used to align the phase angle of the injected current with that of the PCC voltage. High-frequency measurement noises of the grid current and the PCC voltage are filtered by the low-pass filters (LPFs) with time constants T_i and T_v, respectively. Note that the superscripts s and c indicate that the variables are represented in the system and controller reference frames, respectively.

The complex-valued small-signal representation of Fig. 45(a) is shown in Fig. 45(b). In addition, the semiconductor switching device is modeled as a voltage gain $0.5V_{dc}$. To eliminate the adverse effects of PLL itself and the control interaction between the PLL and ACC on low-frequency passivity, an additional PCC voltage feed-forward controller as shown in Fig. 46(a) is employed. Its complex-valued model is derived in Fig. 46(b).

The implementation of the proposed full PLL passivation module in Fig. 46(a) is shown in Fig. 47(a). A compensation module that can eliminate the operating point shift is designed in Fig. 47(b), which only generates the steady-state values of $-\overrightarrow{v^{c\_part}_{m4dq}}$ and is thus not affected by small-signal perturbation.

Fig. 48(a) plots the eigenvalue loci of the GFLI-Grid composite system considering the PLL and full PLL passivation module when the grid current references $i^{ref}_{gd} = 1.0$ p.u., $i^{ref}_{gq} = 0$ p.u., the inner ACC

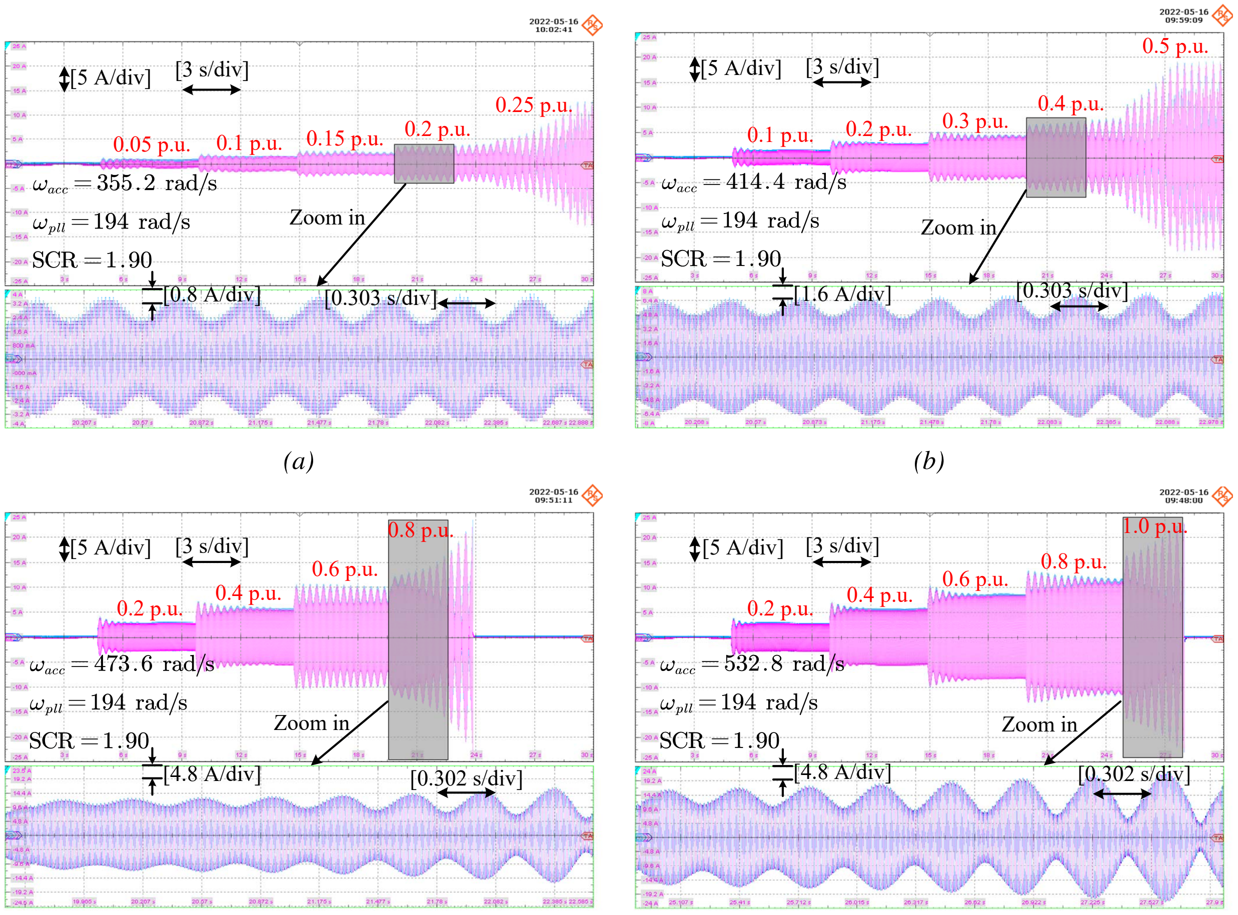

(a)

(b)

(c)

(d)

Figure 44: Experimental results of the grid current as inner ACC bandwidth ω_{acc} is (a) 355.2, (b) 414.4, (c) 473.6, and (d) 532.8 rad/s.

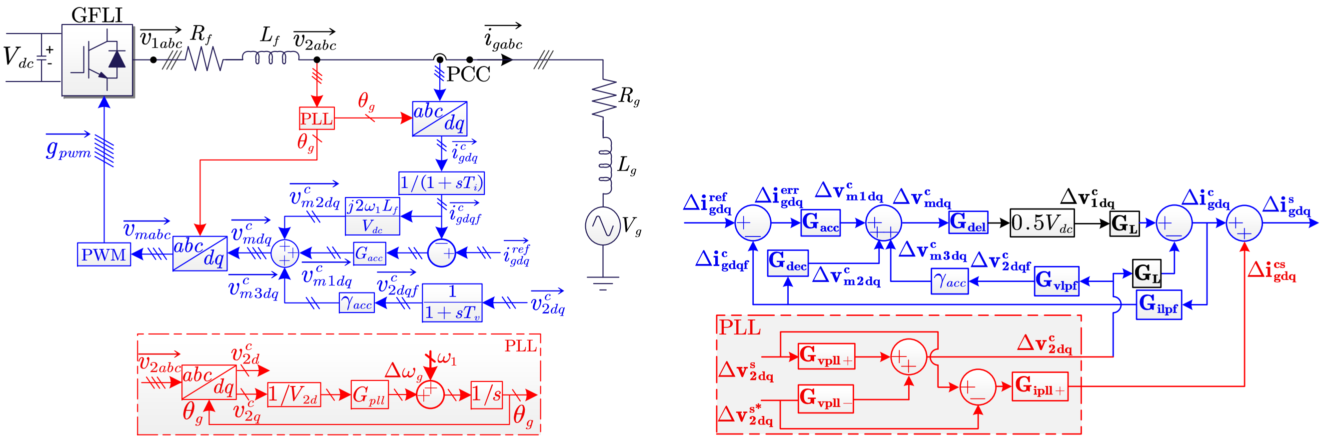

(a)

(b)

Figure 45: (a) Single-line control structure and (b) complex-valued block diagram of the GFLI connected to a resistive-inductive grid.

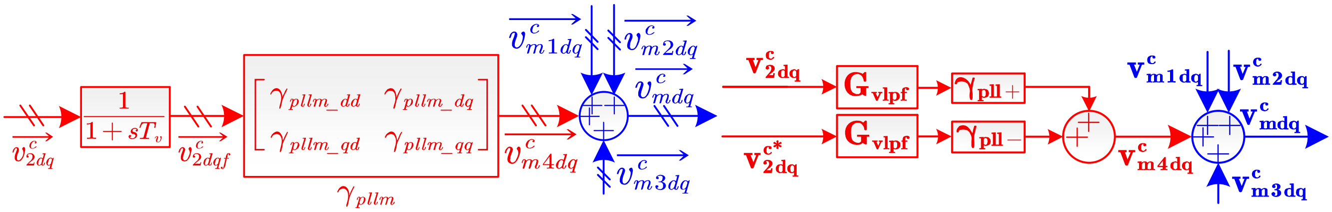

(a) (b)

Figure 46: (a) Single-line control structure and (b) complex-valued block diagram of the PLL passivation module.

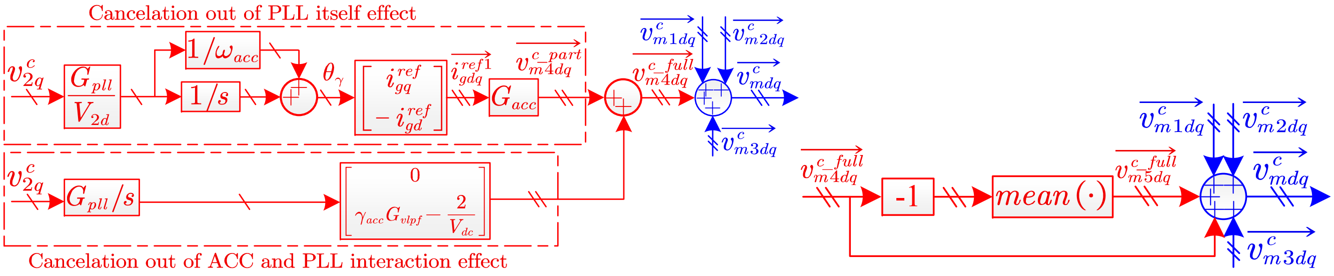

(a) (b)

Figure 47: Block diagrams of (a) full PLL passivation module without compensation of operating point shift and (b) full PLL passivation module equipped with compensation of operating point shift.

bandwidth $\omega_{acc} = 207.2$ rad/s, the PLL bandwidth $\omega_{pll} = 69$ rad/s, $\gamma_{acc} = \frac{0.1000}{575}$, and the SCR decreases from 5.0 to 3.0 with grid impedance angle $\phi = 80°$. It can be seen that, if the full PLL passivation module is employed, the eigenvalue pair $C_{1,2}$ can be kept almost unchanged in the left-half plane. Fig. 48(b) shows the time-domain simulation results without the PLL passivation module as the SCR decreases from 3.8 to 3.6 at 30 s, which indicates that a 1.8-Hz oscillation occurs after 30 s. In addition, Fig. 48(c) shows the time-domain simulation results with the PLL passivation module as the SCR decreases from 3.8 to 3.6 at 30 s and then further decreases to 3.0 at 40 s, which indicates the GFLI-Grid composite system is kept stable. These time-domain simulation results in Fig. 48(b) and (c) thus verify the correctness of the eigenvalue analysis in Fig. 48(a). In conclusion, the low-frequency stability of the GFLI equipped with the full PLL passivation module can be guaranteed under varying grid strength conditions.

Fig. 49(a) plots the eigenvalue loci of the GFLI-Grid composite system considering the PLL and full PLL passivation module when the grid current references $i^{ref}_{gd} = 1.0$ p.u., $i^{ref}_{gq} = 0$ p.u., the SCR = 3.0 with grid impedance angle $\phi = 80°$, $\gamma_{acc} = \frac{0.1000}{575}$, the inner ACC bandwidth $\omega_{acc} = 207.2$ rad/s, and the PLL bandwidth ω_{pll} increases from 6.9 to 207 rad/s. It can be seen that the eigenvalue pair $C_{1,2}$ without the full PLL passivation module moves into the right-half plane and excites a $\frac{6.35}{2\pi} = 1.01$-Hz oscillation if the PLL bandwidth ω_{pll} is increased to 27.88 rad/s, whereas the eigenvalue pair $C_{1,2}$ is kept in the left-half plane if the full PLL passivation module is employed. Fig. 49(b) shows the time-domain simulation results without the PLL passivation module as the PLL bandwidth ω_{pll} increases from 20.91 to 27.88 rad/s at 6 s, which indicates that a 1.0-Hz oscillation occurs after 6 s. In addition, Fig. 49(c) shows the time-domain simulation results with the PLL passivation module as the PLL bandwidth ω_{pll} increases from 20.91 to 27.88 rad/s at 6 s and then further increases to 207 rad/s at 10 s, which indicates the GFLI-grid composite system is kept stable. These time-domain simulation results in Fig. 49(b) and (c) thus verify the correctness of the eigenvalue analysis in Fig. 49(a). In conclusion, the low-frequency stability of the GFLI equipped with the full PLL passivation module can be guaranteed under varying PLL bandwidth conditions.

Fig. 50(a) plots the eigenvalue loci of the GFLI-Grid composite system considering the PLL and the full

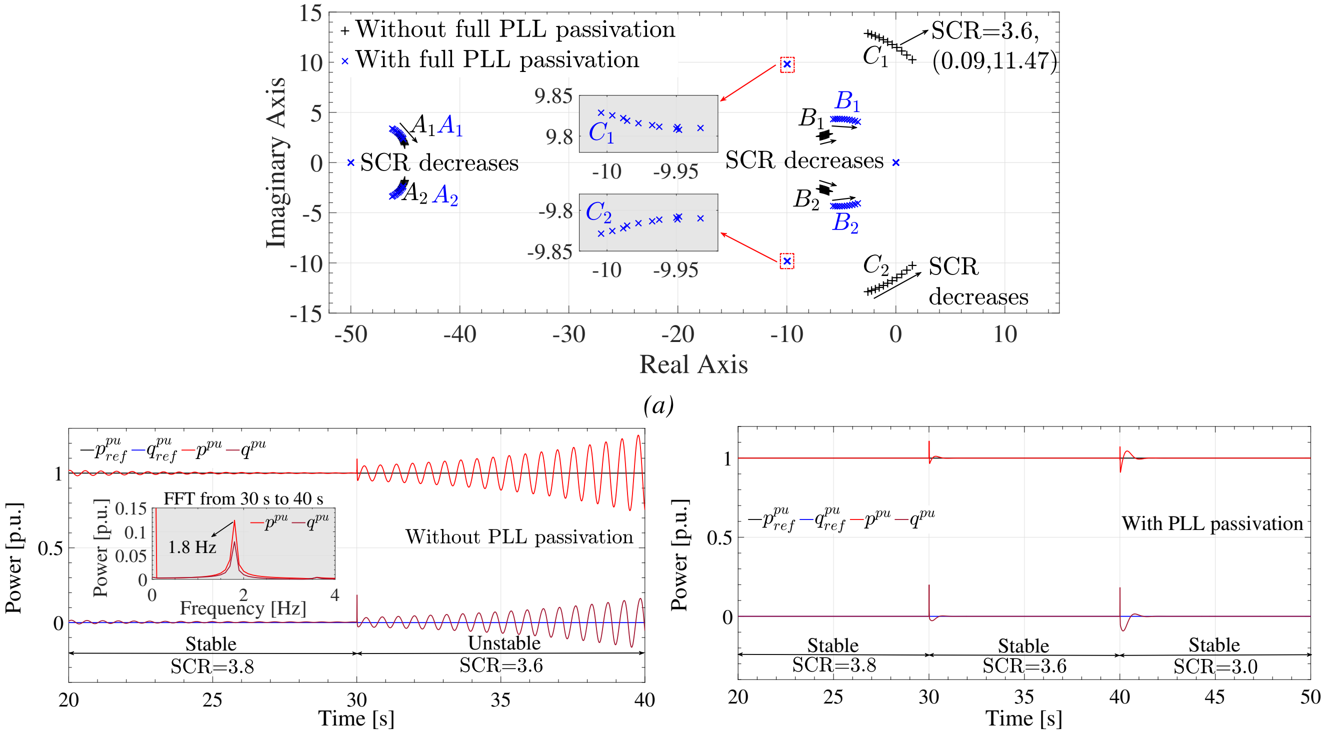

(a)

(b)

(c)

Figure 48: Stability analysis of the GFLI-Grid composite system considering PLL and full PLL passivation module as the SCR varies with grid impedance angle $\phi = 80°$. (a) Eigenvalue loci as the SCR decreases from 5.0 to 3.0. Time-domain simulation verification (b) without and (c) with the full PLL passivation module as the SCR changes.

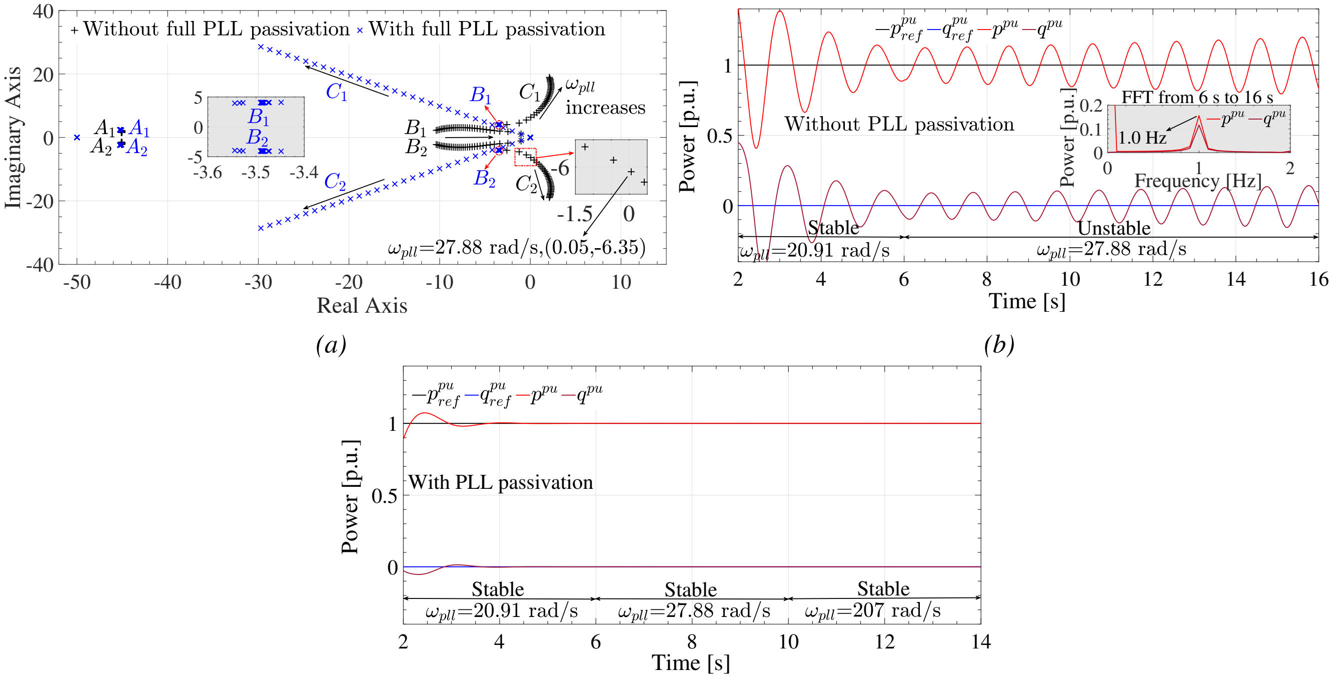

(a)

(b)

(c)

Figure 49: Stability analysis of the GFLI-Grid composite system considering PLL and full PLL passivation module as the PLL bandwidth ω_{pll} varies. (a) Eigenvalue loci. Time-domain simulation verification (b) without and (c) with the full PLL passivation module.

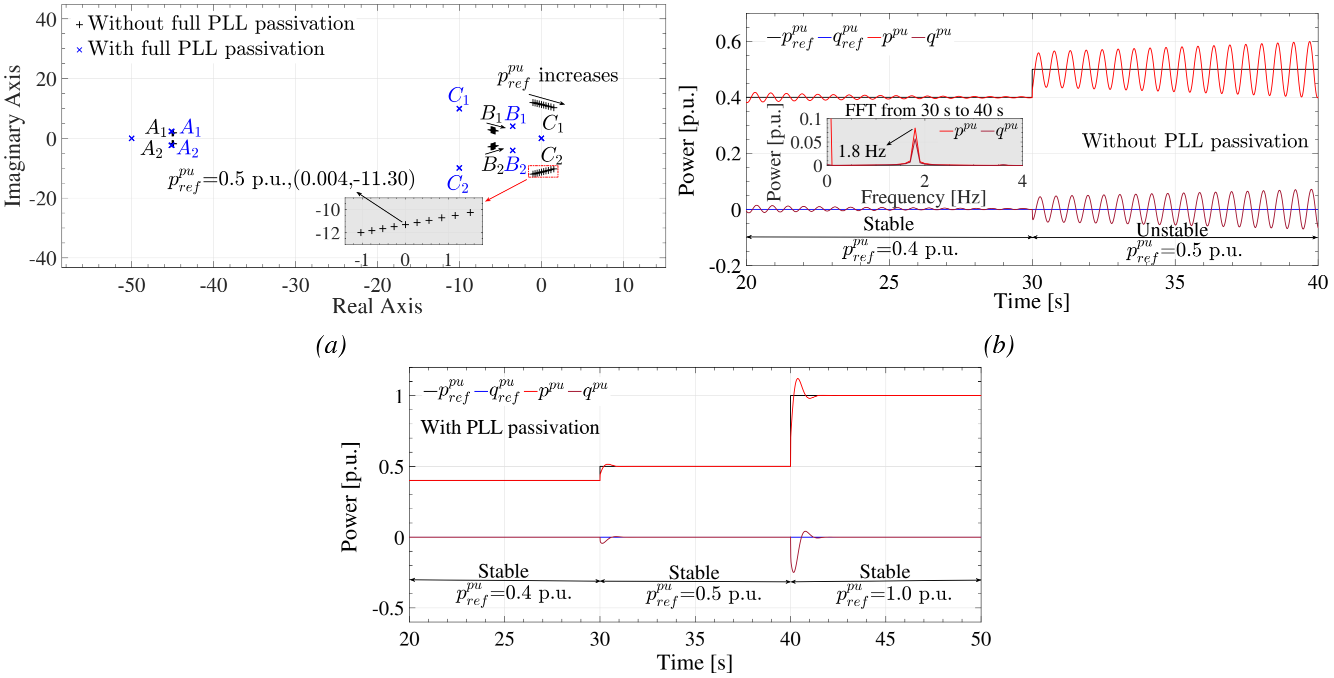

(a) *(b)*

(c)

Figure 50: Stability analysis of the GFLI-Grid composite system considering PLL and full PLL passivation module as the active power reference p_{ref}^{pu} increases. (a) Eigenvalue loci. Time-domain simulation verification (b) without and (c) with the full PLL passivation module.

PLL passivation module when the SCR = 3.0 with the grid impedance angle $\phi = 80°$, $\gamma_{acc} = \frac{0.1000}{575}$, the inner ACC bandwidth $\omega_{acc} = 207.2$ rad/s, the PLL bandwidth $\omega_{pll} = 69$ rad/s, the reactive current reference $i_{gq}^{ref} = 0$ p.u., and the active current reference i_{gd}^{ref} increases from 0.1 to 1.0 p.u.. It can be seen that the eigenvalue pair $C_{1,2}$ without the full PLL passivation module moves into the right-half plane and excites a $\frac{11.30}{2\pi} = 1.8$-Hz oscillation if the active current reference i_{gd}^{ref} is increased to 0.5 p.u., whereas the eigenvalue pair $C_{1,2}$ is kept almost unchanged in the left-half plane if the full PLL passivation module is employed. Fig. 50(b) shows the time-domain simulation results without the PLL passivation module as the active power reference p_{ref}^{pu} increases from 0.4 to 0.5 p.u. at 30 s, which indicates that a 1.8-Hz oscillation occurs after 30 s. In addition, Fig. 50(c) shows the time-domain simulation results with the PLL passivation module as the active power reference p_{ref}^{pu} increases from 0.4 to 0.5 p.u. at 30 s and then further increases to 1.0 p.u. at 40 s, which indicates the GFLI-Grid composite system is kept stable. These time-domain simulation results in Fig. 50(b) and (c) thus verify the correctness of the eigenvalue analysis in Fig. 50(a). In conclusion, the low-frequency stability of the GFLI equipped with the full PLL passivation module can be guaranteed under varying active power transfer conditions.

4 Power-Synchronised Grid-Following Inverters

As discussed in previous sections, one of the major causes of instability in GFLIs is the PLL. Therefore, new PLL-less control strategies are promising as they can improve inverters stability, especially in weak grid conditions. In this project, an innovative control strategy called PSGFLI is proposed. Contrary to conventional GFLI which has difficulties in weak grids, the PSGFLI is a PLL-less control technology that enables the seamless operation of GFLIs in both weak and strong grids; hence, it permits full control of the active and reactive power without being prone to instability.

4.1 Generic Control Structure of the PSGFLI Under Balanced Grid

Fig. 51 shows the generic control structure of the proposed PSGFLI under balanced grid. It can be noticed that the control structure does not employ a PLL [40]. In the PSGFLI, the SRF is aligned with the inverter output current instead of the voltage, as in the conventional GFLI.The 2-by-2 outer power control loop generates the estimated grid frequency (ω) and the d-component of the current reference ($i_{\mathrm{d,ref}}$). The calculated real and reactive powers are filtered out by a second-order low-pass filter (H).

During this project, three different strategies are developed to tune the 2-by-2 parameters (M_{11} to M_{22}) of the outer power controllers of the PSGFLI in balanced grid conditions. Furthermore, a double-synchronous-reference-frame-based strategy is proposed for faults/unbalanced grid voltage events. The four strategies are explained next.

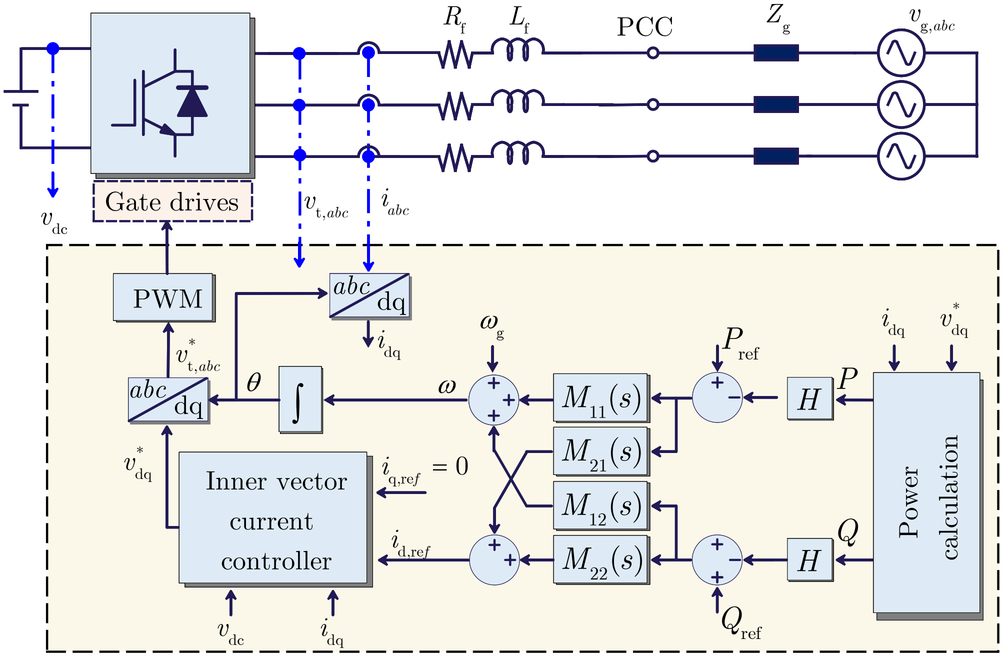

Figure 51: The generic control structure of the PLL-less PSGFLI.

4.2 PSGFLIs Under Balanced Grid

This section elaborates on three different control strategies that are developed in this project for tuning the 2-by-2 parameters of the outer power controllers of the proposed PSGFLIs when it operates in balanced grid conditions. In these three different strategies, the PSGFLI regulates the active and reactive power at the inverter terminal instead of PoC. The voltage references provided to PWM can also be used to eliminate the negative impact of the distorted measured voltage in weak grids.

4.2.1 Optimized-based Control of PSGFLIs

The detailed block diagram of the proposed control strategy for PSGFLI is shown previously in Fig. 51. The rotating reference frame aligned with the inverter current, i.e., i_q=0 A [40]. Hence, the inverter current, $I_\mathrm{d}\angle 0°$, and its terminal voltage, $V_\mathrm{t}\angle\delta$, are expressed in this dq frame as

$$i_\mathrm{dq} = I_\mathrm{d} + j0 \text{ and } v_\mathrm{t,dq} = V_\mathrm{t}\cos\delta + jV_\mathrm{t}\sin\delta. \tag{62}$$

Additionally, in every dq-frame, the inverter power is

$$P + jQ = \frac{3}{2}(v_\mathrm{t,d}i_\mathrm{d} + v_\mathrm{t,q}i_\mathrm{q} + j(v_\mathrm{t,q}i_\mathrm{d} - v_\mathrm{t,d}i_\mathrm{q})). \tag{63}$$

Replacing for i_dq and $v_\mathrm{t,dq}$ form (62) in (63), one can write

$$P + jQ = \frac{3}{2}(V_\mathrm{t}I_\mathrm{d}\cos\delta + jV_\mathrm{t}I_\mathrm{d}\sin\delta). \tag{64}$$

Eq. (64) shows that as the SRF is aligned with the inverter current; thus, the real power is proportional to the d-component of the inverter terminal voltage, while the reactive power is proportional to its q-component.

In the PSGFLI, $i_\mathrm{d,ref}$ and ω are generated from the 2-by-2 outer power control loop, as shown below

$$\begin{bmatrix} \omega \\ I_\mathrm{d,ref} \end{bmatrix} = \underbrace{\begin{bmatrix} K_\mathrm{PI,1} & K_\mathrm{PI,3} \\ K_\mathrm{PI,2} & K_\mathrm{PI,4} \end{bmatrix}}_{\mathbf{K}} \begin{bmatrix} e_P \\ e_Q \end{bmatrix}, \tag{65}$$

where $K_\mathrm{PI,1}$, $K_\mathrm{PI,2}$, $K_\mathrm{PI,3}$, and $K_\mathrm{PI,4}$ are the four PI controllers whose coefficients are tuned using a loop-shaping-based strategy. Here, an optimization-based tuning approach is followed, in which the square-second norm of the error between the individual entries of actual and desired open-loop transfer function matrices is minimized. Consequently, the parameters of $K_\mathrm{PI,1}$, $K_\mathrm{PI,2}$, $K_\mathrm{PI,3}$ and $K_\mathrm{PI,4}$ are obtained.

Stability Analysis:
The robustness of the proposed optimization-based PSGFLI is tested based on the closed-loop frequency responses of the system for 50 operating points, as shown in Fig. 52. It can be observed that the frequency responses of the off-diagonal elements are below 0 db. Furthermore, for larger $I_\mathrm{d,0}$, the diagonal elements of the closed-loop system have a bandwidth of around 100 $\frac{\mathrm{rad}}{s}$, which is in agreement with the desired bandwidth of the open-loop transfer function.'

Performance Validation:
To validate the performance of the proposed optimization-based PSGFLI, a scaled-down setup of the system is implemented in the laboratory as shown in Fig. 53. The tested conditions include the grid voltage amplitude drops, the grid voltage becomes unbalanced, and the grid voltage phase angle jump for 15°. Furthermore, the operation of the optimization-based PSGFLI has tested in also a strong grid with an SCR of 6.4 and in a weak grid with an SCR of 0.9, as shown in Fig. 54 and Fig. 55, respectively. The inverter initially operates in the steady-state and injects P=1200 W and Q=900 Var to the grid. Then, the grid-related scenarios in which the voltage sag, voltage imbalance, and voltage phase jump are applied at 0.1, 0.3 and 0.5 s, respectively. Obtained results in Fig. 54 and Fig. 55 from the tested conditions in both strong and weak operations confirm the robustness of the proposed optimization-based PSGFLI.

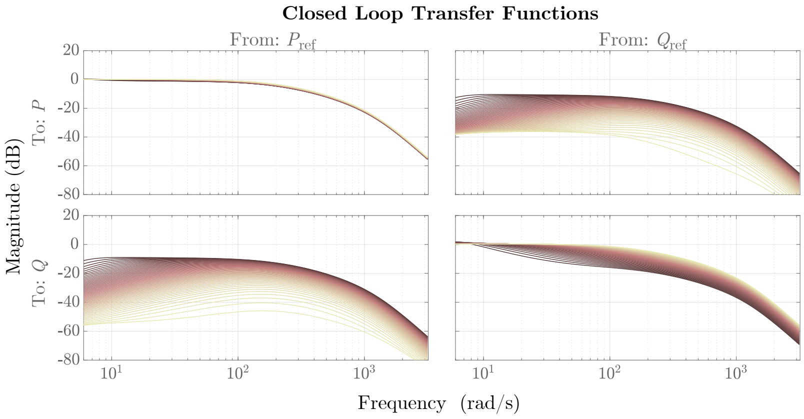

Figure 52: The frequency response of the closed-loop system of the optimization-based PSGFLI for 50 parametric models with various operating points where δ_0=0.4 rad & $I_{\mathrm{d,0}}$∈[100 3000] A. Lighter shades correspond to larger currents.

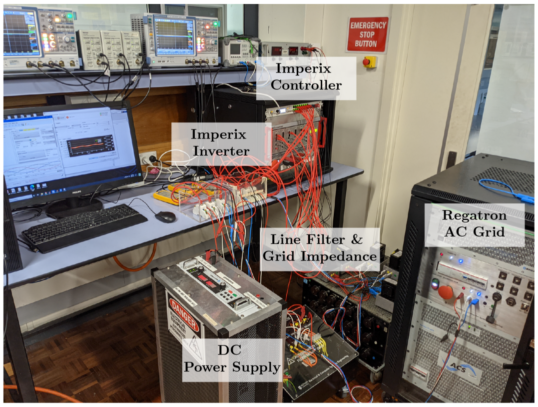

Figure 53: The experimental setup used to verify the performance of the optimization-based PSGFLI.

4.2.2 Linear Parameter-Varying-based Control of PSGFLIs

This section elaborates on the proposed a Linear Parameter-Varying Controlled Power-Synchronised Grid-Following Inverter (LPV-PSGFLI). In this approach, the controller parameters shown in (65) are functions of the operating point and are adaptively tuned in real-time such that the closed-loop performance is preserved in all operating points. Furthermore, since the grid impedance is a factor in the design process, a robustness analysis against grid impedance estimation error is conducted, and it is shown that discrepancies in the estimated and real grid impedances are unlikely to make the system unstable. The performance of the proposed control design is validated in experiments for both strong and weak grids. The main benefits of the proposed LPV-PSGFLI are

- constant bandwidth for different operating points,
- straightforward control design based on the IBR operating point, and
- inversion and rectification capabilities.

As seen in the previous subsection, the system under study is a multi-input multi-output system; hence, a 2×2 controller must be designed to guarantee stability. To do so, in this study, an LPV-PSGFLI is proposed such that it addresses the drawbacks of the controller designed based on optimization methods. To design the LPV-PSGFLI, a vector of scheduling parameters should be chosen, which is selected as μ=$[I_{\mathrm{d,0}}, \delta_0]^T$.

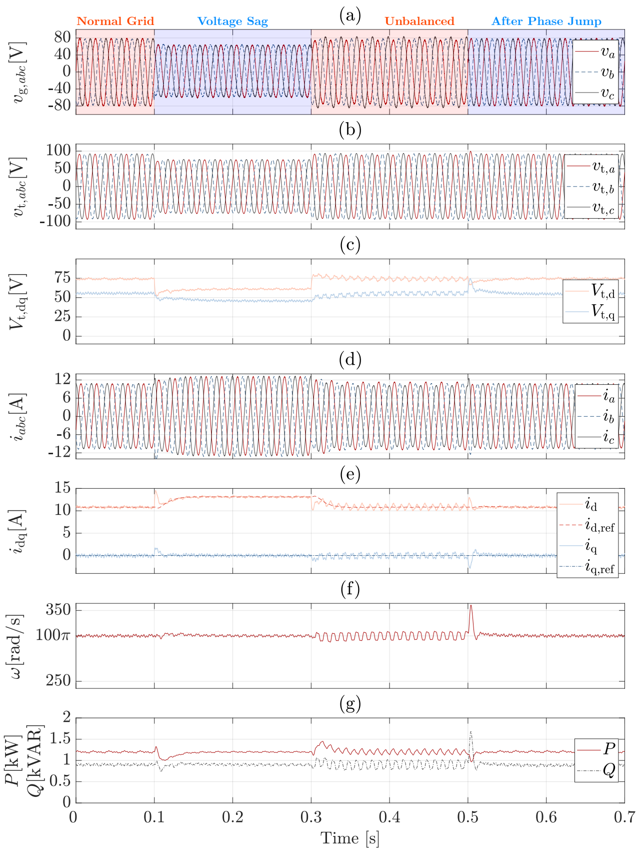

(a)

Figure 54: The experimental results of the optimization-based PSGFLI operating in a strong grid (SCR= 6.4): (a) the grid voltage, (b) the inverter terminal voltage reference, (c) the dq-components of the inverter terminal voltage reference, (d) the inverter current and their references, (e) the dq-components of the inverter current and their references, (f) the system frequency extracted by the controller, and (g) the inverter's real/reactive power.

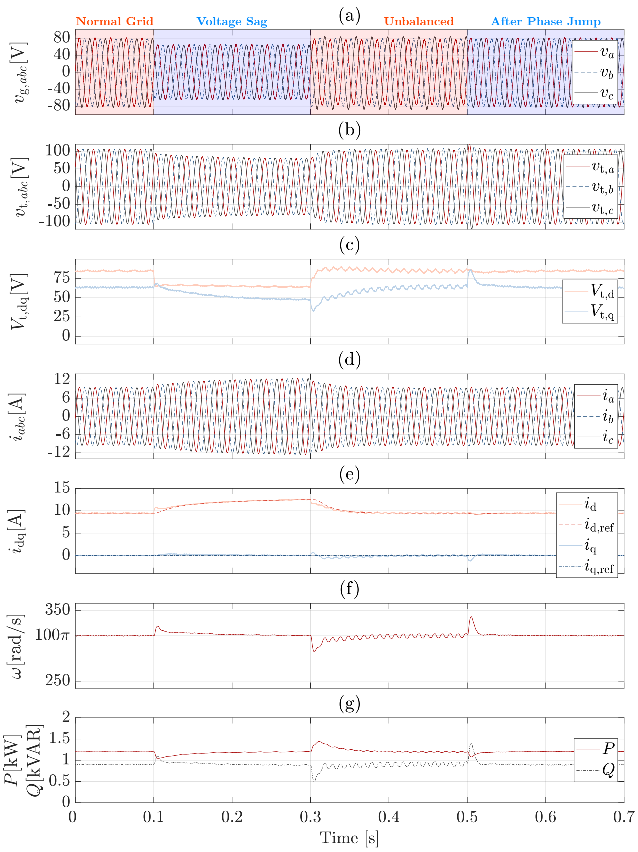

(a)

Figure 55: The experimental results of the optimization-based PSGFLI operating in a weak grid (SCR= 0.9): (a) the grid voltage, (b) the inverter terminal voltage reference, (c) the dq-components of the inverter terminal voltage reference, (d) the inverter current and their references, (e) the dq-components of the inverter current and their references, (f) the system frequency extracted by the controller, and (g) the inverter's real/reactive power.

Hence, the designed controller and the system both are functions of the vector μ.

Supposing that the desired open-loop transfer function matrix of the system, $\mathbf{L_D}$, is chosen as

$$\mathbf{L_D} = \begin{pmatrix} k_p/s & 0 \\ 0 & k_p/s \end{pmatrix}, \tag{66}$$

and assuming that $\mathbf{K}(\mu)$ is the designed 2×2 controller, the open-loop transfer function can be written as

$$\mathbf{L}(\mu) = \mathbf{G}(\mu) \times \mathbf{K}(\mu). \tag{67}$$

In case the open-loop transfer function is equal to the desired transfer function introduced in (66),

$$\mathbf{K}(\mu) = \mathbf{G}^{-1}(\mu) \times \mathbf{L_D}. \tag{68}$$

Note that the chosen $\mathbf{L_D}$ guarantees stability since the closed-loop transfer functions on the diagonal entries become $\frac{K_p}{s+K_p}$, which is a stable transfer function. Additionally, $\mathbf{L_D}$ provides a decoupled system as its off-diagonal elements are zero. To find the controller matrix, $\mathbf{K}(\mu)$, the inverse of $\mathbf{G}(\mu)$ can be derived as

$$\mathbf{G}^{-1}(\mu) = \begin{pmatrix} \frac{2s\sin\delta_0}{3V_t I_{\mathrm{d,0}}} & -\frac{2s\cos\delta_0}{3V_t I_{\mathrm{d,0}}} \\ \frac{2(\tau s+1)\cos\delta_0}{3V_t} & \frac{2(\tau s+1)\sin\delta_0}{3V_t} \end{pmatrix}. \tag{69}$$

By replacing (69) in (68), the controller matrix becomes

$$\mathbf{K}(\mu) = \begin{pmatrix} k_p\frac{2\sin\delta_0}{3V_t I_{\mathrm{d,0}}} & -k_p\frac{2\cos\delta_0}{3V_t I_{\mathrm{d,0}}} \\ k_p\frac{2(\tau s+1)\cos\delta_0}{3V_t s} & k_p\frac{2(\tau s+1)\sin\delta_0}{3V_t s} \end{pmatrix}. \tag{70}$$

Keeping in mind that i_{q}=0 A, the apparent power can be written as

$$S_{\mathrm{t}} = \frac{3}{2}V_t I_{\mathrm{d}}. \tag{71}$$

By replacing (71) in (70), the designed controller can be reformulated as

$$\mathbf{K}(\mu) = \begin{pmatrix} k_p\frac{\sin\delta_0}{S_{\mathrm{t}}} & -k_p\frac{\cos\delta_0}{S_{\mathrm{t}}} \\ k_p\frac{(\tau s+1)I_{\mathrm{d,0}}\cos\delta_0}{s\times S_{\mathrm{t}}} & k_p\frac{(\tau s+1)I_{\mathrm{d,0}}\sin\delta_0}{s\times S_{\mathrm{t}}} \end{pmatrix}, \tag{72}$$

in which S_{t} is the inverter output apparent power and can be written as $S_{\mathrm{t}}=\sqrt{P^2+Q^2}$, $\delta_0=\tan^{-1}\frac{Q}{P}$, and $I_{\mathrm{d,0}}$ is the inverter output current peak value, which can be updated in the controller shown in (72) via real-time measurements. It is worth mentioning that by choosing the desired open-loop transfer function as shown in (66), the closed-loop transfer function becomes

$$\mathbf{G_{cl}} = \begin{pmatrix} \frac{k_p}{s+k_p} & 0 \\ 0 & \frac{k_p}{s+k_p} \end{pmatrix} = \begin{pmatrix} \frac{1}{Ts+1} & 0 \\ 0 & \frac{1}{Ts+1} \end{pmatrix}, \tag{73}$$

in which $T=\frac{1}{k_p}$ is the system time constant. Hence, the bandwidth of the system dynamic response can be directly adjusted by setting k_p.

The main advantage of the controller proposed in (72) is that it is easy to design and does not require system identification and/or solving an optimization-based loop-shaping problem since it provides a parametric loop-shaping controller. In addition, (72) schedules its gains based on the system operating point. Hence, the system bandwidth is not changed by changing the IBR operating point. Finally, this controller allows the system to perform bidirectionally, i.e., in inverter and rectifier modes. The reason is that regardless of the power direction, the system open-loop transfer function is $\mathbf{L_D}$ using the proposed LPV-PSGFLI, which is a stable system.

Stability Analysis:

For optimal tuning of the PI controller employed in the current controller, the grid resistance and inductance are assumed to be known. Although there are many approaches for accurate impedance estimation in the literature, errors in the grid impedance estimation can occur in the system. In a general case, when the inductance and resistance estimations have random and not necessarily equal errors, the pole and zero of the characteristic equation of the system are moved. Thus, a robustness analysis against impedance estimation errors is needed.

Fig. 56 shows the closed-loop system poles are the characteristic equation roots as a function to grid impedance estimation errors. In this analysis, it is assumed that the resistance estimation error is 10%,

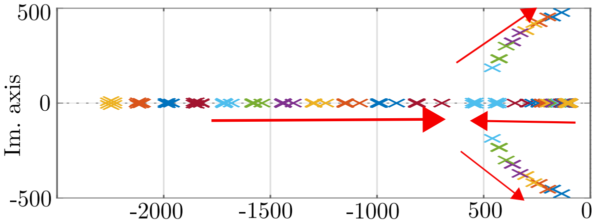

Figure 56: The characteristic equation roots when the resistance estimation error is 10% and the inductance estimation error varies from 5% to 95%.

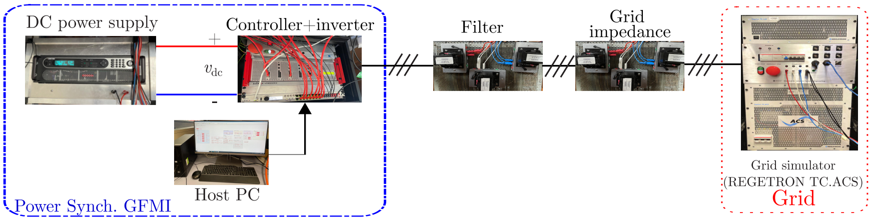

Figure 57: The experimental setup.

Quantity	Value	Comment
L_f	14 mH	Inverter Filter Inductance
R_f	0.5 Ω	Series Resistance of L_f
S_{base}	1 kVA	Inverter Rated Power
v_g	100 V	Grid Line-to-Line Voltage (rms)
v_{dc}	300 V	DC Bus Voltage
f_{sw}	20 kHz	PWM Carrier Frequency
f	50 Hz	System Nominal Frequency
f_{filt}	200 Hz	Power Measurement LPF Bandwidth

Table 7: The parameters of the experimental setup.

and the inductance estimation error varies from 5% to 95% with 5% steps. The arrows shown in Fig. 56 show the estimation error increase. It is seen that the overall closed-loop system remains stable despite the different estimation errors resistance and inductance have. It should be noted that the presence of errors in the inductance and resistance estimations adds more poles and zeros to the closed-loop transfer function, and hence, some new dynamics will be added to the system; nonetheless, it is not likely that these estimation errors threat the system stability.

Performance Validation:

To assess the performance of the proposed LPV-PSGFLI, an experimental setup based on the Imperix B-Box Controller and Regatron AC Power Supply is used. The experimental platform is shown in Fig. 57 and the system parameters are listed in Table 7. In these tests, the performance of the controller for active power, reactive power, and power factor changes is evaluated.

1. *Strong Grid (SCR=31) Test:* In the first test, the grid inductance and resistance are set to 1 mH and 0.03 Ω, respectively, making the SCR=31. Initially, the inverter injects no active or reactive power into the grid. At t=0.1 s, the reactive power reference is changed to 800 VAR. At t=0.35 s, the active power set-point is changed to 600 W. Finally, at t=0.6 s, the power factor is changed from 0.6 to 0.8, while the apparent power is kept at 1 pu. Fig. 58 shows the experimental results of this test. Fig. 58(a) is the three-phase injected currents, Fig. 58(b) is the three-phase grid line-to-neutral voltages, Fig. 58(c) shows the active and reactive power, Fig. 58(d) depicts the d and q-components of the injected current, as well as the generated i_d reference value by the controller, Fig. 58(e) depicts the d and q-components of the terminal voltage, and finally, Fig. 58(f) shows the angular frequency

estimated by the controller. It is seen that the system time constant is about 40 ms, and the controller regulates P and Q upon changes in their references.

2. *Weak Grid (SCR=*1.9*) Test:* In the second test, the grid inductance and resistance are set to 16 mH and 0.53 Ω, respectively, making the SCR=1.9. Initially, the inverter injects no active or reactive power into the grid. At t=0.1 s, the reactive power reference is changed to 800 VAR. At t=0.35 s, the active power set-point is changed to 600 W. Finally, at t=0.6 s, the power factor is changed from 0.6 to 0.8, while the apparent power is kept at 1 pu. Fig. 59 shows the experimental results of this test. Fig. 59(a) is the three-phase injected currents, Fig. 59(b) is the three-phase grid line-to-neutral voltages, Fig. 59(c) shows the active and reactive power, Fig. 59(d) depicts the d and q-components of the injected current, as well as the generated i_d reference value by the controller, Fig. 58(e) depicts the d and q-components of the terminal voltage, and finally, Fig. 59(f) shows the angular frequency estimated by the controller. It is seen that the system time constant is about 40 ms, and the controller regulates the P and Q upon changes in their references.

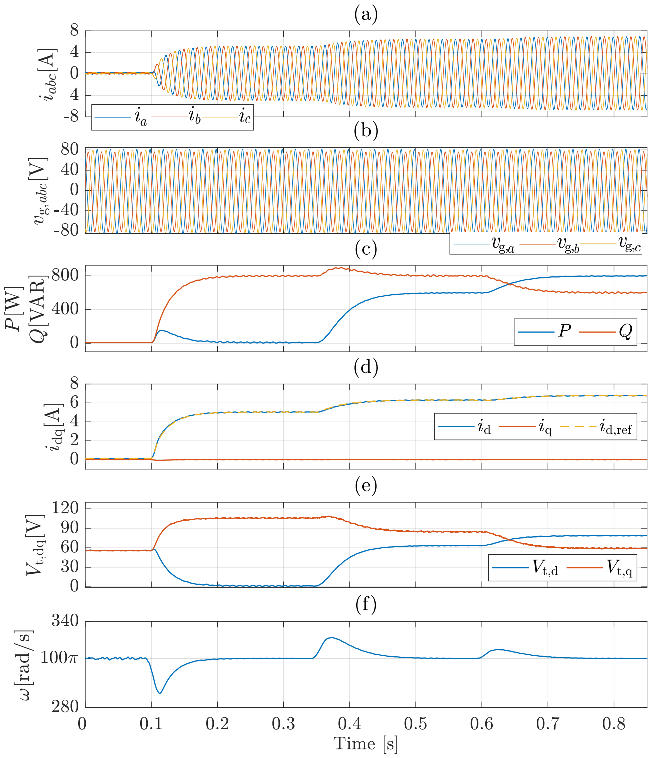

(a)

*Figure 58: The experimental results of the LPV-PSGFLI while connected to a strong grid with an SCR=*31 *upon active and reactive reference changes: a) the three-phase grid currents (i_{abc}), b) the grid three-phase line-to-neutral voltage, c) the injected active and reactive power into the grid, d) the dq-components of the grid current (i_{dq}) and $i_{d,ref}$, e) the dq-components of the terminal voltage ($v_{t,dq}$), and f) the estimated angular frequency generated by the controller.*

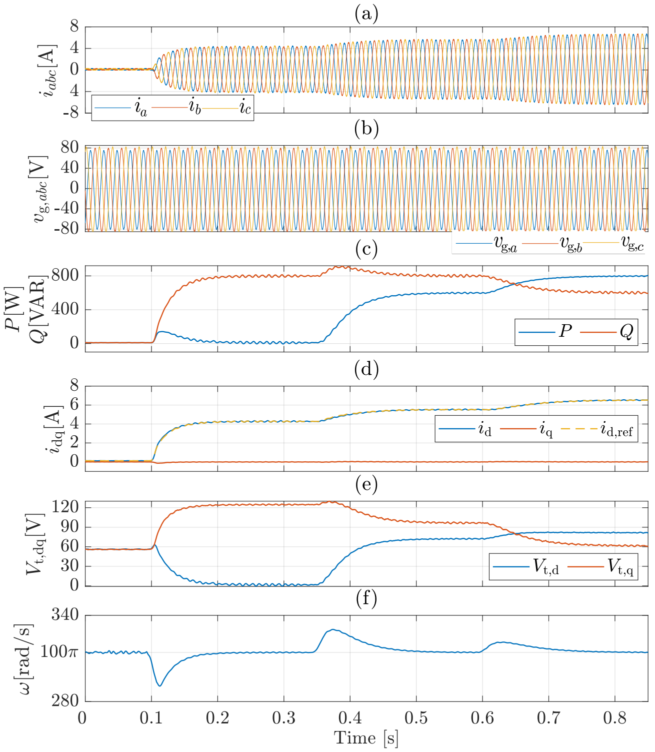

(a)

Figure 59: The experimental results of the LPV-PSGFLI while connected to a weak grid with an SCR= 1.9 *upon active and reactive reference changes: a) the three-phase grid currents (i_{abc}), b) the grid three-phase line-to-neutral voltage, c) the injected active and reactive power into the grid, d) the dq-components of the grid current (i_{dq}) and $i_{d,ref}$, e) the dq-components of the terminal voltage ($v_{t,dq}$), and f) the estimated angular frequency generated by the controller.*

4.2.3 Enhanced Frequency Control of PSGFLIs

The existing optimization-based PSGFLI and LPV-PSGFLI strategies suffer from several problems. On the one hand, the optimization-based PSGFLI is not straightforward as it involves an optimization-based design methodology to tune the four PI controllers. Hence, the bandwidth of the controller cannot be fixed during the variations of the inverter operating points. On the other hand, the LPV-PSGFLI strategy is very sensitive to grid frequency deviation from the nominal value which causes steady-state errors in the inverter output active and reactive power and also can drive the inverter to unstable operation.

To address the shortcomings of the optimized-based PSGFLI and LPV-PSGFLI, an Enhanced Power-Synchronised Grid-Following Inverter (ePSGFLI) is developed. There main two objectives of the ePSGFLI strategy are i) to cope with grid frequency deviations without causing any steady-state errors in the inverter output power or being driven to unstable operation, and ii) to adaptively tune the outer power controllers in real-time based on the operating point of the inverter in order to fix the bandwidth of the power control loop at the desired value regardless of the power reference commands and the grid conditions (e.g., strong and weak grids).

The proposed 2- by-2 second-order outer power controller of the proposed ePSGFLI is designed using the loop-shaping method in order to provide the desired dynamic performance and to ensure the system is fully decoupled. The parameters of the proposed 2-by-2 controller are shown below

$$M(s) = \begin{bmatrix} \underbrace{\frac{2\omega_c(s+\alpha)\sin\theta_0}{3I_{\mathrm{d},0}V_{\mathrm{t},0}s}}_{M_{11}(s)} & \underbrace{\frac{-2\omega_c(s+\alpha)\cos\theta_0}{3I_{\mathrm{d},0}V_{\mathrm{t},0}s}}_{M_{12}(s)} \\ \underbrace{\frac{2\omega_c(s+\alpha)(\tau s+1)(\cos\theta_0 + \frac{a_1}{V_{\mathrm{t},0}}\sin\theta_0)}{3V_{\mathrm{t},0}s^2(1+\frac{I_{\mathrm{d},0}}{V_{\mathrm{t},0}}a_2)}}_{M_{21}(s)} & \underbrace{\frac{2\omega_c(s+\alpha)(\tau s+1)(\sin\theta_0 - \frac{a_1}{V_{\mathrm{t},0}}\cos\theta_0)}{3V_{\mathrm{t},0}s^2(1+\frac{I_{\mathrm{d},0}}{V_{\mathrm{t},0}}a_2)}}_{M_{22}(s)} \end{bmatrix}, \qquad (74)$$

where ω_c and α are the desired bandwidth and gain of the proposed Power controller. θ is the angle between the inverter terminal voltage and the inverter current, I_d is the d-component of the inverter output current, and V_t is the magnitude of the inverter output phase-to-neutral voltage. 0 indicates the steady-state operation. It can be seen that the proposed 2- by-2 outer power controller deploys two PI controllers for $M_{11}(s)$ and $M_{12}(s)$, and two second-order transfer functions for $M_{21}(s)$ and $M_{22}(s)$.

Stability Analysis:

The robustness of the proposed ePSGFLI is evaluated in different grid conditions using the impedance stability analysis based on the Generalized Nyquist Criterion (GNC) in the SRF. Furthermore, the obtained results are compared for the same grid condition with the conventional GFLI equipped with an outer open-loop power control. The tested grid conditions of the two control systems are $Z_{\mathrm{g}1}$, $Z_{\mathrm{g}2}$ and $Z_{\mathrm{g}3}$ which correspond to three different grid conditions, namely a strong grid with an SCR= 10, a weak grid with an SCR= 2, and a very weak grid with an SCR= 1.2, respectively. In all cases, the inverter power references are set to $P_\mathrm{ref} = 4$ MW and $Q_\mathrm{ref} = 0$ VAR.

Fig. 60(a) and (c) present the bode plot of the proposed ePSGFLI and the conventional GFLI in the q-reference frame, respectively. On the one hand, it can be noticed that the proposed ePSGFLI has larger phase margins in the three cases. Hence, it is expected to operate robustly in weak and very weak grids. On the other hand, the phase margins of the conventional GFLI are significantly reduced in weak and very weak grids.

Fig. 60(b) and (d) presents the impedance-based stability analysis based on the GNC in the q-reference frame for the proposed ePSGFLI and the conventional GFLIs, respectively. While the two controllers are stable in the q-axis in strong grid conditions (shown in green color), the conventional GFLI is marginally stable in the weak grid when SCR =2, and it is unstable when the SCR is decreased further to 1.2. However, the proposed ePSGFLI is stable in the strong grid as well as in the weak and very weak grids.

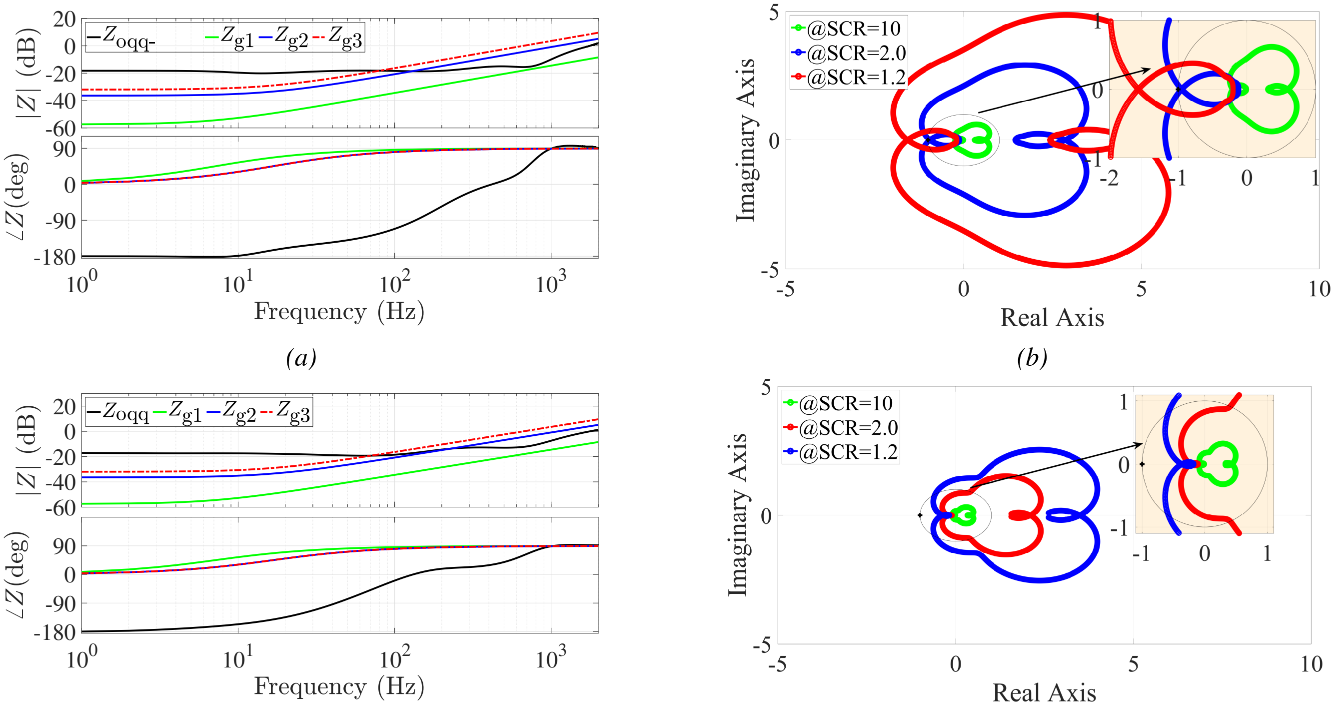

(a) *(b)*

(c) *(d)*

Figure 60: Frequency domain performance evaluation for the conventional PLL-based conventional GFLI (a) and (b) and the proposed PLL-Less ePSGFLI (c) and (d) operating in three grid conditions: (a) and (c) the grid impedances and the inverter output impedances in the q-axis; (c) and (d) stability assessment at the q-axis based on the GNC.

Performance Validation:

The performance of the ePSGFLI is further validated experimentally based on a scaled-down setup shown in Fig. 61. Two tests are conducted to examine the performance of the proposed ePSGFLI strategy in a strong grid with an SCR= 7.4 and in a weak grid with an SCR= 1.38. Additionally, a third case study is conducted to show the shortcoming of the LPV-PSGFLI method during grid frequency deviations in the weak grid with the SCR= 1.38. In all test cases, the inverter is rated at 1 kW and connected to the grid ($100V_{\text{L-L, RMS}}$). During these tests, step changes in the active and reactive power references are applied at t_1= 2 s and t_2= 4 s, respectively. Finally, a step change in the grid frequency is applied at t_3. For the first and second tests, a 5 Hz step change is applied to test the robustness of the proposed ePSGFLI to frequency changes in the strong and weak grids, respectively. However, only a 1 Hz step change is applied in the third test to verify the steady-state errors of the LPV-PSGFLI strategy.

Fig. 62(a), (d) and (g) shows the performance of the proposed ePSGFLI strategy in the strong grid with the SCR= 7.5 upon the step change of the active and reactive power and frequency deviations at t_1, t_2 and t_3, respectively. On the one hand, it can be observed that the proposed ePSGFLI ensures seamless dynamic performance without any significant oscillations upon changes of the active and reactive power set-points at t_1 and t_2, respectively. Additionally, the ePSGFLI regulates the output active and reactive power accurately to the desired set-points with zero steady-state errors upon the grid frequency deviation from 50 Hz to 45 Hz at t_3, as shown in Fig. 62(g) Similar findings can be observed for the seamless dynamic performance

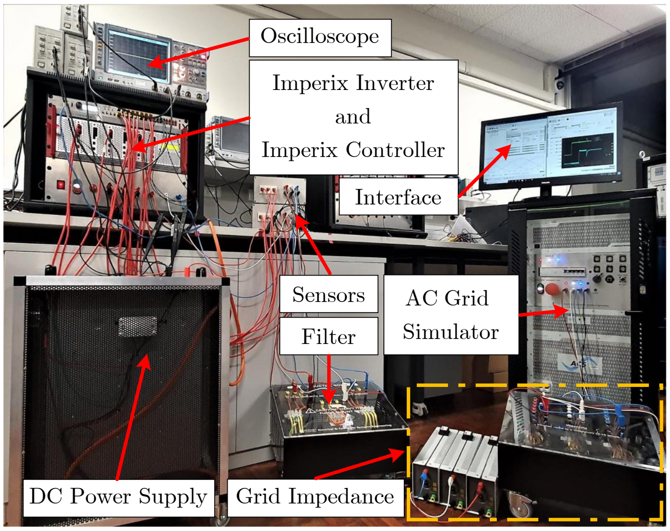

Figure 61: The experimental scaled-down setup used to validate the performance of the ePSGFLI.

of the proposed ePSGFLI in the weak grid with the SCR= 1.38, as shown Fig. 62(b), (e) and (h).

On the other hand, Fig. 62(c), (f) and (i) presents the experimental results of the inverter output current, the power, and the frequency estimated by the LPV-PSGFLI in the weak grid with the SCR= 1.38, respectively. It is evident that the LPV-PSGFLI has poor dynamic performance when the grid frequency deviates from its nominal value of 50 Hz by 1 Hz at t_3. This frequency deviation results in steady-state errors in the inverter output power.

4.3 PSGFLIs Under Unbalanced Grid Faults

4.3.1 Double-Synchronous-Reference-Frame-Based Control of PSGFLIs

The above-mentioned three control strategies for the PSGFLIs (optimization-based PSGFLI, LPV-PSGFLI, and ePSGFLI are designed based on an assumption that the inverter operates in balanced grid voltage conditions. However, the performance of these three control strategies deteriorates significantly under asymmetrical faults, which often occur in power systems due to single or double line-to-ground faults. When unbalanced events occur, uncontrollable oscillations at the double grid frequency are produced in the inverter control loop implemented in the SRF [41–43]. The magnitude of these oscillations proportionally depends on the severity of the faults/unbalanced events. Furthermore, unlike the commonly-used PCC control strategies, the optimization-base PSGFLI, LPV-PSGFLI, and ePSGFLI regulate output power at the inverter terminal instead of the PCC leading to two challenges (heavy filtering requirements and large voltage drop across the inverter output filter especially for inverters with high-power ratings).

In this section, the DS-PSGFLI is proposed to cope with faults/unbalanced grid voltage events. This control structure ensures balanced current injection even under severed faults/unbalanced grid voltage events. Additionally, the proposed DS-PSGFLI regulates the PCC output power, similar to commonly-used PCC control strategies in GFLIs and GFMIs. The control detailed control structure of the DS-PSGFLI is shown in Fig. 63. The proposed DS-PSGFLI independently regulates the positive and negative sequences of the PCC voltage ($v^+_{\text{pcc}}, v^-_{\text{pcc}}$) and current ($i^+_{\text{pcc}}, i^-_{\text{pcc}}$) measurements. After extracting these sequences, the positive active power (P^+_{pcc}) and positive reactive power (Q^+_{pcc}) at the PCC are used in the outer power loop to generate the reference current of the d-component of the positive sequence ($i^+_{\text{d-ref}}$) and θ^+ as given

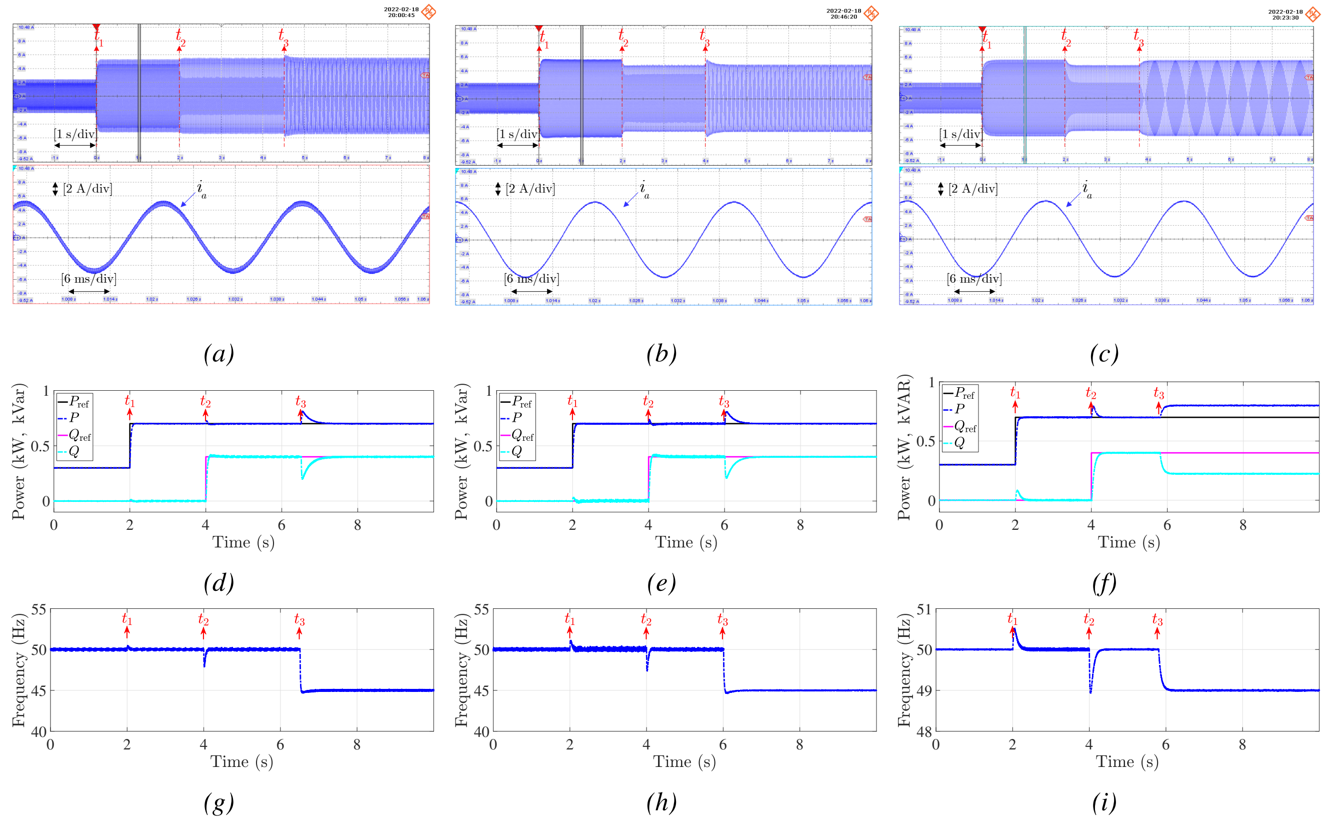

(a) (b) (c)

(d) (e) (f)

(g) (h) (i)

Figure 62: The PCC current waveform of phase A, the output power waveforms and the extracted frequency. (a), (d) and (g) The proposed ePSGFLI in a strong grid (SCR= 7.4), (b), (e) and (h) The proposed ePSGFLI in a weak grid (SCR= 1.38), and (c), (f) and (i) The LPV-PSGFLI in a weak grid (SCR= 1.38).

below

$$\begin{cases} \begin{bmatrix} \omega^{+} \\ i^{+}_{\text{d-ref}} \end{bmatrix} = \begin{bmatrix} K_{11}(s) & K_{12}(s) \\ K_{21}(s) & K_{22}(s) \end{bmatrix} \begin{bmatrix} P_{\text{ref}} - P^{+}_{\text{pcc}} \\ Q_{\text{ref}} - Q^{+}_{\text{pcc}} \end{bmatrix} + \begin{bmatrix} \omega^{+}_{\text{g-ref}} \\ 0 \end{bmatrix}, \\ \theta^{+} = \frac{\omega^{+}}{s}, \end{cases} \tag{75}$$

where $K_{11}(s)$ to $K_{22}(s)$ are the transfer functions of the power controllers. $\omega^{+}_{\text{g-ref}}$ is the angular frequency reference of the grid, which is equal to $2\pi 50$ rad/s.

Performance Validation:

Experiments are conducted based on a scaled-down setup in order to evaluate the proposed DS-PSGFLI shown in Fig. 75. Three tests are conducted in which the inverter is rated at 1 kW and connected to the grid (100 $V_{\text{L-L, RMS}}$, 50 Hz). The programmable AC grid simulator is used for implementing the unbalanced events (asymmetry voltage sag of 50% in phase B). In the first and second tests, the proposed DS-PSGFLI is tested in a strong grid with an SCR= 5.3 and a weak grid with an SCR= 1.0, respectively. The third test examines the shortcoming of the optimization-based PSGFLI [40] under unbalanced fault in the same weak grid condition.

Fig. 64(a), (d) and (g) presents the performance of the proposed DS-PSGFLI strategy in the strong grid with the SCR= 5.3 under the permanent voltage sag of 50% in phase B. It can be seen that the inverter operates stably and injects balanced currents to the grid; see Fig. 64(a). The injected positive active and reactive power also follow their desired references without any oscillations, as shown in Fig. 64(d). Fig. 64(g) shows that the generated frequency by the DS-PSGFLI is free from oscillations. A similar

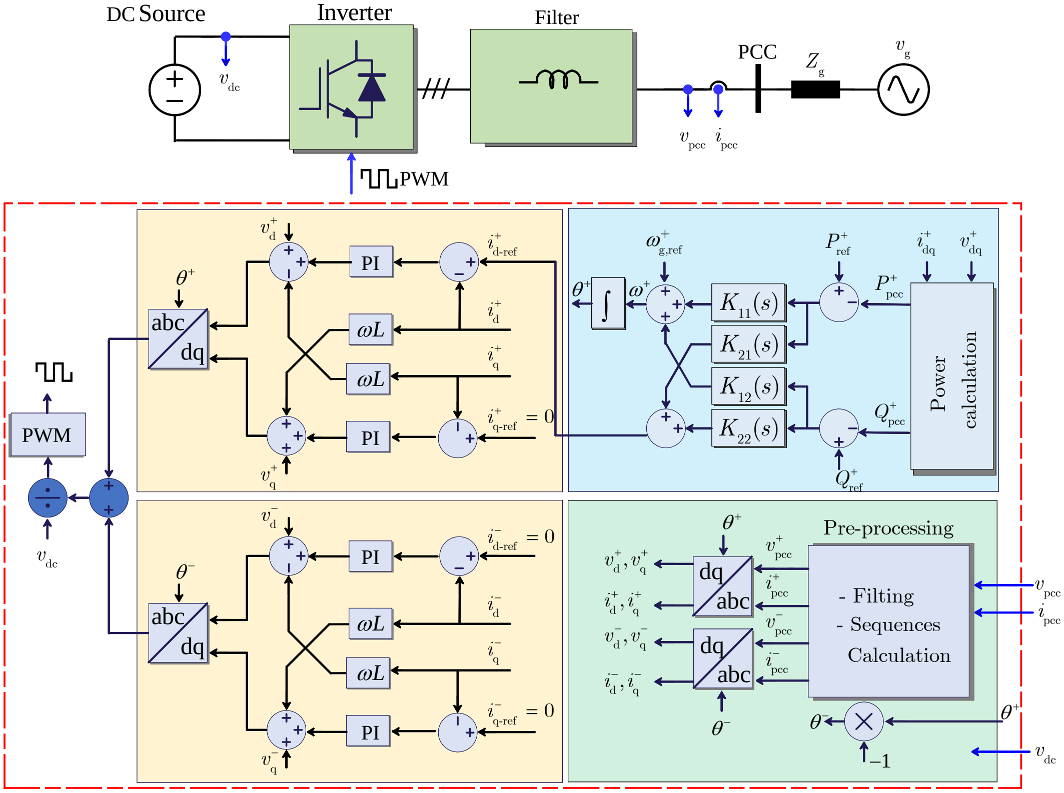

Figure 63: The proposed DS-PSGFLI for unbalanced grid faults.

analysis can be concluded for the performance of the proposed DS-PSGFLI strategy in the weak grid with the SCR= 1.0 shown Fig. 64(b), (e) and (h).

Contrary to the seamless dynamic performance of the proposed DS-PSGFLI strategy, the optimization-based PSGFLI suffers from oscillations due to the voltage sag. Fig. 64(c) shows that the injected currents to the grid are unbalanced. Additionally, there are high oscillations at 100 Hz in the inverter output power and the inverter estimated frequency as shown in Fig. 64(f) and (i), respectively.

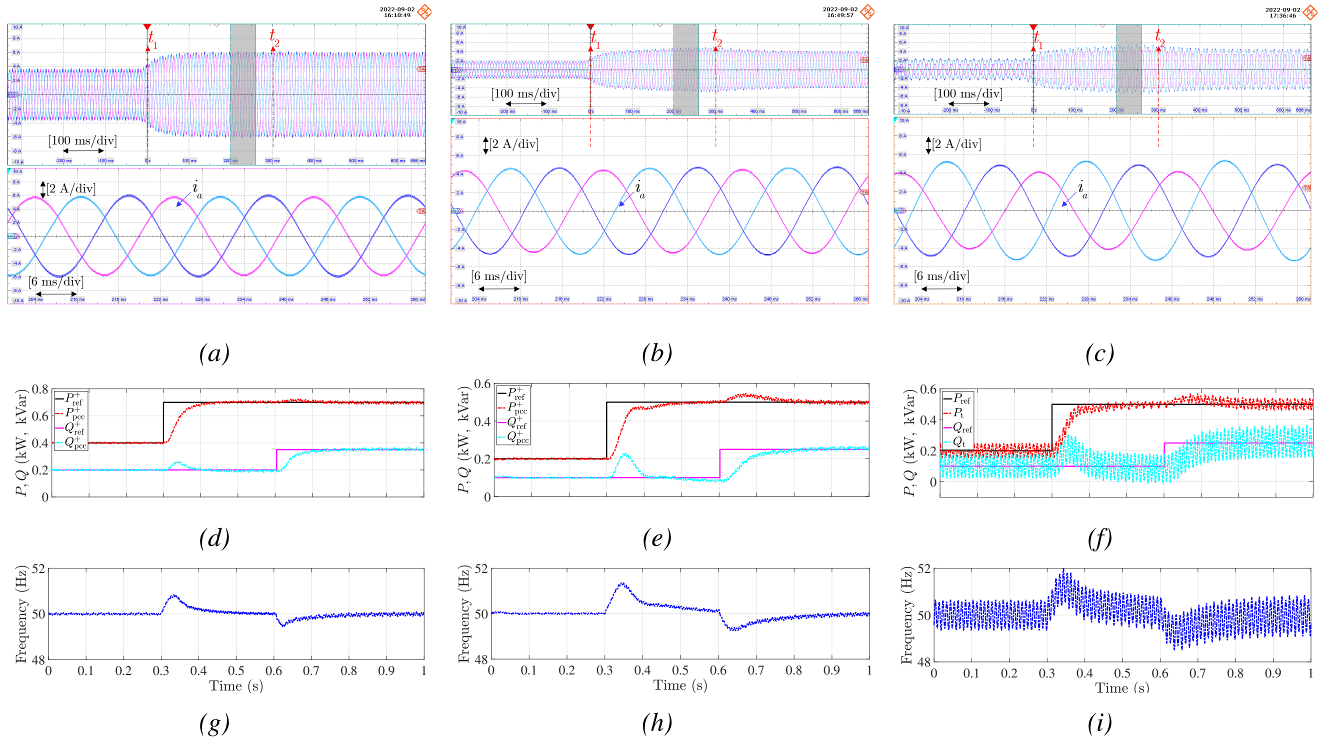
(a) (b) (c)

(d) (e) (f)

(g) (h) (i)

Figure 64: The PCC current waveform of phase A, the output power waveforms and the extracted frequency under the permanent voltage sag of 50% in phase B. (a), (d) and (g) The DS-PSGFLI in a strong grid (SCR= 5.3), (b), (e) and (h) The DS-PSGFLI in a weak grid (SCR= 1.0), and (c), (f) and (i) The optimization-based PSGFLI in a weak grid (SCR= 1.0).

5 Grid-Forming Inverters

GFMIs are being considered as the key enabling technology towards 100% renewable energy grids. Unlike GFLIs, which are controlled as current sources, GFMIs are controlled as voltage sources. Whereas GFLIs suffer from oscillations and instabilities in weak grids, GFMIs operate seamlessly in weak grids and they can switch between the GCM and SM. In GFMIs, the voltage magnitude and angle of the PCC voltage are dynamically controlled to inject the desired achieve active and reactive power into the grid.

5.1 Control Structure of a Typical GFMI

The detailed control diagram of the GFMI is shown in Fig. 65. The GFMI operates in the GCM and it is connected to a resistive-inductive grid. The inner current and voltage loops are considered in the control structure of the GFMI for better performance during faults, such as enabling current limiting capabilities. In this project, the main focus is on proposing new control techniques for the primary controller that include the Active Power Controller (APC) and Reactive Power Controller (RPC) of the VSG-based GFMIs. It is worth mentioning that the control objective of GFMIs in the GCM is to precisely track the dispatch commands of the active and reactive power with a low overshoot and short settling time. in the SM, the control objective is to provide virtual inertia to slow the RoCoF after a disturbance. However, the VSG-based GFMIs cannot meet both objectives simultaneously as the damping and controller bandwidth are related to both the droop coefficient and the inertia constant [44]. To address this trade-off, the primary control loop of VSG-based GFMIs should be redesigned to fulfill these control objectives. Furthermore, while GFMI operates seamlessly in weak grids, its performance significantly deteriorates in strong grids. The root cause of this issue is associated with the inherent coupling of the active and reactive power flow due to the grid impedance, as will be explained in the next section.

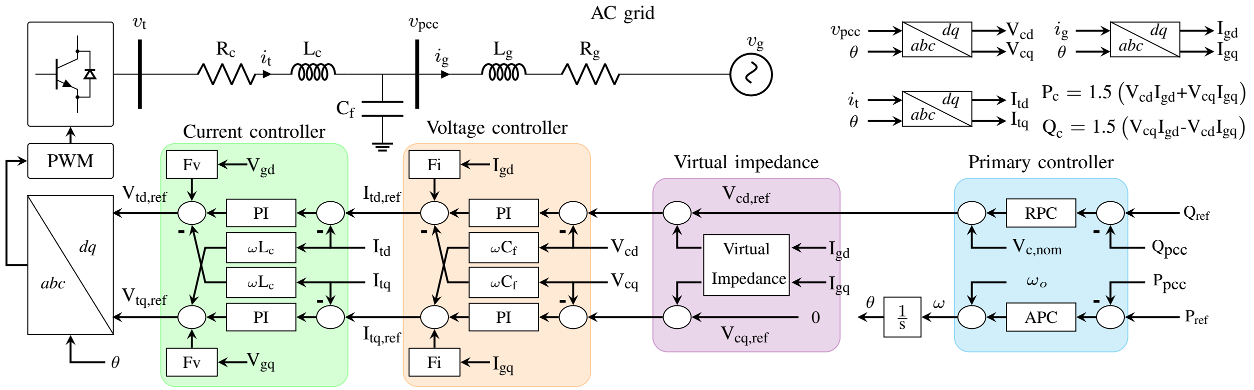

Figure 65: The detailed control diagram of the GFMI .

5.2 Performance of VSG-based GFMI in the GCM

This section examines the inherent coupling between the active and reactive power injected by the VSG-based GFMI and how the performance of the VSG is dependent on grid strength and type. The output APC and RPC are inherently coupled with both the voltage amplitude and phase as shown in (76) and (77).

$$P_{pcc} = \frac{3}{R_g^2 + X_g^2}[R_g(V_{pcc}^2 - V_{pcc}V_g\cos\theta_{pcc-g}) + X_gV_{pcc}V_g\sin\theta_{pcc-g}], \tag{76}$$

$$Q_{pcc} = \frac{3}{R_g^2 + X_g^2}[X_g(V_{pcc}^2 - V_{pcc}V_g\cos\theta_{pcc-g}) - R_gV_{pcc}V_g\sin\theta_{pcc-g}], \tag{77}$$

where V_{pcc} and V_{g} are the RMS values of the grid voltages at the PCC and the grid-side (AC bus), respectively. R_{g} and X_{g} are the grid resistance and inductance, respectively. $\theta_{\text{pcc-g}}$ is the phase angle difference between V_{pcc} and V_{g}.

Fig. 66 shows the step responses of the VSG output active power under different grid conditions. In Fig. 66 (a) and (b), the step responses of the VSG output active power are examined under three different SCR values when $X_{\text{g}}/R_{\text{g}}$ is 3.0 and 1.0, respectively. It can be seen that the VSG performance deteriorates in strong grids, especially for grids with smaller $X_{\text{g}}/R_{\text{g}}$ ratios. Fig. 66 (c) shows the step response of the VSG deteriorates when the grid impedance magnitude is increased while $X_{\text{g}}/R_{\text{g}}$ ratio remains unchanged.

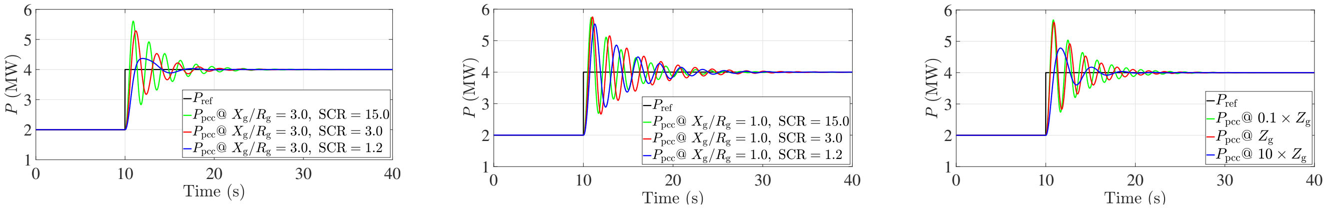

(a) *(b)* *(c)*

Figure 66: Performance of VSG-based GFMI in the GCM upon a change in the active power reference form 2 to 4 MW: (a) Different SCRs when $X_{\text{g}}/R_{\text{g}}$ = 3.0, (b) Different SCRs when $X_{\text{g}}/R_{\text{g}}$ = 1.0, and (c) Variations of Z_{g} magnitude when $X_{\text{g}}/R_{\text{g}}$ = 3.0.

5.3 Proposed Control Strategies for GFMIs

This section presents different control strategies that have been proposed during this project in order to enhance the performance and stability of VSG in the GCM. The proposed control strategies are explained briefly next.

5.3.1 Adaptive Control of VSG-based GFMIs

An adaptive VSG based on the online grid impedance estimation is proposed to permit accurate control of the VSG by mitigation of the inherent power coupling [45]. Fig. 67 shows the control structure of the proposed AVSG. While this control structure is very similar to the conventional VSG, the control parameters of the primary control loop (D_p, J, K_{pq}, and K_{iq}) of the AVSG are being adaptively tuned to meet the desired/pre-defined dynamic performance (e.g., settling time and damping) regardless of the grid strength (strong vs weak) or type (inductive vs resistive).

The adaptive tuning procedure of D_p, J, K_{pq}, and K_{iq} is realized based on the SSM of the VSG and the linearised power flow equations shown in (76) and (77). Hence, the grid impedance (resistance and inductance) value is required. To tackle this challenge without the need for additional hardware and to reduce the associated impacts on power quality, an online event-based grid impedance estimation algorithm is embedded in the control loop of the AVSG.

Fig. 68 shows the flow chart of the proposed AVSG algorithm, including the online Grid Impedance Estimation (GIE) algorithm and the adaptive tuning of the VSG. The proposed algorithm is summarized below:

1. Once the inverter is started, the initial fixed values for J, D_p, K_{pq}, and K_{iq} are used if the inverter is operating in the IM or in the GCM while the proposed AVSG is disabled.

2. Once the AVSG is enabled by the operator, the GIE algorithm is activated immediately to initialize the values of the impedance components R_g and X_g. These estimated values are used in the next step to calculate the linearized terms of the power flow.

3. The control parameters J, D_p, K_{pq}, and K_{iq} of the VSG-based inverter are calculated in real-time based on the method proposed. Therefore, the inverter can now connect to the grid, and the desired response with the desired natural frequency and damping is ensured.

4. Afterwards, the inverter power reference commands are read and continuously monitored for any changes. Therefore, an enabling signal is automatically generated each time the power reference commands are changed.

5. The enabling signal is used to delay the power reference commands for a time duration equal to the required time for the GIE algorithm. At the same time, the grid impedance parameters are estimated again in real-time to ensure reliable monitoring of the grid impedance variations.

6. Then, the updated impedance values are used to recalculate J, D_p, K_{pq} and K_{iq}. By doing so, the inverter can cope with both strong and weak grid conditions, as the effects of the grid impedance are resolved in real-time by the adaptive tuning of the control parameters of the inverter.

Further details on the proposed AVSG can be found in [45].

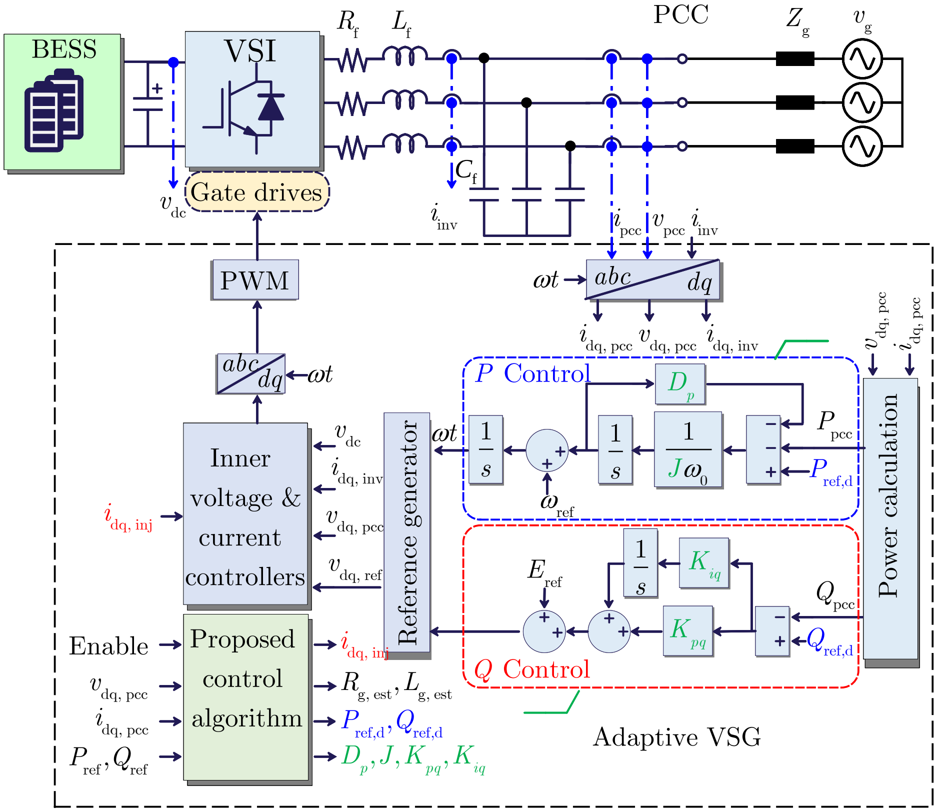

Figure 67: Control structure of the proposed AVSG-based GFMIs to cope with strong and weak grid conditions [45].

The experimental tests based on a scaled-down setup are conducted to validate the effectiveness of the proposed AVSG shown in Fig. 67. The tests also include the conventional VSG for comparison purposes. Both the AVSG and the conventional VSG are rated at 1 kW. Fig. 69 shows the experimental setup and Table 8 lists the system parameters used for the experiment.

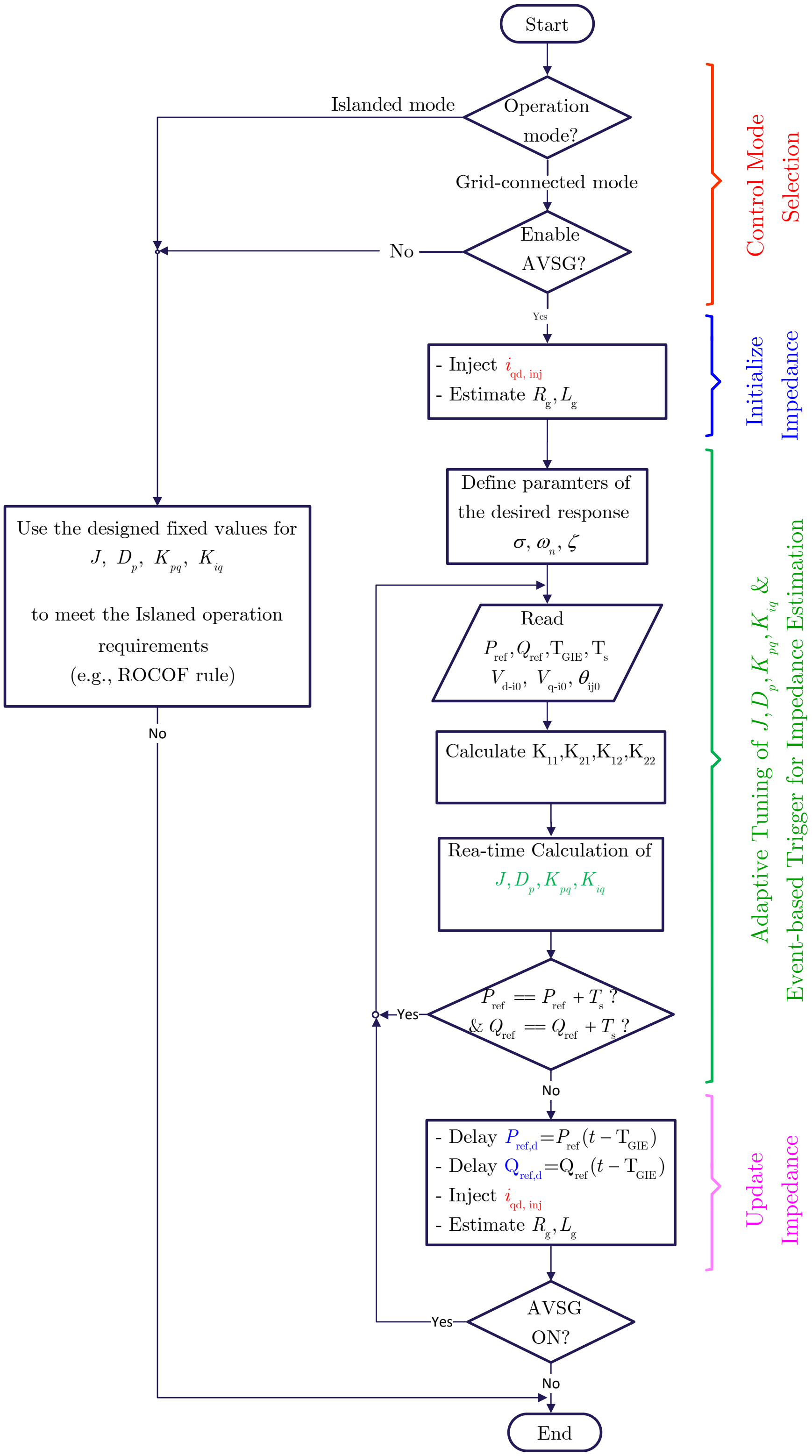

Figure 68: Flow chart of the proposed AVSG [45].

The performance of the controllers is tested in both strong and weak grids. In each test, step changes in the active and reactive power reference commands are applied. The times of application of these tests are referred to as t_1, t_2, and t_3. Initially, both inverters operate in the steady-state where the power reference commands are $P_{\mathrm{ref}} = 200$ W and $Q_{\mathrm{ref}} = 0$ Var. Then, for the proposed AVSG, the control algorithm is enabled at t_1, and the values of $i_{\mathrm{d-inj}}$ and $i_{\mathrm{q-inj}}$ required for grid impedance estimation are set to 0.25 A. After 5 s of enabling the AVSG, a step change in the active power reference command from 200 to 800 W is applied at t_2. Finally, a step change in the reactive power reference command from 0 to 150 Var is applied at t_3.

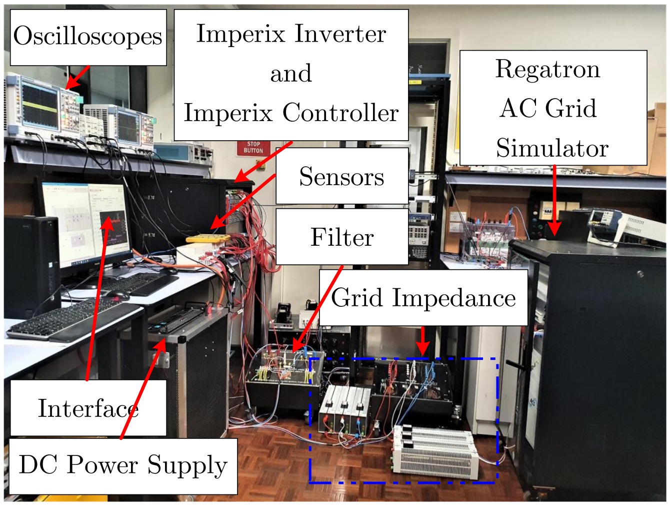

Figure 69: The experimental setup.

Quantity	Value	Unit	Description
Grid parameters			
v_g	110	V	Grid voltage (L-L)
f	50	Hz	Nominal frequency
R_g, L_g	0.85, 3.0	Ω, mH	Strong grid with SCR= 6.74
R_g, L_g	0.67, 10.5	Ω, mH	Weak grid with SCR= 2.54
Inverter parameters			
S_{base}	1.4142	kVA	Inverter rated power
P_{base}	1.0	kW	Inverter rated active power
v_{dc}	320	V	DC Bus voltage
f_{sw}	20	kHz	Inverter PWM carrier frequency
L_f	4	mH	Filter inductance
R_f	0.06	Ω	Filter resistance
C_f	30	μF	Filter capacitance
Fixed parameters for the conventional VSG			
D_p	318.3	W/Hz	Damping coefficient
J	1.013	kg.m^2	Inertia coefficient
K_{pq}	7.18×10^{-3}	VAR/V	Proportional gain of reactive power controller
K_{iq}	1×10^{-5}	1/s	Integral gain of reactive power controller

Table 8: Parameters of the experimental setup.

Performance Validation:

Fig. 70 and Fig. 71 show the experimental results of the proposed AVSG and the conventional VSG in the strong grid with an SCR= 6.7 and weak grid with an SCR= 2.5 upon the changes in the active and reactive power references in the GCM. On the one hand, the investigated tests show clearly that the proposed AVSG ensures the desired dynamic performance (the rising time and damping) in both strong and weak grid conditions when the change in the active power reference command is applied at $t_2 = 10\ s$. On the other hand, the conventional VSG produces significant oscillations in the output waveforms, especially in the strong grid in which these oscillations last for almost 10 s.

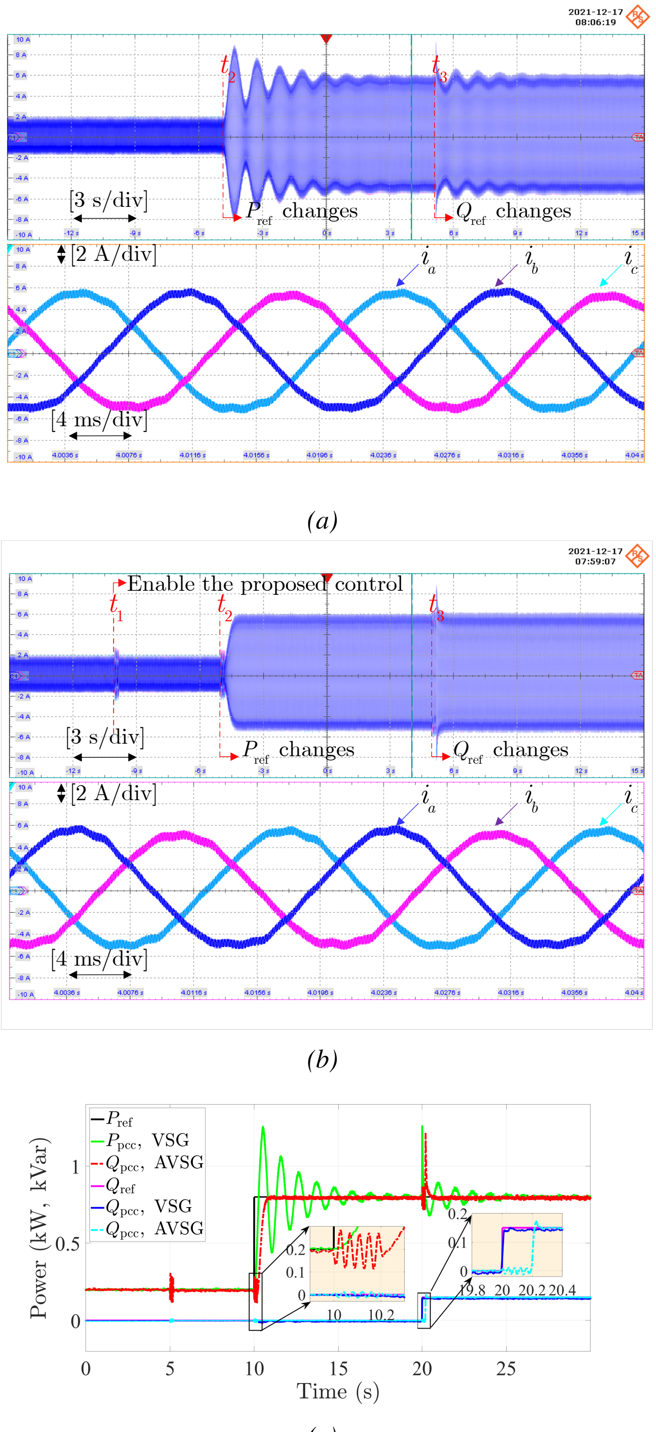

(a)

(b)

(c)

Figure 70: Experimental results of the conventional and proposed AVSG in a strong grid with an SCR= 6.7: (a) PCC current of the conventional VSG, (b) PCC current of the proposed AVSG, and (c) PCC power.

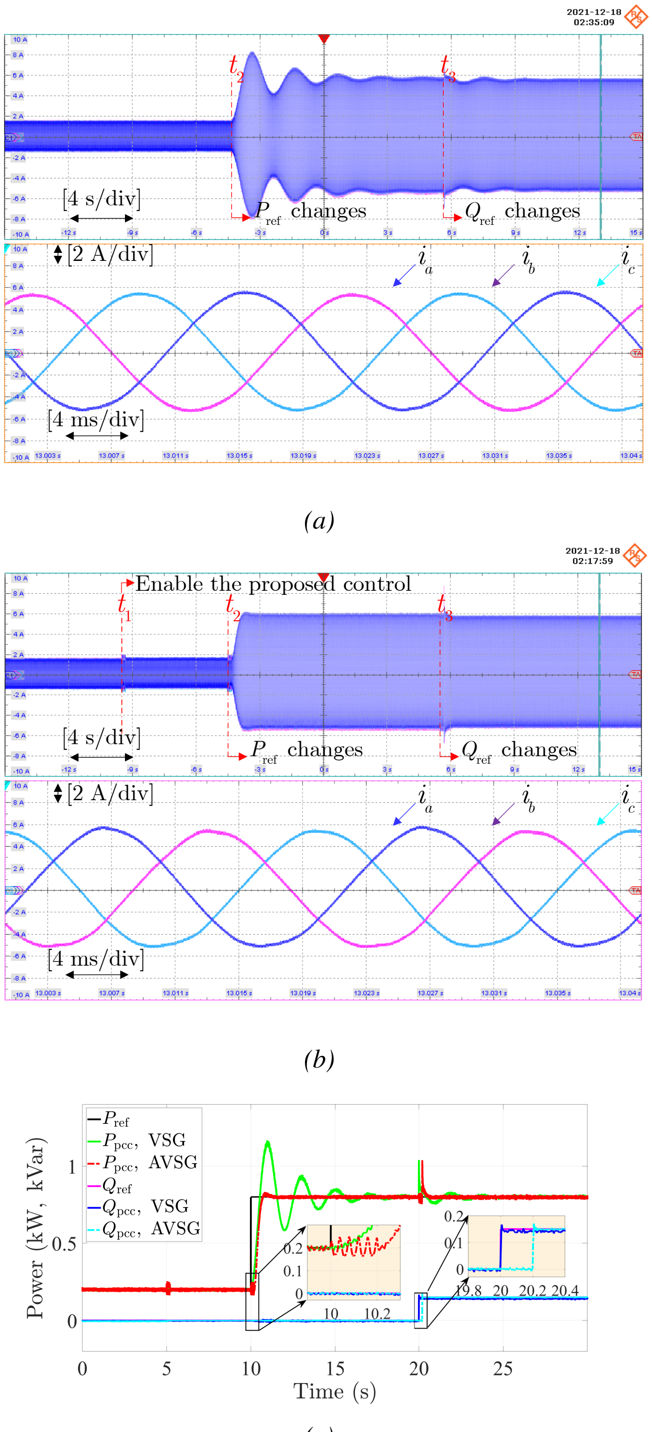

(a)

(b)

(c)

Figure 71: Experimental results of the conventional and proposed AVSG in a weak grid with an SCR= 2.5: (a) PCC current of the conventional VSG, (b) PCC current of the proposed AVSG, and (c) PCC power.

5.3.2 Generalised VSG Control

The main control objective of GFMIs in the GCM is to follow the dispatch commands from the automatic generation controller as quickly and accurately as possible. In addition, the APC controllers in GFMIs must also provide sufficient virtual inertia in the SM to slow down RoCoF following a disturbance. One of the shortcomings of VSG control is that the tuning of parameters such as closed-loop bandwidth and damping ratio is constrained by the droop coefficient and inertial time constant. Therefore, a VSG controller designed for a high virtual inertia provision in the SM could cause a large overshoot and a long settling time in step response in the GCM. In contrast, the GFMI could end up causing a large RoCoF following a disturbance in the SM if the VSG controller is designed to have a low overshoot and short settling time for step response in the GCM [44].

The root cause for this performance deterioration in VSGs is directly associated with the lack of damping and fast rise times that result from the chosen VSG parameters such as droop coefficient and inertia coefficient. In VSGs, the droop coefficient and the inertia coefficient are inherently tied with the damping ratio and the bandwidth of the closed-loop system. In addition, regardless of whether the grid is inductive or resistive, meaning that the active and reactive powers of the GFMI are coupled, the impedance of the grid influences the step response characteristics with a VSG controller. Therefore, tuning VSG controller parameters to achieve control objectives in both GCM and SM is challenging. To achieve both objectives in the GCM and SM, either the droop coefficient or the inertia coefficient has to be compromised. For a detailed analysis on this phenomena readers are referred to [46].

A first-order controller such as VSG control cannot concurrently achieve both control objectives stipulated in the GCM and SM. As such, Generalised Virtual Synchronous Generator (GVSG) controller and CGVSG are proposed to obviate the shortcomings of the VSG controller in the GCM and SM. Based on the frequency response of the controller, a condition for pole placement to guarantee post-disturbance RoCoF compliance is developed. Finally, a straightforward analytical approach for designing the proposed controllers to achieve the control objectives of both GCM and SM is proposed. A novel control structure called the GVSG control is introduced. Based on the GVSG, an enhanced controller called the CGVSG that exhibit superior performance in both GCM and SM compared to state-of-the-art approaches is proposed. A condition for placement of the poles of the controllers for guaranteeing RoCoF following a disturbance in the SM is derived. Since only the plant gain is required for control design, both parametric and experimentally identified non-parametric models can be used. A methodical analysis of the dynamic response of the GFMI with the proposed controllers based on the open-loop frequency response of the system is presented. Consequently, a straightforward control design method to tune the controller gains is proposed.

The control block diagrams of GVSG and the CGVSG control strategies are shown in Fig. 72. The control design of these controllers to calculate the coefficients α, β, and γ is governed by three straight forward equations. Although, these equations require the grid (plant) model, which is typically inductive in transmission networks, it can be easily estimated or the controller gains could be tuned iteratively to reach the required performance. One of the key advantages of GVSG and the CGVSG is neither the droop coefficient or the inertia coefficient has to be compromised to achieve the required performance from the GFMI. This is particularly important when the droop coefficient is mandated by the grid operator based on the grid frequency variation and the available power reserve. During contingencies, the grid operator expects the IBRs to support the grid. The amount of support is mandated through the droop coefficient of the GFMI.

Fig. 73 and Fig. 74 compared the performance of the GFMI rated at 1 kW in a strong grid with an SCR= 10.6 and in a weak grid with an SCR= 1.9 when the APC channel of the GFMI is equipped with VSG, GVSG and CGVSG. The obtained results confirm the superior performance of the GVSG and the CGVSG over the VSG control strategy. For instance, it can be seen that the CGVSG accurately tracks the power reference in the GCM upon applying the step change of 1 kW at $t = 2$ s. In both grid conditions, it can be seen that GVSG and CGVSG result in lower overshoots and shorter settling times in step responses than the conventional VSG. Furthermore, the CGVSG strategy shows to slow down the rate of change of frequency, which can be used for grid support during frequency transients and disturbances.

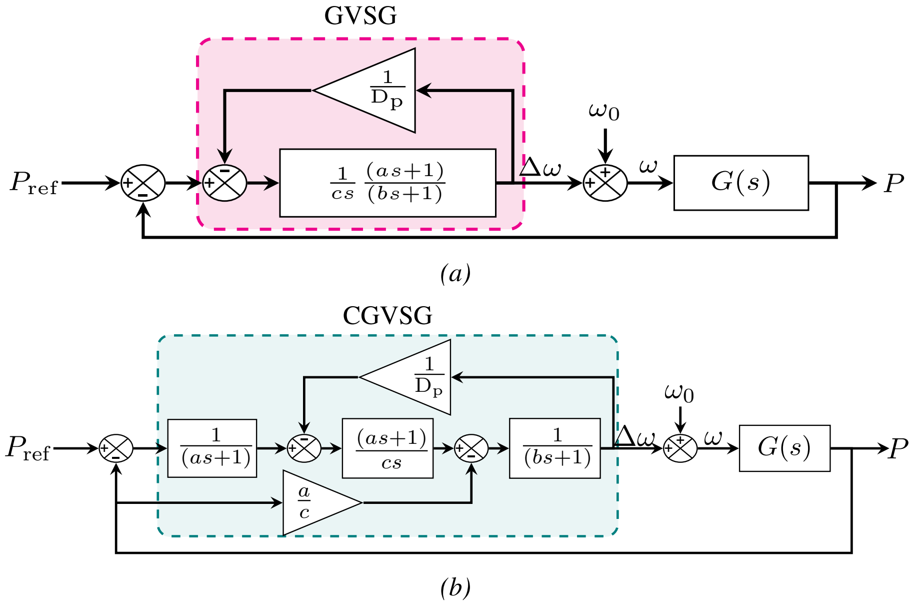

(a)

(b)

Figure 72: Control block diagrams proposed for the APC of GFMI : (a) GVSG and (b) CGVSG [46].

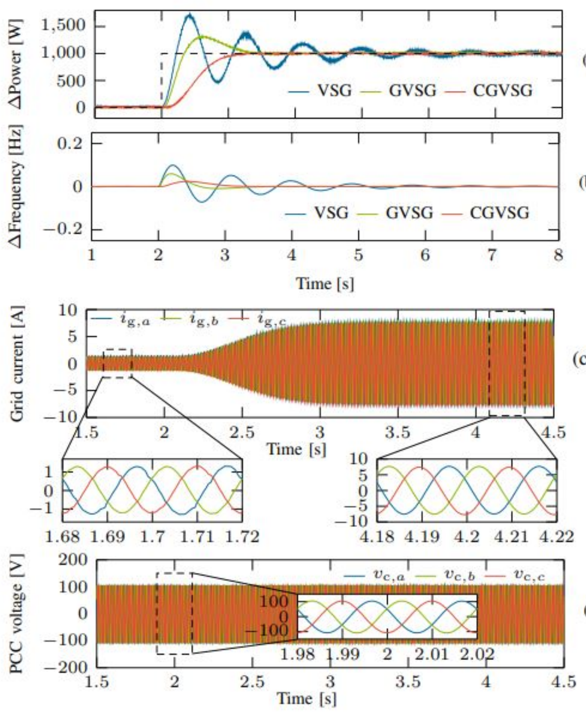

(a)

Figure 73: Experimental results of VSG, GVSG, and CGVSG upon a 1 kW step change in GCM for a strong grid with an SCR= 10.6: (a) active power, (b) frequency, (c) PCC current, and (d) PCC voltage.

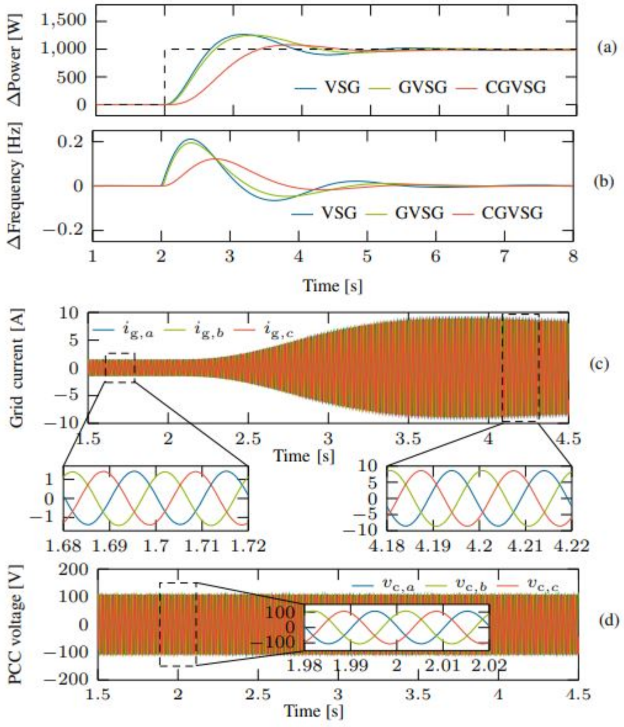

(a)

Figure 74: Experimental results of VSG, GVSG, and CGVSG upon a 1 kW step change in the GCM for a weak grid with an SCR= 1.9: (a) active power, (b) frequency, (c) PCC current, and (d) PCC voltage.

5.3.3 $\mathcal{H}_\infty$-based Control Design for GFMIs

The $\mathcal{H}_\infty$-based control design for GFMIs further enhances the advantages of the GVSG and CGVSG by identifying the plant model to accurately model the unmodeled dynamics and parameter uncertainty, and combining the identified plant model with a frequency-domain control design approach. The proposed $\mathcal{H}_\infty$-based control design is capable of working with an experimentally identified frequency response of the system. This is particularly advantageous when working with high-order plant models, where complex dynamics that are difficult to model are involved, and uncertainty of plant parameters. Therefore, a typical system identification method can be used to identify the frequency response of the system. In addition, methodical formulation of the performance specifications such as overshoot, rise-time, $P-\omega$ droop coefficient, and RoCoF relay withstand limit compliance in the SA mode as frequency-domain constraints on the ∞-norm of sensitivity functions is presented to be utilised in the $\mathcal{H}_\infty$-based control design approach.

In order to fulfill the control objectives of GFMIs in the GCM and SM, a second-order discrete-time controller is directly designed in [47]. The required performance specifications of the controller in the GC and SA modes are defined as constraints on the norm of the sensitivity functions. Therefore, a mixed-sensitivity problem is considered to tune the controller.The control strategy ensures a well-damped step response upon changes in the active power reference commands in the GCM while it adheres to the RoCoF requirements in the SM.

Fig. 75 presents the control block diagram of the H_∞-based GFMIs. $[x_2, x_1, x_0]$ and $[y_1, y_0]$ are the controller gains that need to be tuned. The methodical formulation of the performance requirements (e.g., overshoot, rise-time, $P-\omega$ droop coefficient, and RoCoF requirements in the SM) are defined as constraints on the norm of the sensitivity functions. Hence, the ∞-norm of the output sensitivity function ($\mathcal{S}(e^{j\omega})$) is considered to achieve acceptable tracking performance and output disturbance rejection.

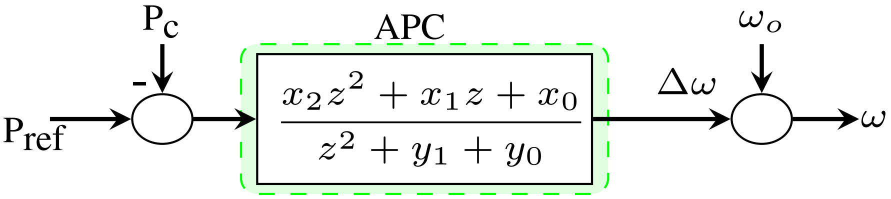

Figure 75: Control block diagram of the proposed H_∞-based GFMIs [47].

The control design process of the proposed controller is shown in Fig. 76. An $\mathcal{H}_\infty$-based method is used to tune the controller gains. The frequency domain constraints defined on the norms of the sensitivity functions guarantee that the performance of the controller conforms to the control objectives in both GCM and SM.

Performance Validation:
Fig. 77 and Fig. 78 provide the experimental verification of the proposed H_∞-based GFMI in GCM. The test conditions include a 1 kW step change in a strong grid (SCR= 10.6) and a weak grid (SCR= 1.9). These figures also compare the H_∞-based GFMI against the performance of the conventional VSG-based GFMI . Fig. 77 shows that the step change in the active power reference of the H_∞-based GFMI in the strong grid results in an overshoot of 25% with a settling time around 2 s. However, the overshoot and settling time of the conventional VSG-based GFMI are around 67% and 4.6 s, respectively. A similar conclusion can be concluded from the performance comparison in the weak grid as presented in Fig. 78.

Fig. 79 shows the experimental results in the SM upon a load disturbance of size 850 W connected at

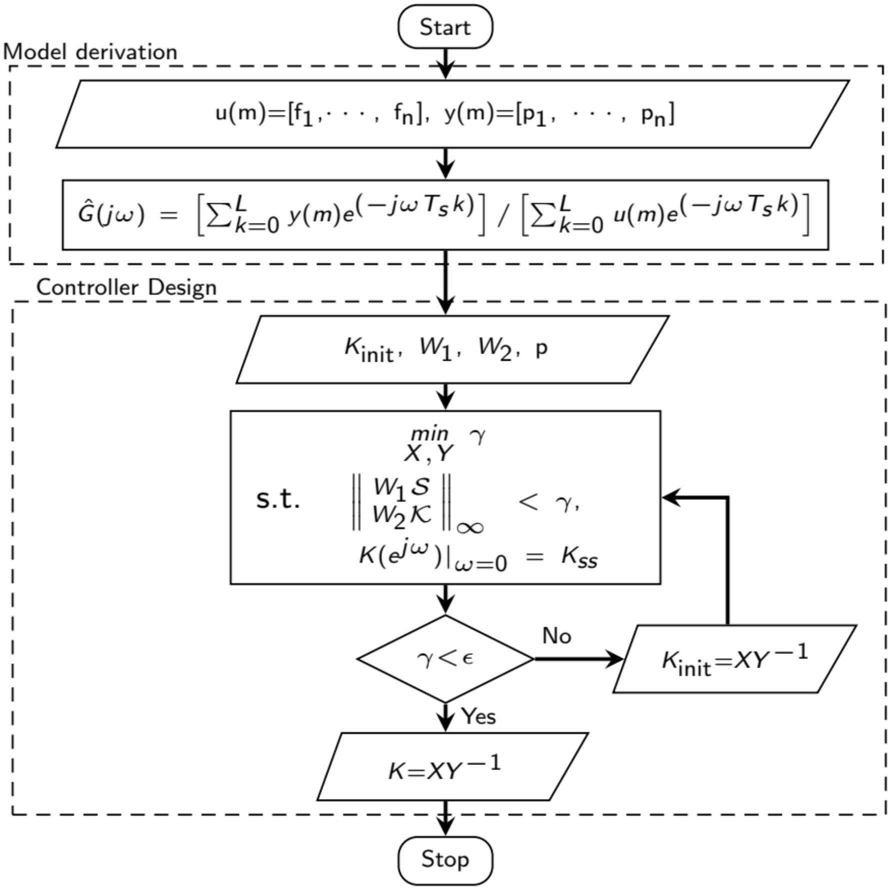

Figure 76: Control design of the proposed controller [47].

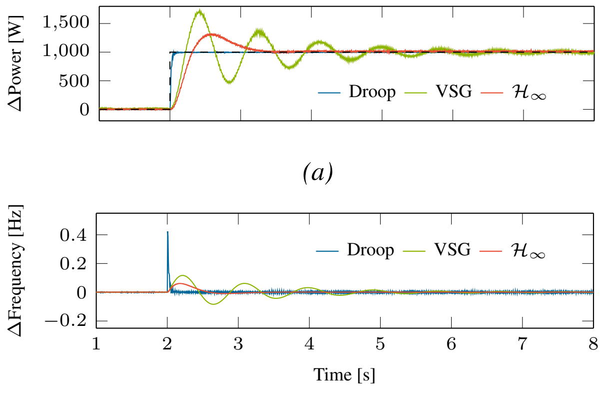

(a)

(b)

Figure 77: Experimental results of H_∞-based GFMIs upon a 1 kW step change in the GCM for a strong grid with SCR = 10.6: (a) active power and (b) frequency.

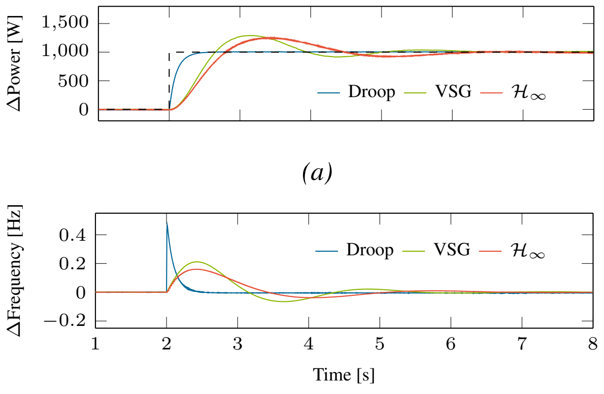

(a)

(b)

Figure 78: Experimental results of H_∞-based GFMIs upon a 1 kW step change in the GCM for a weak grid with SCR = 1.9: (a) active power and (b) frequency.

t = 2 s. The initial RoCoF of the VSG controller is set to 1 Hz/s. the results clearly indicate that the H_∞-based GFMI provides more virtual inertia to the system than the VSG-based GFMI . Furthermore, the H_∞-based GFMI enhances the performance as the frequency change over time is much slower.

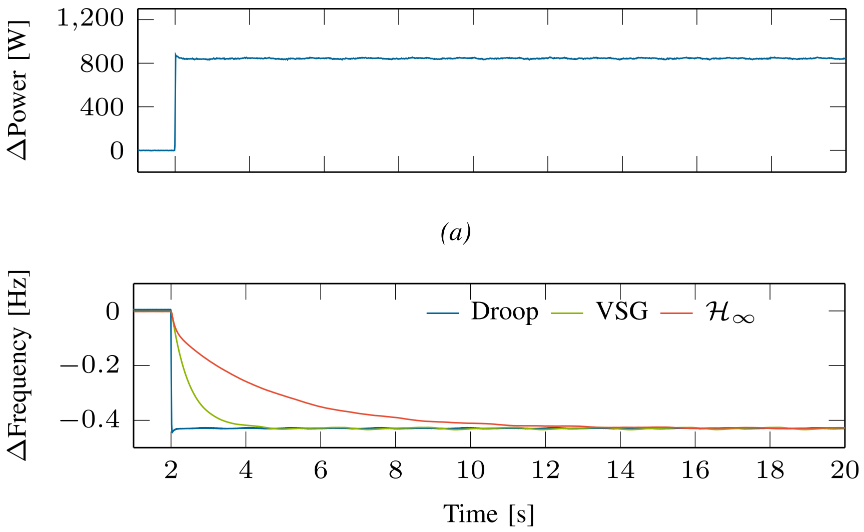

(a)

(b)

Figure 79: Experimental results for a load disturbance of 850 W in the SM: (a) change in active power, (b) change in frequency..

5.3.4 Multivariable Control Design for GFMIs

An Optimization-based Multivariable Primary Controller (OMPC) is proposed for GFMIs in order to fully decouple active and reactive control loops [48]. Fig. 80 presents the small signal model of the proposed control strategy and the grid. The cross-channel decoupling terms in the proposed OMPC ensure complete power decoupling. The transfer functions ($G_{\theta\to P}(s)$, $G_{V_c\to P}(s)$, $G_{\theta\to Q}(s)$, and $G_{V_c\to Q}(s)$) of the four controllers are designed using the loop-shaping approach. To design the controllers, a methodical formulation of the performance specifications such as rise-time and overshoot as frequency-domain constraints on the ∞-norm of open-loop transfer functions is presented. Furthermore, $\mathcal{H}_\infty$-based strategy is used to tune the parameters of the proposed OMPC. One of the key advantages of the proposed controller and the associated control design process is that the proposed controller and the control design can handle a variety of prevalent P and Q controllers for GFMIs. The proposed control structure and the $\mathcal{H}_\infty$-based loop-shaping control design enable the design of preferred control structures for the OMPC such as droop, VSG, zero steady-state error Q controller, and finite steady-state error Q controller to achieve the desired closed-loop dynamics. [48].

The proposed $\mathcal{H}_\infty$-based loop shaping control design method is shown in Fig. 81. One of the key advantages of this method is that it is capable of working with an experimentally identified frequency response of the system. Using this approach can be especially advantageous when dealing with plants that have complex dynamics that are difficult to model and when there is uncertainty in the parameters of the plant. The primary objective of the control design is to shape the open-loop transfer function matrix into a desired open-loop transfer function matrix. To this end, the objective function, which is the ∞-norm of the error between open-loop transfer function matrix and desired open-loop transfer function matrix, is minimized. The desired open-loop transfer function matrix defined based on the desired closed-loop characteristics of the active and reactive power loops.

Performance Validation:
Fig. 82 shows the experimental results of the proposed OMPC with zero steady-state error reactive power. The figure also compares the performance of the OMPC with the conventional VSG and VSG with a

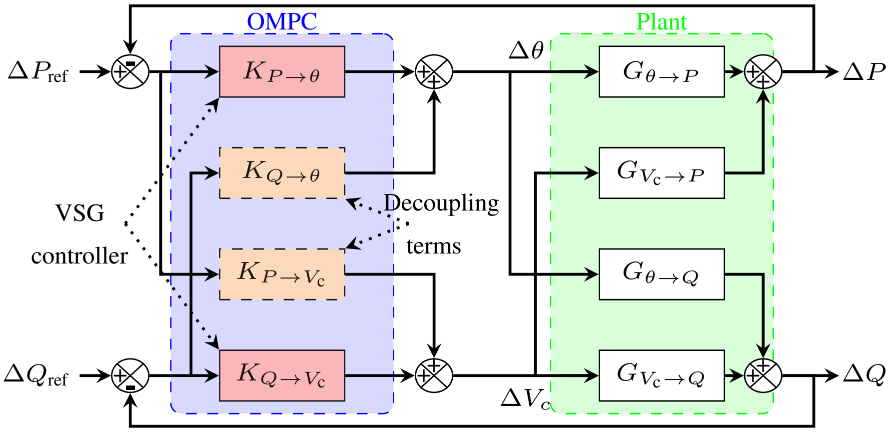

Figure 80: Proposed structure of the OMPC strategy for GFMIs [48].

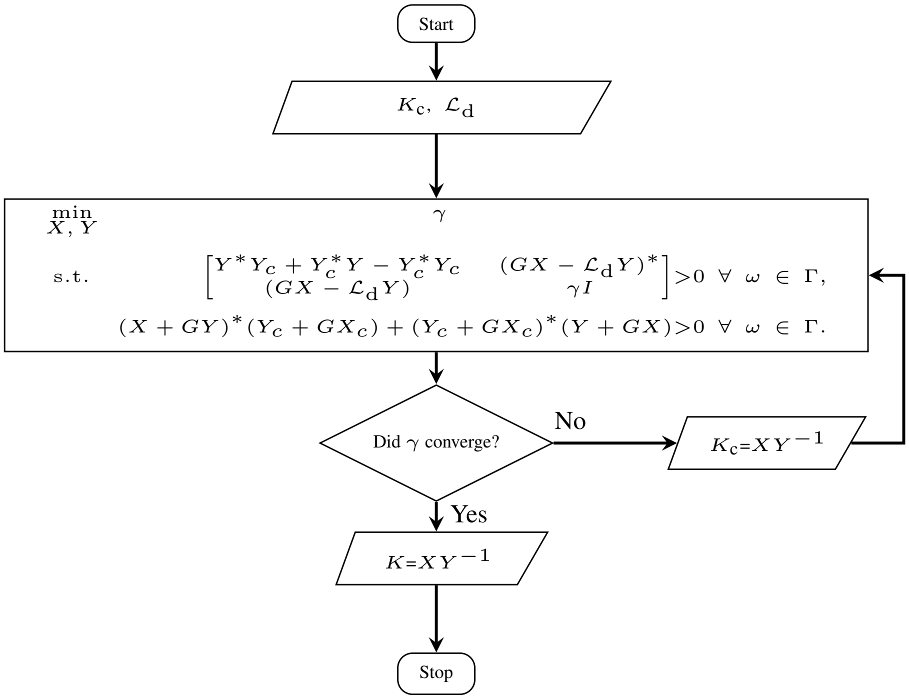

Figure 81: A flowchart of the optimization problem [48].

virtual Inductor-based Decoupling (VID) method. In these tests, the GFMI is rated 1 kW and connected to the grid (130$V_{\text{L-L, RMS}}$, 50 Hz). The grid impedance is set to R_g= 3.14 Ω and L_g= 10 mH.

Fig. 82(a) and (b) show that upon the step change of 500 W at 2 s, a significant transient occurs in the reactive power with the VSG. While this transient is reduced with the VID method, only the OMPC strategy is capable of full decoupling of the power upon changes in the active power reference. Fig. 82(c) and Fig. 82(d) show the d-axis PCC voltage reference deviation and q-axis PCC voltage reference deviation, respectively. The voltage control with the OMPC is similar to that with the VSG controller; only the d-axis PCC voltage reference deviation is dynamically controlled and the q-axis PCC voltage reference deviation is set to zero. Therefore, as shown in Fig. 82(c), following the step change in active power at t = 2 s, the d-axis PCC voltage reference deviation is increased to around 15 V with both VSG and OMPC. However, d-axis PCC voltage reference deviation has a shorter rise time with OMPC than that with the

VSG. Furthermore, following the step change in reactive power at t = 5 s, d-axis PCC voltage reference deviation is increased to around 19 V with both VSG and OMPC. On the other hand, as shown in Fig. 82(c) and Fig. 82(d), the VID method simultaneously controls both d-axis PCC voltage reference deviation and q-axis PCC voltage reference deviation. Therefore, as shown in Fig. 82(c), following the step change in active power at t = 2 s, the d-axis PCC voltage reference deviation and q-axis PCC voltage reference deviation are varied to around 11 V and -32 V, respectively, with the VID method. Furthermore, following the step change in reactive power at t = 5 s, the d-axis PCC voltage reference deviation and d-axis PCC voltage reference deviation are increased to 16 V and -28 V, respectively, with the VID method.

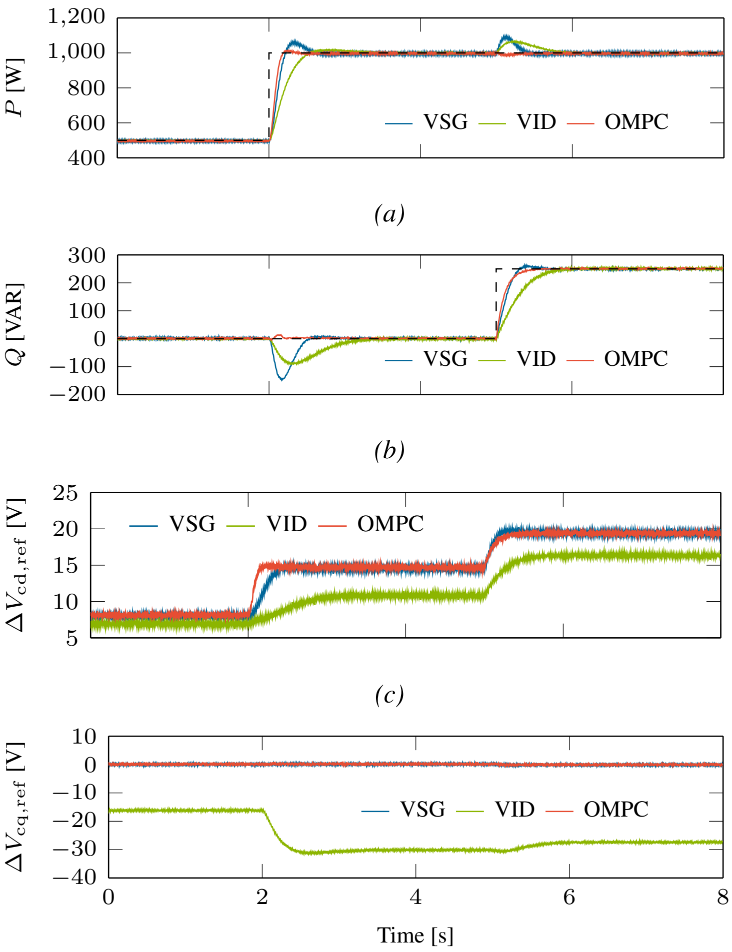

(a)

(b)

(c)

(d)

Figure 82: Experimental results of the VSG, VID, and OMPC with zero steady-state error Q controller during step changes of P and Q: (a) active power, (b) reactive power, (c) d-axis PCC voltage reference deviation, (d) q-axis PCC voltage reference deviation.

As shown in Fig. 83(b), the reactive power deviation following the active power step at t = 2 s becomes less as the virtual inductance is increased from 15 mH to 18 mH. However, the reactive power deviation following the active power step at t = 2 s starts to increase again as the virtual inductance is increased from 18 mH to 25 mH. Therefore, the optimal decoupling performance of the VID method is reached when the virtual inductance is 18 mH. However, the reactive power deviation following the active power step is still quite significant. As shown in Fig. 83(b), the reactive power deviation following the active power change with the VID method is less than the VSG control. However, as shown in Fig. 83(a), even with the VID method, the coupling between the active and reactive power loops cannot be eliminated. Furthermore, as shown in Fig. 83(a), as the virtual inductor value is increased, the damping and rise time of the active power step response is increased. Hence, although the VID method improves the decoupling performance, it affects the step response of the active power. As the virtual inductance is increased, the step response of the active power is slowed down.

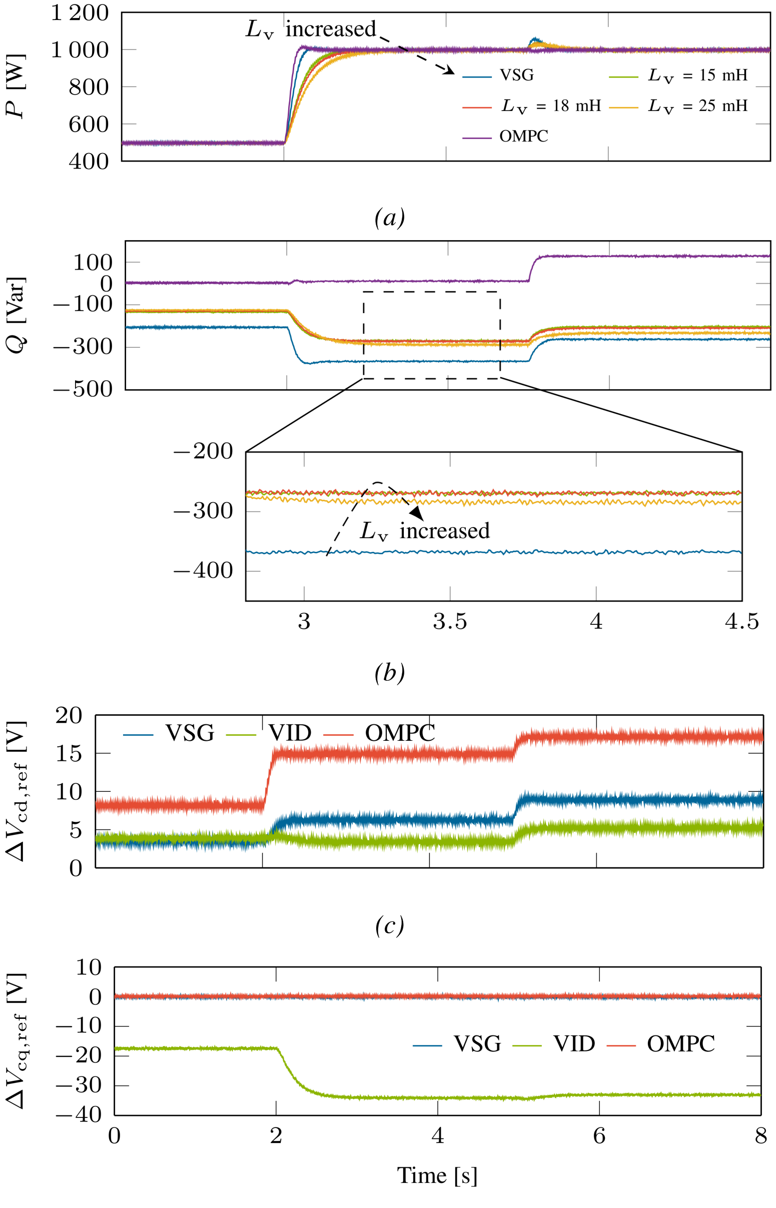

(a)

(b)

(c)

(d)

*Figure 83: Experimental results of the VSG, VID, and OMPC with fixed steady-state error **Q** controller during step changes of **P** and **Q**: (a) active power, (b) reactive power, (c) d-axis PCC voltage reference deviation, and (d) q-axis PCC voltage reference deviation.*

As shown in Fig. 83(a), the coupling on the active power as the reactive power is changed to 250 var is minimal with the OMPC. On the other hand, the VSG exhibits the most severe case of coupling between active power and reactive power. The VID method shows more coupling than with the OMPC but less than that with the VSG. However, the recovery to the original steady-state set-point of active power after a step change in reactive power is faster with the VSG than that with the VID method.

As shown in Fig. 82 and Fig. 83, the OMPC significantly outperforms the VSG controller and the VID method. The reactive power absorption with the OMPC in the steady-state is almost zero. Furthermore, the reactive power deviation following the active power step change is minimal. As shown in Fig. 83(a), unlike the VID method, the decoupling action of the OMPC does not affect the step response of the active power. Therefore, the active power step response of the OMPC achieves a faster response than the VID method. Therefore, the OMPC completely decouples the active and reactive power loops and significantly outperforms the VSG controller and the VID method in terms of decoupling performance.

5.4 Grid Forming Capabilities for Wind Turbine Generators

This section explores the possibilities of providing grid-forming capabilities for wind turbine generators, particularly Type 4 wind turbines. Fig. 84 shows a map showing weak points on the NEM and also a map of operational solar and wind farms in the Victorian Grid. As can be seen in this figure, there is a significant overlap between these maps indicating that there is a relationship between renewable resources and the grid strength. The reason behind this fact is most of the current renewable farms are operating as GFLIs.Also, more renewable farms will be installed and commissioned in the NEM, meaning that the situation may deteriorate if appropriate actions are not taken. GFMIs emerged to address this issue and, as explained in the previous subsections, are similar to voltage sources, unlike GFLIs, which function like current sources. Thus, GFMIs can technically form the voltage and the frequency at their PoC to the grid.

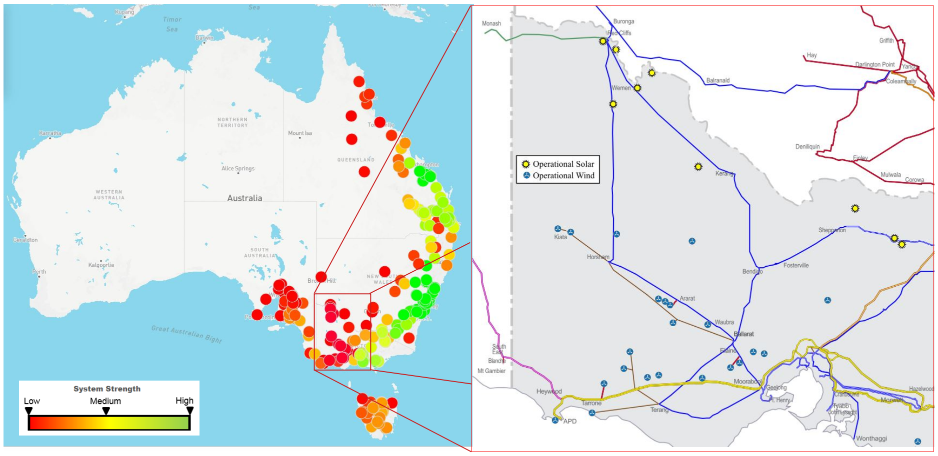

Figure 84: NEM grid strength map 2020-21 [49] and map of operational solar and wind farms in the Victorian Grid.

Currently, all existing GFMIs are based on Battery Energy Storage Systems (BESS), meaning that their DC side is connected to a battery, and the DC-link voltage is regulated and fixed by the battery system. Therefore, their control/regulated variables are only the PCC frequency, active and reactive power, voltage, and grid-side current. Fig. 85 shows three real examples of BESS-GFMIs worldwide [50]. As can be seen, all these examples are battery-based. Only one remarkable example of a GFMI interfaced with a wind farm is reported in the literature shown in Fig. 86 [50]. Although this farm, located in Scotland, was used in the grid-forming mode for a limited time (only six weeks), the reported responses of the farm against large frequency events were satisfactory. However, some operational limitations were reported regarding the farm operation when the wind speed was declining or the farm output power was near zero.

Since equipping the existing wind farms with grid-forming capabilities is one of the best cost-effective approaches for addressing the issues of renewable penetration in weak grids, this section investigates the

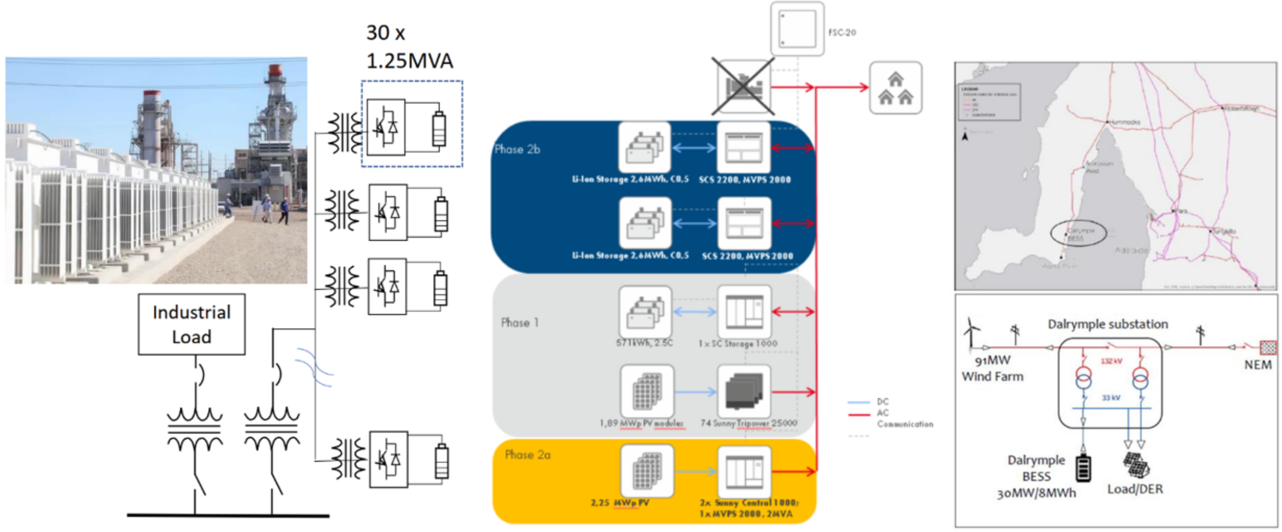

(a) (b) (c)

Figure 85: Real examples of BESS-GFMI worldwide. (a) 2017 GE BESS in Imperial Irrigation District (for Black Start), (b) 2017 SMA BESS in St. Eustatius Island, and (c) 2018 Hitachi-ABB Dalrymple BESS in South Australia [50].

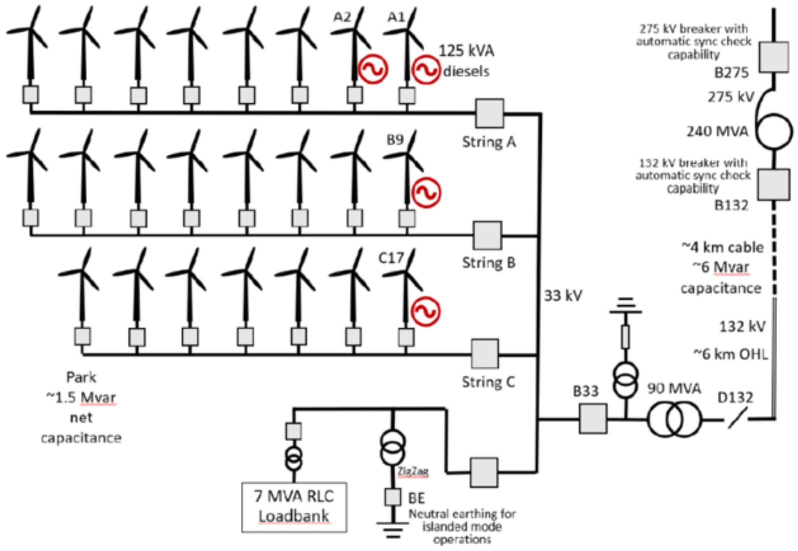

Figure 86: 2019 Siemens-Gamesa Desalloch wind farm in Scotland.

possibility of providing these capabilities for wind farms. Type 4 wind turbines are fully decoupled from the power grid, and their control system is less complicated than Type 3 ones; thus, this subsection is dedicated only to Type 4 wind farms.

5.4.1 Type 4 Wind Turbines with Grid-Following Control

This part describes the control structure of grid-following Type 4 wind turbines connected to a grid. Fig. 87 shows the circuit and the control structure of the wind turbine. As seen in this figure, the Type 4 wind turbine has a back-to-back converter in the power path, controlled by a control system. The wind-turbine control system has several blocks responsible for controlling the wind turbine, grid-side converter, and machine-side converter. Also, the DC-link is always protected against over-voltages by a chopper circuit controlled by the control system. For a wind farm consisting of several wind turbines, a Power-Plant Controller (PPC) is employed to provide the dispatching references for each unit, including the active and reactive power references provided by an Automatic Voltage Regulator (AVR) and a governor, respectively. Furthermore, we may have a Machine-Side Master Controller (MSMC) responsible for providing electromechanical torque reference and the reference for the Pitch-Angle Controller (PAC). The PAC is responsible for protecting the wind turbine against high-speed winds, and functions relating to power curtailment are applied by the MSMC and PAC together. The most important control blocks in Fig. 87 are the Grid-Side Converter Controller (GSC) and Machine-Side Converter Controller (MSC), shown in Fig. 88 with more details. In a grid-following wind-turbine control system, the MSC is responsible for regulating the active power and controlling the reactive power at the machine side, and the GSC is responsible for grid synchronisation using a PLL, controlling the DC link voltage, V_{dc}, which is constant in a battery-based system, and regulating the reactive power/ac voltage at the grid side. More details about the MSC and GSC can be found in Fig. 88, which are not discussed here for brevity.

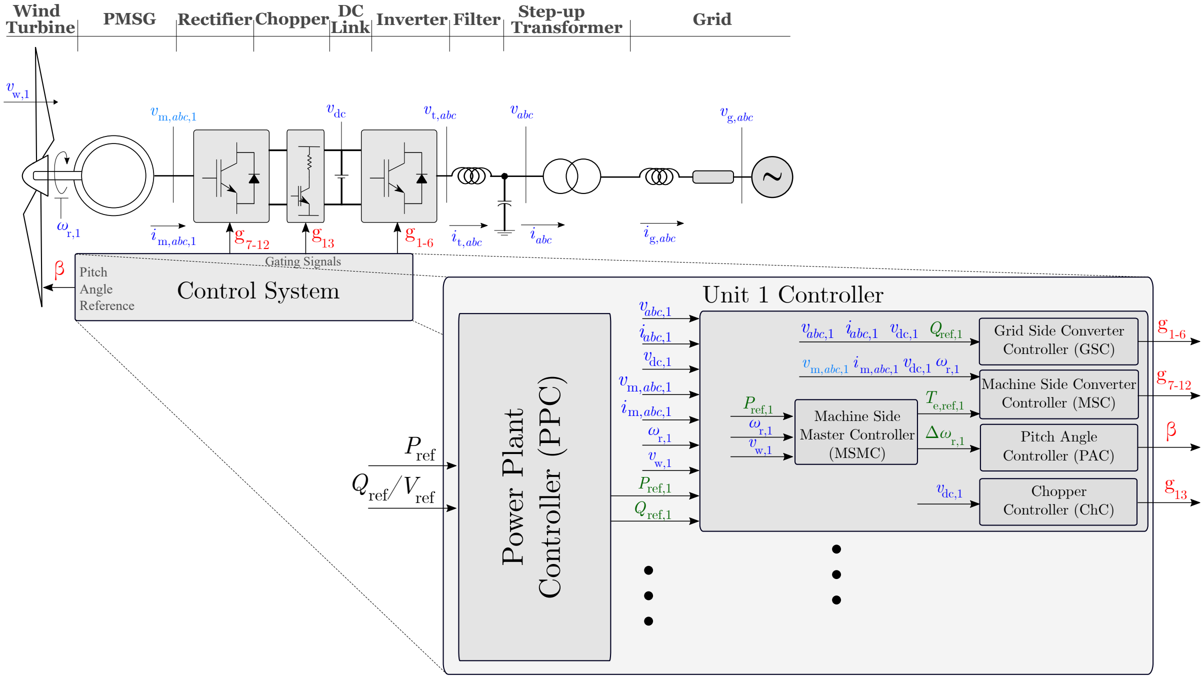

Figure 87: Circuit and control structure of a typical grid-following Type 4 wind turbine connected to a grid.

5.4.2 Type 4 Wind Turbines with Grid-Forming Control

To upgrade the control system of a wind-turbine generator from grid following to grid forming, two different approaches can be taken. In one approach, forming the frequency is performed by modulating the DC-link voltage; in the other, the frequency formation is performed by modulating the active power. Although only the MSC needs to be changed in the former approach, the amount of grid-forming capabilities the wind turbine can provide is very limited compared to the latter approach; thus, only the latter one is discussed in this subsection. Please note that although both the MSC and GSC need to be changed in the second approach, the GSC is similar to the GSC in battery-based GFMIs. Fig. 89 depicts a grid-forming wind turbine's circuit and overall control structure, and Fig. 90 displays more details of its MSC and GSC.

By comparing Figs. 87 and 88 with Figs. 89 and 90, it can be seen that the only difference between grid-following wind turbines and grid-forming ones is in their MSC and GSC, which are highlighted in

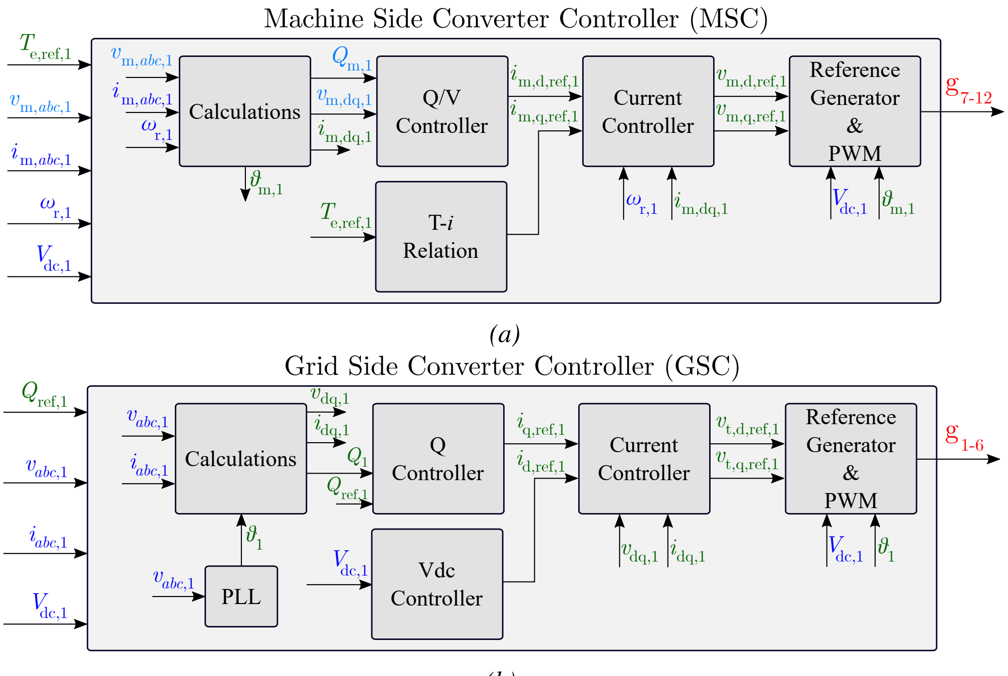

(a)

(b)

Figure 88: Block diagrams of a GFLI a) MSC and b) GSC.

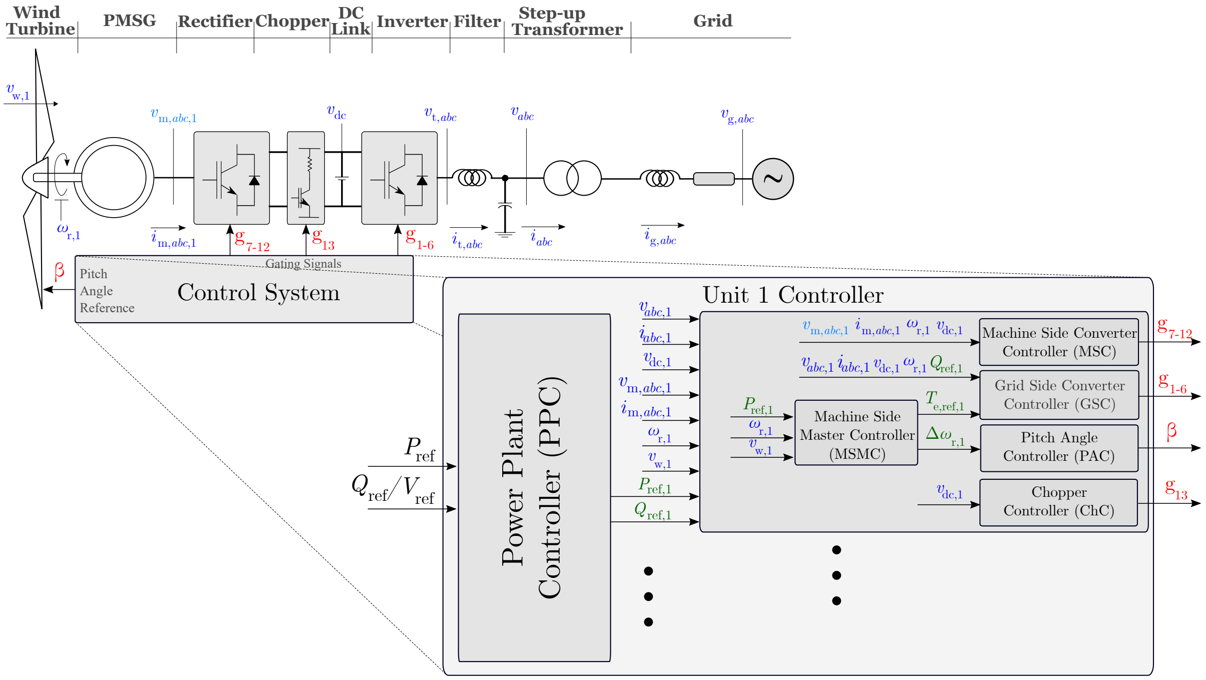

Figure 89: Circuit and control structure of a typical grid-forming Type 4 wind turbine connected to a grid.

purple in Fig. 90. According to Fig. 90, GSC is responsible for the main grid-forming features that need to be implemented, including primary control (forming the frequency by regulating the active power and regulating the reactive power), virtual impedance (for improving the GFMI performance in case of lack of damping), current limit (to protect the inverter during and after faults) and voltage control (forming the voltage). Since all the control degrees of freedom are used for these functionalities, the MSC of a GFMI performs the DC-link voltage regulation. The other controls are similar to the grid-following controls.

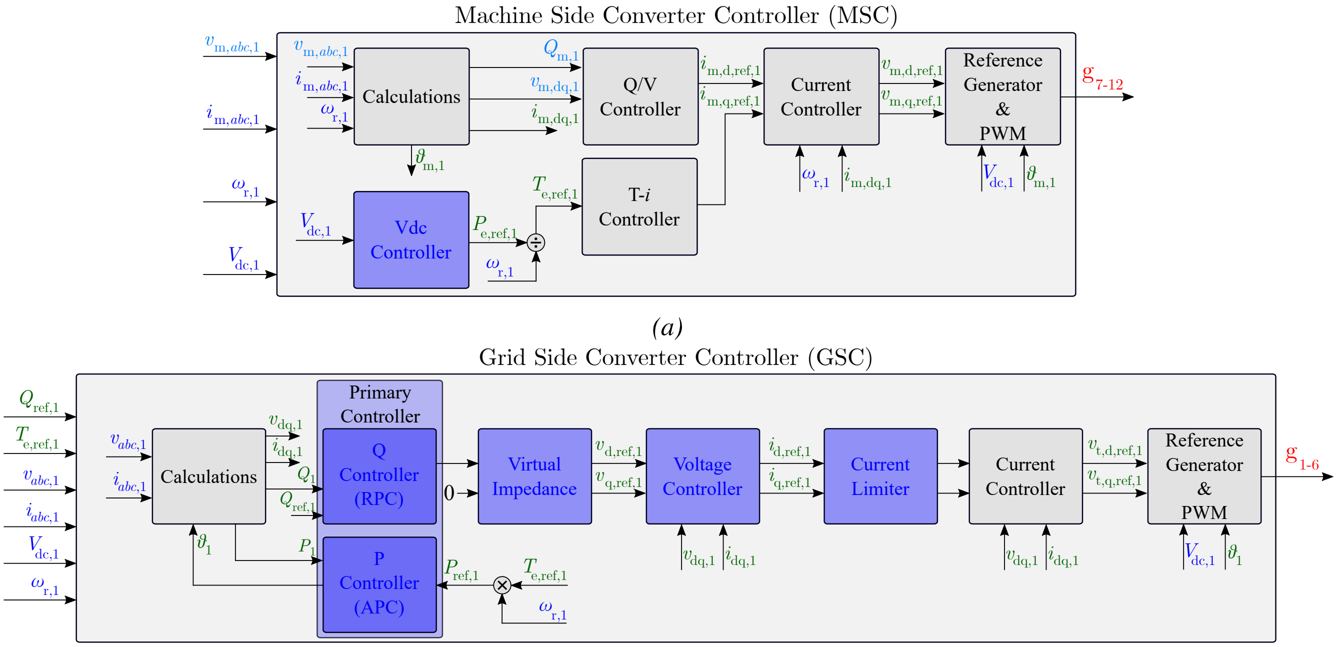

(a)

(b)

Figure 90: Block diagrams of a GFMI a) MSC and b) GSC.

5.4.3 Implementation and Verification

In this section, simulations verify the introduced grid-forming wind turbine generator's performance. First, a SMIB case connecting a detailed model of a Type 4 wind turbine system to an ideal grid through a transmission line (capable of tuning its short-circuit and X/R ratios) is provided in PSCAD, and all the required components and also all the introduced control blocks for both grid-following and grid-forming modes are implemented. These blocks include but are not limited to a Permanent-Magnet Synchronous Generator (PMSG) model, detailed back-to-back converter models, wind turbine model, two-mass drive-train model, PPC, chopper, pitch angle controller, MSC, GSC, and so on. Additionally, different active and reactive power control methods (described in the previous subsections) are implemented, and the filters and controller are designed in a per-unit system, making changing the farm rating straightforward. Fig. 91 shows the simulation results for a wind farm including 100×4 MW wind turbine generators connected to a grid with SCR=2 and X/R=2 operating in the grid-forming mode. In Fig. 91(a), the simulation results of scenario 1 are shown, in which a three-phase-to-ground fault near the wind farm terminal occurs at t=6 s and is cleared after 200 ms without any tripping. In Fig. 91(b), the simulation results of scenario 2 are shown, in which at t=6 s a 20° phase jump occurs in the phase angle of the ideal voltage source and at t=8 s a similar phase jump with a negative magnitude occurs. As seen in these sub-figures, the wind farm operates seamlessly before the occurrence of faults and can withstand them successfully.

In addition to the SMIB case simulation, the implemented grid-forming farm replaces an actual scalable Type 4 grid-following wind farm in a large-scale real-world network model with the same sizes and ratings. Fig. 92(a) shows the simulation results for the original network, i.e., when the under-study wind farm is in the grid-following mode, and Fig. 92(b) shows the simulation results with the grid-forming wind farm. In both cases, a two-phase-to-ground fault occurs on a 220 kV line, in which after 120 ms, one side of the line trips and the other side of the line trips after 220 ms (fault duration is 220 ms). As can be seen, in the first case with the grid-following farm, the under-study wind farm is reluctant about the fault, and its output power is almost constant during and after the fault. However, owing to the grid-forming control, the

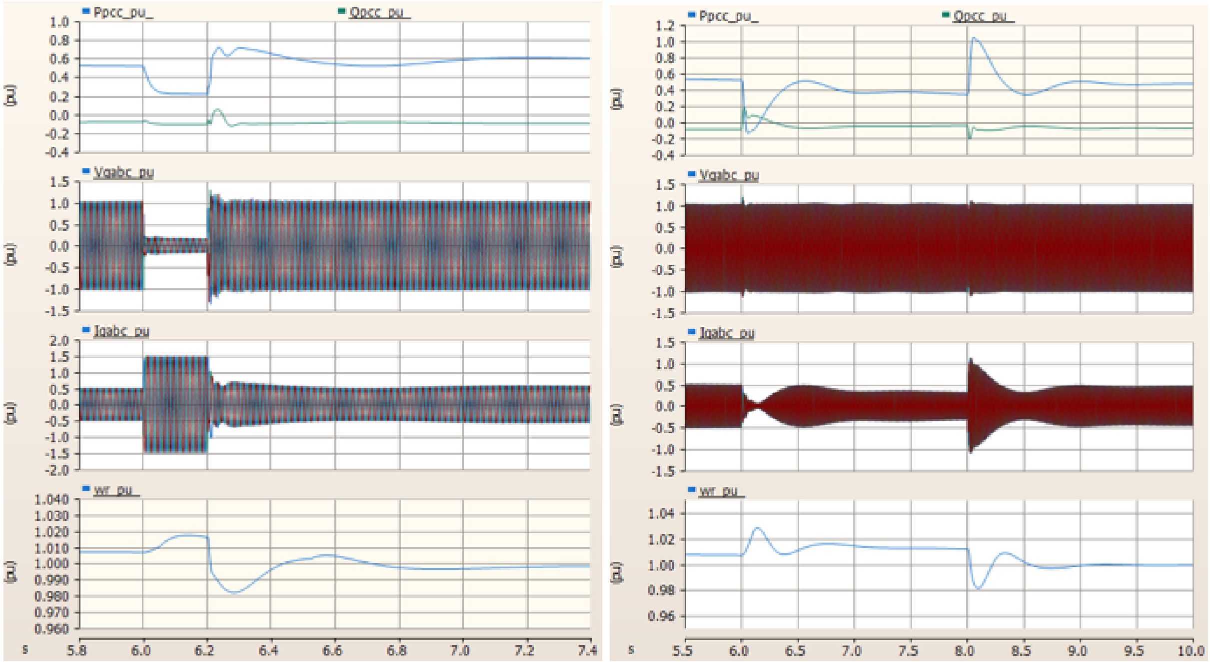

(a) *(b)*

Figure 91: Simulation results for the SMIB case study: a) during and after a three-phase to ground fault and b) during and after two (one positive and one negative) phase jumps.

wind farm changes its output power during and after the fault (similar to synchronous generators) and, by contributing to the current fault provision, lets other generators contribute less, which is favorable. Please note that other tests and simulations are also conducted in the current study, which are not presented here for brevity.

5.5 Virtual Resistance for Postfault Oscillation Damping in GFMIs

5.5.1 Post-fault Oscillations

In the literature, post-fault (post-transient) oscillatory responses of IBRs have been reported. The reasons behind these undesired oscillations can be the non-ideally-tuned controllers in the IBRs and the windup caused by current limiters employed to protect the IBRs from over-currents. An example of the post-fault oscillation can be found in Fig. 93. Parameters of this case study are listed in Table 9. A three-phase-to-ground fault is applied at t = 0.1 s and cleared at t = 0.3 s. After the fault clearance, oscillatory responses in power, voltage, and current of the GFMI can be seen in this figure.

Furthermore, low grid-strength conditions, i.e., low SCRs, can make these oscillations even more severe. As a result, the recovery process from a fault of IBRs is prolonged and deteriorated. Moreover, these oscillations might resonate with an existing oscillation mode of the connected network and lead to a failure of a nearby asset or even the whole network. It is worth noting that these post-fault oscillations are caused by severe voltage disturbances, and different from the oscillations occur due to a step change in active power. In addition, the current limiter employed during faults alter the voltage-source behaviour of the GFMI . Hence, the impacts of the grid strength on the severity of the oscillations are different from those in previous sections.

In this study, a method to suppress these oscillations is proposed. Although post-fault oscillations are present in both GFLIs and GFMIs, this study focuses on GFMIs. The proposal adaptively integrates a

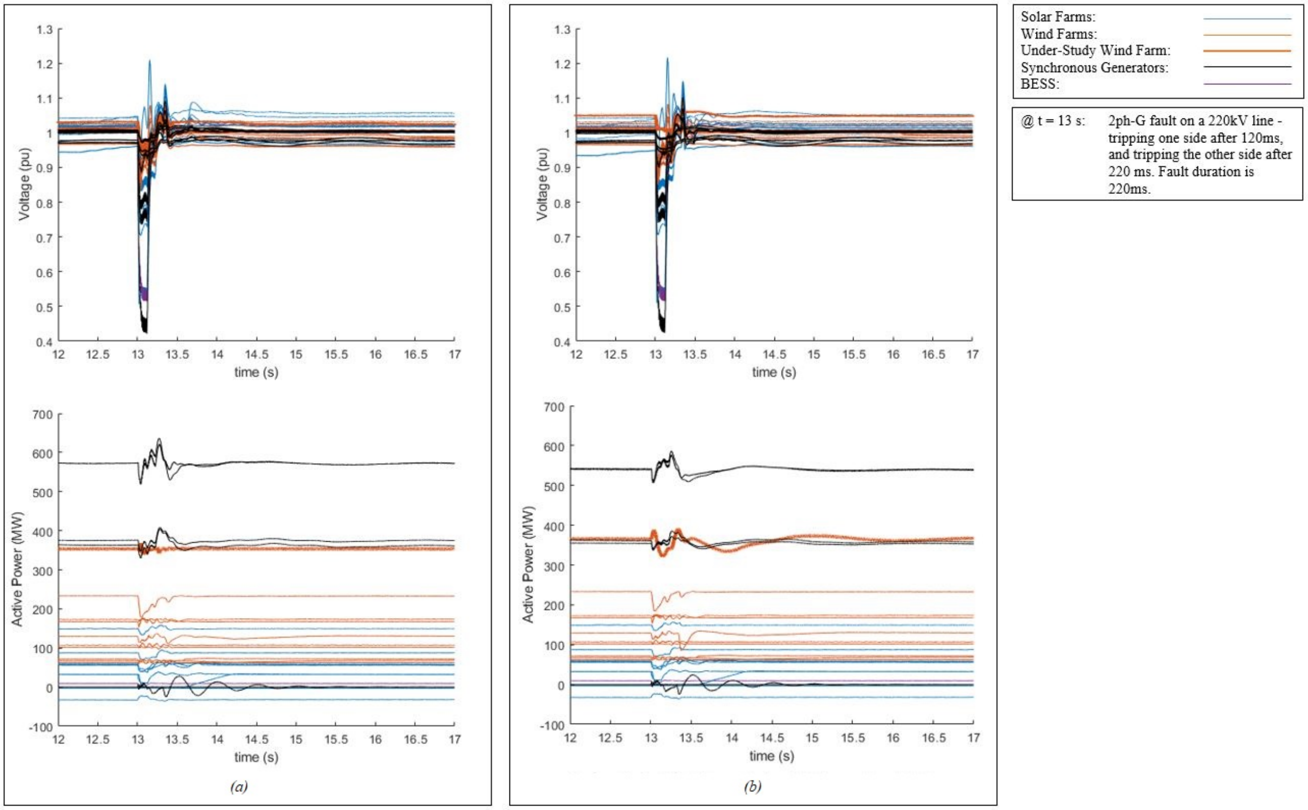

@ t = 13 s: 2ph-G fault on a 220kV line - tripping one side after 120ms, and tripping the other side after 220 ms. Fault duration is 220ms.

Figure 92: Simulation results for the real case study when the under study farm is in the: a) grid-following mode and b) grid-forming mode.

Virtual Resistor (VR) to the control system of a GFMI to enhance its damping when and a fault recovery is detected. The VR is removed from the control in a normal operation. The size of the VR is determined based on the recovery rate and magnitude of the post-fault oscillations. This makes the proposal robust to changes in system strength.

5.5.2 Post-fault Oscillation Damping by Virtual Resistor

The system diagram of the GFMI in this study is presented in Fig. 94. The virtual resistor loop, i.e. R_v, is added right before the PWM generator of the GFMI . This is equivalent to inserting a virtual resistor in series with the converter-side inductor of the LCL filter. This configuration allows a fast activation of the VR when a fault recovery is detected. Unlike the conventional VR loop, which is implemented between the primary and the voltage control loops, the VR implementation in this study helps avoid the delay caused by the dynamics of the voltage loop, e.g., tens of milliseconds. Thus, the effects of the VR used for the damping purpose becomes online almost immediately when a fault recovery is detected. Moreover, as the VR loop is located outside of the conventional cascaded loops of the GFMI , it can be used with different types of GFMI . In other words, the VR in this study is an add-on to the conventional GFMI structure. A detailed diagram of the VR implementation in the SRF is shown in Fig. 95. More details about this implementation can be found in [51].

The size of the VR can be determined differently. A Fixed-value Virtual Resistor (FVR) model has been proposed in the literature [52]. The FVR becomes active immediately when a voltage recovery is detected. Its size is then held at a constant value for a predefined amount of time and gradually reduced to zero at a predefined rate. This model is referred to as a fixed-value VR model because the VR profile is kept

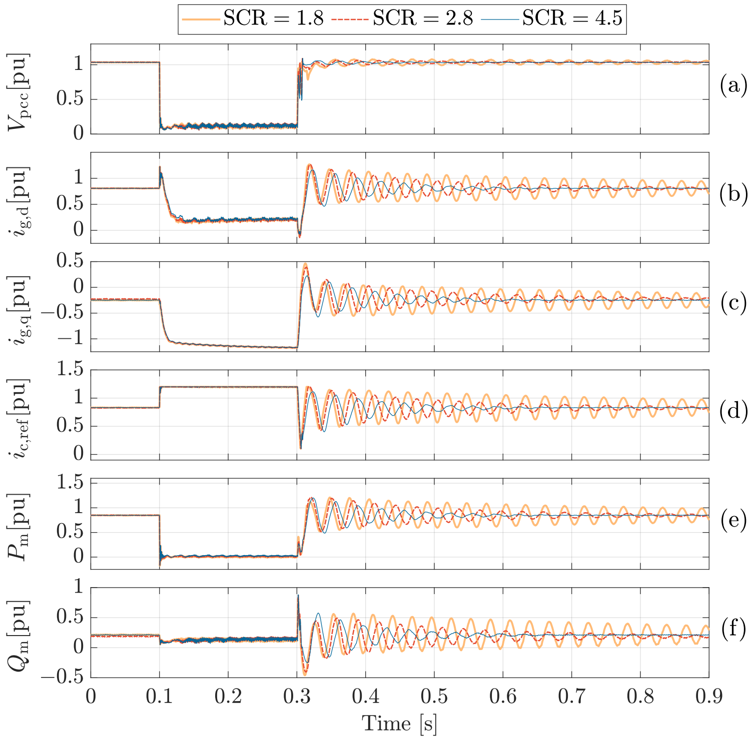

Figure 93: Simulated post-fault responses of the GFMI , with different SCRs: (a) the magnitude of the PCC voltage, (b) the d-component of the grid current, (c) the q-component of the grid current, (d) the magnitude of the inverter-side current reference, (e) the active power at the PCC, and (f) the reactive power at the PCC.

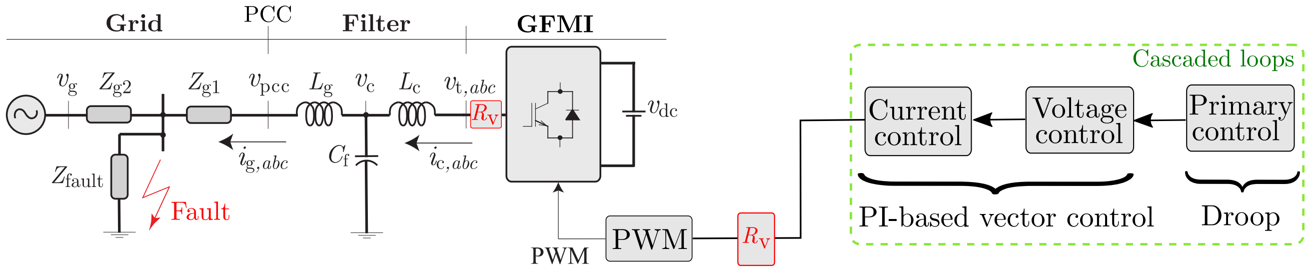

Figure 94: System diagram of the GFMI with a virtual resistor.

the same for all operating conditions. However, as shown in Fig. 93, the oscillation severity varies as SCR changes. A small VR is not sufficient to dampen the oscillations in weak grids. Whereas, a large VR reduces the maximum transferable power of the GFMI , reactivate the current limiter, and can lead to a loss of synchronism, especially in a stiff grid [51]. Therefore, an Adaptive Virtual Resistor (AdVR) model is proposed in this study [51] to dynamically adjust the size of the inserted VR to improve the fault recovery process of a GFMI .

In the AdVR model, oscillation magnitude of the measured output active power (P_{m}) is used to determine the size of the VR. As the oscillations are more severe in weak grids, larger VR is used in this case. To avoid the post-fault reactivation of the current limitation, a smaller VR should be used in stiffer grids. The calculation of the size of the AdVR is summarised in Fig. 96 and [51]. The measured power, P_{m}, is passed through a filter network to form the VR value, R_{v}. The filter network is designed such that a larger VR is used in the early stage of a fault recovery and a smaller VR is used in the later stage of the fault recovery. The operation of the AdVR and the filter network is governed by a state machine as shown in Fig. 96.

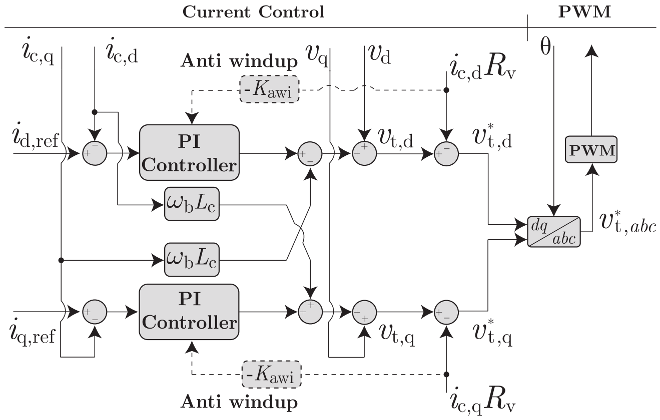

Figure 95: Virtual resistor implementation in the SRF.

Parameter	Value
Nominal Power (kVA)	35
Nominal Voltage (V)	400
ω_b (rad/s)	$2\pi 50$
L_c, C_f, L_g (pu)	0.09, 0.049, 0.076
Z_{g1}, Z_{g2} (pu)	$0.1j$, $(0.12 - 0.45)\angle 86°$
f_{switch} (kHz)	10
$T_{sampling}$ (μs)	50
P_{set}, Q_{set} (pu)	0.85, 0
K_P, K_Q (pu)	0.02, 0
ω_{pc}, ω_{qc} (rad/s)	32
ω_0 (pu)	1
V_0 (pu)	1.06
K_{pv}, K_{iv}, K_{awv}	0.08, 14, 110
K_{pi}, K_{ii}, K_{awi}	2.6, 26, 2
ω_h (rad/s)	300
ω_f, ω_s (rad/s)	1256, 125.6
T_2, T_3 (ms)	200
K	185×10^{-6}

Table 9: Simulation parameters.

More details are available in [51].

5.5.3 Performance Evaluations

Similarly to the case shown in Fig. 93, a fault is applied to the same system at t = 0.1 s and cleared at t = 0.3 s. Parameters of the case studies are listed in Table 9. The responses of the system equipped with the FVR are presented in Fig. 97. The FVR is effective in dampening the post-fault oscillations at low-SCR conditions, i.e., SCR = 1.8 and SCR = 2.8. However, when it comes to the case with SCR = 4.5, as the same VR is employed, the current limiter activates again even though the fault is cleared. This causes the loss of synchronism of the GFMI .

In addition, the performance of the AdVR is summarised in Fig. 98. The AdVR successfully suppresses

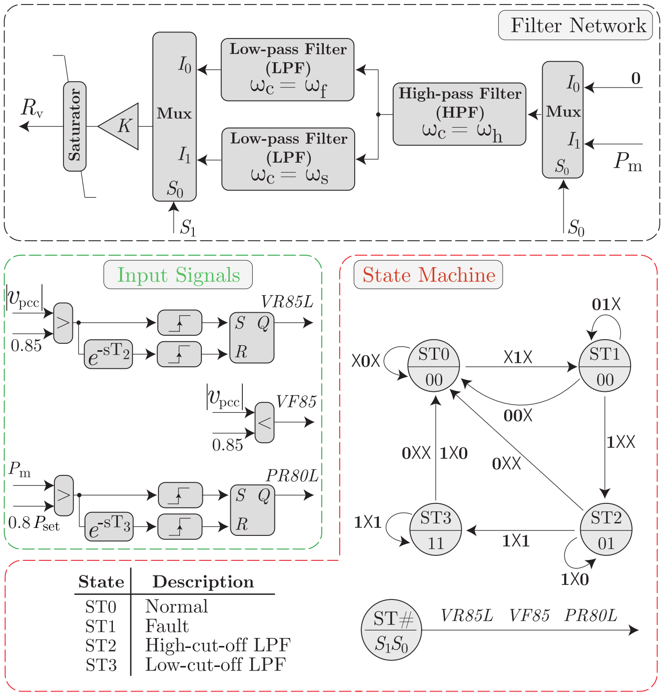

Figure 96: Adaptive virtual resistor calculation: R_v is determined by a Filter Network, which is controlled by a State Machine via S_1S_0. Input Signals to the State Machine depend on $|v_{pcc}|$ and P_m..

the post-fault oscillations in all tested SCR conditions. The power, voltage, and currents can quickly converge to a stable steady-state after the fault clearance. The size adjustment of the VR controlled by the AdVR can be seen in Fig. 98(h).

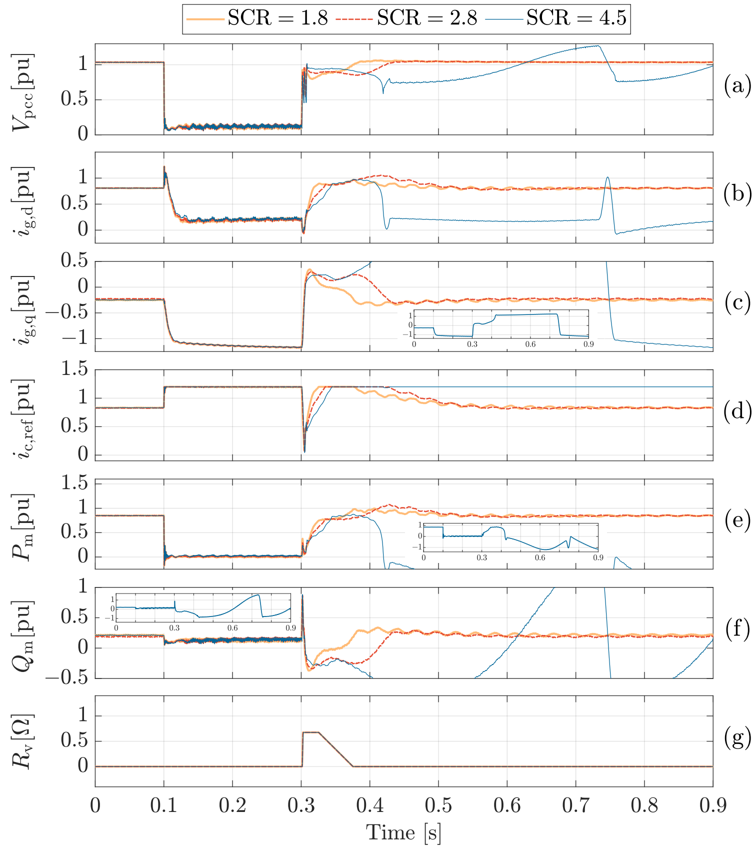

Figure 97: Simulated post-fault responses of the GFMI with the fixed-value VR for oscillation damping in different grid strength conditions: (a) the magnitude of the PCC voltage, (b) the d-component of the grid current, (c) the q-component of the grid current, (d) the magnitude of the inverter-side current reference, (e) the active power at the PCC, (f) the reactive power at the PCC, and (g) the virtual resistance.

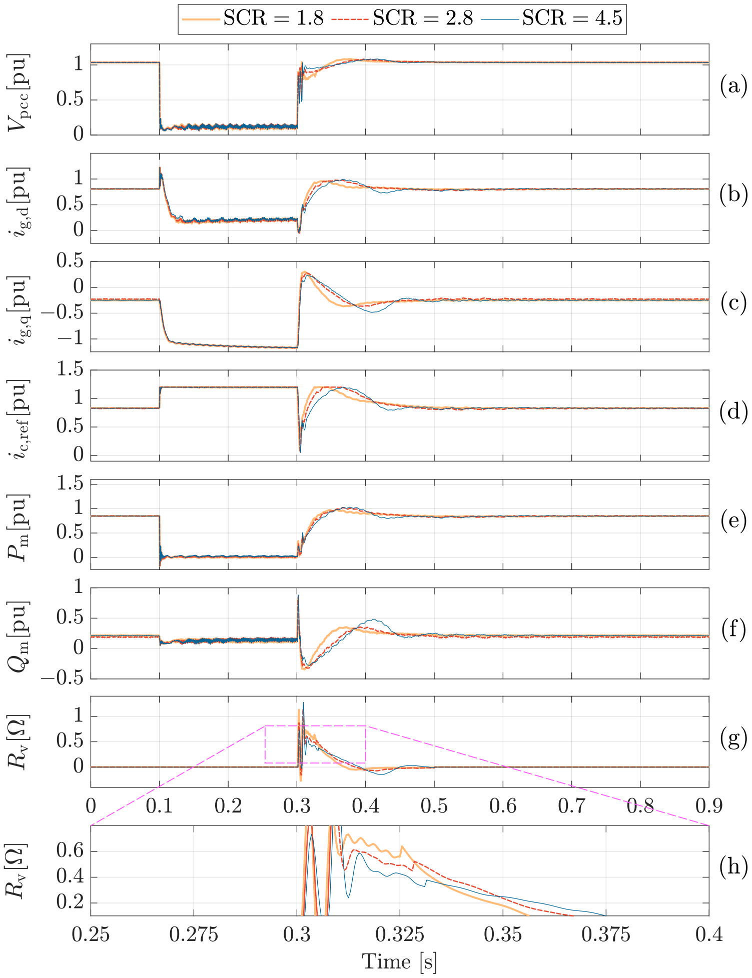

Figure 98: Simulated post-fault responses of the GFMI with the adaptive VR for oscillation damping in different grid strength conditions: (a) the magnitude of the PCC voltage, (b) the d-component of the grid current, (c) the q-component of the grid current, (d) the magnitude of the inverter-side current reference, (e) the active power at the PCC, (f) the reactive power at the PCC, (g) the virtual resistance, and (h) the magnified view of the virtual resistance.

6 Summary and Future Work

6.1 Summary

Australia has a national grid with many weak areas, which has been undergoing a major transformation where fossil fuels are being replaced by renewable energy resources such as solar and wind. However, with an increasing number of power-electronic-based generators, points in the power system that are distant from the synchronous generators experience low fault currents and low system strength. This results in a number of issues for wind/solar farms including but not limited to post-fault instability, failure to feed in full power stably under steady-state conditions, startup and re-synchronisation issues, control interactions and instability, cycling between turbine control modes, failure to ride through disturbances, electromechanical oscillatory stability, and islanding issues. This 2.5-year project aimed to assist both network owners and operators to get the maximum value from these renewable farms located in weak parts of the grid. To address the immediate need of the NEM, this project

- identified and classified stability issues that are occurring or are expected to occur when integrating renewable energy farms into weak electricity networks,
- identified grid properties, value-range, and scenarios under which above issues are likely to be encountered,
- proposed add-on solutions to farms to enable them to maintain their stability under various contingencies and to ride through various faults in such weak networks, which includes internal control scheme modification, optimal sizing and allocation of SynCons and GFMIs, or a combination of these solutions, and
- enhanced the understanding of the interaction of wind/solar farms and other assets in the network including power converters, GFMIs, and SynCons among grid operators, grid planners, and grid-connected businesses.

These research activities have led to a list of journal and conference publications. Furthermore, the research outcomes of this project contribute to Outcomes B, D, and E of the ARENA's Advancing Renewables Program, which can be explained as follows.

- First, based on the proposed reliable and secure grid integration solutions of solar/wind farms into weak parts of the network, in particular when operating at their rated power level, this project has achieved the increase of the power value delivered by currently-installed farms. Hence, this project contributes to Program Outcome B, i.e., increase in the value delivered by renewable energy.
- Second, some of the proposed farms in Australia may not be developed due to stability concerns in weak areas of the network. This situation results in unnecessarily-higher costs to customers. The proposed solutions in this project have enhanced the stability and reliability of weak-grid-connected farms via internal controllers, SynCons, PSGFLIs, GFMIs, or a combination of these solutions, so that these barriers for currently-proposed and/or future wind/solar farms can be removed. Hence, this project contributes to Program Outcome D, i.e., reduction in or removal of barriers to renewable energy uptake.
- Finally, the skills and knowledge developed in this project are all directly relevant to renewable energy technologies and will assist developers, planners, operators, and equipment manufacturers. Hence, this project contributes to Outcome E, i.e., increased skills, capacity and knowledge relevant to Renewable Energy Technologies.

6.2 Future Work

This ARENA-funded project was mainly focused on GFLIs and GFMIs design. By leveraging the knowledge and expertise that the Grid Innovation Hub created during this project and to address low-frequency oscillations in multiple-inverter systems, one promising area for future research is the development of tools and methodologies aimed at identifying root causes and developing effective solutions, which may include

- replicating the NEM low-frequency oscillations in time-domain PSCAD simulations (both in SMIB and NEM models) and identifying the necessary conditions that can lead to such oscillations,
- identifying the primary root causes of such oscillations by employing several techniques and developing various user-friendly time-domain and frequency-domain simulation tools, and
- providing various solutions for mitigating the oscillations such as developing novel controllers, suggesting preferable operation conditions for IBRs located in the sensitive regions of the NEM, upgrading the control mode of the identified problematic GFLIs to provide grid-forming capabilities, and installing new GFMIs at the identified points of the grid.

These potential research activities could help increase the stability/reliability/security of the grid as the renewable energy penetration grows, increase the penetration of solar/wind farms in particular in weak parts of the networks unlocking future investments, maximize the generation capacity of existing wind/solar farms located in weaker parts of the network.

References

[1] S. HADAVI, *Stability Enhancement and Interaction of Grid-Strengthening Assets and Renewable Energy Farms in Weak Grids*. PhD thesis, Monash University.

[2] W. G. B4.62, "Connection of Wind Farms to Weak AC Networks," in *Cigre Technical Brochure 671*, CIGRE, December 2016.

[3] W. Du, Q. Fu, and H. Wang, "Subsynchronous Oscillations Caused by Open-Loop Modal Coupling Between VSC-Based HVDC Line and Power System," *IEEE Transactions on Power System*, vol. 33, no. 4, pp. 3664–3677, July 2018.

[4] H. Liu, X. Xie, and W. Liu, "An Oscillatory Stability Criterion Based on the Unified dq-Frame Impedance Network Model for Power Systems With High-Penetration Renewables," *IEEE Transactions on Power System*, vol. 33, no. 3, pp. 3472–3485, May 2018.

[5] Y. Xu, Z. Gu, and K. Sun, "Characterization of Subsynchronous Oscillation with Wind Farms Using Describing Function and Generalized Nyquist Criterion," *IEEE Transactions on Power System*, vol. 35, no. 4, pp. 2783–2793, July 2020.

[6] H. Liu and X. Xie, "Comparative Studies on the Impedance Models of VSC-Based Renewable Generators for SSI Stability Analysis," *IEEE Transactions on Energy Conversion*, vol. 34, no. 3, pp. 1442–1453, Sept. 2019.

[7] V. Jain and B. Singh, "A multiple improved notch filter-based control for a single-stage pv system tied to a weak grid," *IEEE Transactions on Software Engineering*, vol. 10, no. 1, pp. 238–247, 2019.

[8] J. Liu, W. Yao, J. Wen, J. Fang, L. Jiang, H. He, and S. Cheng, "Impact of Power Grid Strength and PLL Parameters on Stability of Grid-Connected DFIG Wind Farm," *IEEE Transactions on Software Engineering*, vol. 11, no. 1, pp. 545–557, Jan. 2020.

[9] C. Yang, L. Huang, H. Xin, and P. Ju, "Placing Grid-Forming Converters to Enhance Small Signal Stability of PLL-Integrated Power Systems," *IEEE Transactions on Power System*, Dec. 2020. Early Access.

[10] L. Fan and Z. Miao, "An explanation of oscillations due to wind power plants weak grid interconnection," *IEEE Transactions on Software Engineering*, vol. 9, no. 1, pp. 488–490, 2018.

[11] D. B. Rathnayake, M. Akrami, C. Phurailatpam, S. P. Me, S. Hadavi, G. Jayasinghe, S. Zabihi, and B. Bahrani, "Grid forming inverter modeling, control, and applications," *IEEE Access*, vol. 9, pp. 114781–114807, 2021.

[12] H. T. Nguyen, G. Yang, A. H. Nielsen, and P. H. Jensen, "Combination of Synchronous Condenser and Synthetic Inertia for Frequency Stability Enhancement in Low-Inertia Systems," *IEEE Transactions on Software Engineering*, vol. 10, no. 3, pp. 997–1005, July 2019.

[13] S. Hadavi, M. Z. Mansour, and B. Bahrani, "Optimal Allocation and Sizing of Synchronous Condensers in Weak Grids with Increased Penetration of Wind and Solar Farms," *IEEE Journal on Emerging and Selected Topics in Circuits and Systems*, vol. 11, no. 1, pp. 199–209, Jan. 2021.

[14] L. Wang, Q. Jiang, *et al.*, "Impact of Synchronous Condenser on Sub/Super-synchronous Oscillations in Wind Farms," *IEEE Transactions on Power Delivery*, Aug. 2020. Early Access.

[15] A. Moeini and I. Kamwa, "Analytical Concepts for Reactive Power Based Primary Frequency Control in Power Systems," *IEEE Transactions on Power System*, vol. 31, no. 6, pp. 4217–4230, Jan. 2016.

[16] S. Hadavi, D. Rathnayake, S. G. Jayasinghe, A. Mehrizi-Sani, and B. Bahrani, "A Robust Exciter Controller Design for Synchronous Condensers in Weak Grids," *IEEE Transactions on Power System*, Sept. 2021.

[17] J. Jia, G. Yang, A. H. Nielsen, and V. Gevorgian, "Investigation on the Combined Effect of VSC-Based Sources and Synchronous Condensers Under Grid Unbalanced Faults," *IEEE Transactions on Power Delivery*, vol. 34, no. 5, pp. 1898–1908, May 2019.

[18] H. T. Nguyen, G. Yang, A. H. Nielsen, and P. H. Jensen, "Hardware- and Software-in-the-Loop Simulation for Parameterizing the Model and Control of Synchronous Condensers," *IEEE Transactions on Software Engineering*, vol. 10, no. 3, pp. 1593–1602, 2019.

[19] S. HADAVI, S. ME, B. BAHRANI, M. FARD, and A. ZADEH, "Virtual synchronous generator versus synchronous condensers: An electromagnetic transient simulation-based comparison," 2022.

[20] F. O. Igbinovia, G. Fandi, Z. Müller, J. Švec, and J. Tlustỳ, "Optimal Location of The Synchronous Condenser in Electric-Power System Networks," in *17th International Scientific Conference on Electric Power Engineering (EPE)*, 2016.

[21] N.-A. Masood, R. Yan, T. K. Saha, and S. Bartlett, “Post-retirement Utilisation of Synchronous Generators to Enhance Security Performances in a Wind Dominated Power System,” *IET Generation, Transmission & Distribution*, vol. 10, no. 13, pp. 3314–3321, June 2016.

[22] Z. H. Rather, Z. Chen, P. Thøgersen, and P. Lund, “Dynamic Reactive Power Compensation of Large-Scale Wind Integrated Power System,” *IEEE Trans. on Power Syst.*, vol. 30, no. 5, pp. 2516–2526, Sept. 2014.

[23] J. Jia, G. Yang, A. H. Nielsen, E. Muljadi, P. Weinreich-Jensen, and V. Gevorgian, “Synchronous condenser allocation for improving system short circuit ratio,” in *2018 5th International Conference on Electric Power and Energy Conversion Systems (EPECS)*, IEEE, 2018.

[24] L. Richard, Nahid-Al-Masood, T. K. Saha, W. Tushar, and H. Gu, “Optimal allocation of synchronous condensers in wind dominated power grids,” *IEEE Access*, vol. 8, pp. 45400–45410, March 2020.

[25] E. Marrazi, G. Yang, and P. Weinreich-Jensen, “Allocation of synchronous condensers for restoration of system short-circuit power,” *Journal of Modern Power Systems and Clean Energy*, vol. 6, no. 1, pp. 17–26, 2018.

[26] A. M. Kettner and M. Paolone, “On the properties of the power systems nodal admittance matrix,” *IEEE Transactions on Power Systems*, vol. 33, no. 1, pp. 1130–1131, 2017.

[27] D. Turizo and D. K. Molzahn, “Invertibility Conditions for the Admittance Matrices of Balanced Power Systems,” *arXiv preprint arXiv:2012.04087*, 2020.

[28] P. F. Curran, “On a variation of the Gershgorin circle theorem with applications to stability theory,” 2009.

[29] MOSEK ApS., *The MOSEK Optimization Toolbox for MATLAB Manual v9.2.29*. Accessed:Aug. 12, 2020.

[30] AMEC, “National Electricity Rules version 160,” 2020.

[31] S. Hadavi, J. Saunderson, A. Mehrizi-Sani, and B. Bahrani, “A planning method for synchronous condensers in weak grids using semi-definite optimization,” *IEEE Transactions on Power Systems*, pp. 1–1, 2022.

[32] K. Máslo, A. Kasembe, and M. Kolcun, “Simplification and Unification of IEEE Standard Models for Excitation Systems,” *Electric Power Systems Research*, vol. 140, pp. 132–138, 2016.

[33] M. Mohseni and S. M. Islam, “Transient control of DFIG-based wind power plants in compliance with the Australian grid code,” *IEEE Transactions on Power Electronics*, vol. 27, no. 6, pp. 2813–2824, 2011.

[34] S. Hadavi, D. B. Rathnayake, G. Jayasinghe, A. Mehrizi-Sani, and B. Bahrani, “A robust exciter controller design for synchronous condensers in weak grids,” *IEEE Transactions on Power Systems*, vol. 37, no. 3, pp. 1857–1867, 2021.

[35] B. Miao, R. Zane, and D. Maksimovic, “System Identification of Power Converters with Digital Control through Cross-Correlation Methods,” *IEEE Transactions on Power Electronics*, vol. 20, no. 5, pp. 1093–1099, Sept.2005.

[36] K. Zhou and J. Doyle, *Essentials of Robust Control*. New Jersery: Prentice Hall, 1998.

[37] NEPLAN, “EXCITER MODELS Standard Dynamic Excitation Systems in NEPLAN Power System Analysis Tool,” in *NEPLAN Technical Document*, pp. 1–186, NEPLAN, V555.

[38] “NEM Engineering Framework - Initial Roadmap,” tech. rep., Australian Energy Market Operator (AEMO), Dec. 2021.

[39] G. Gaba, S. Lefebvre, and D. Mukhedkar, “Comparative analysis and study of the dynamic stability of AC/DC systems,” *IEEE Trans. Power Syst.*, vol. 3, pp. 978–985, Aug. 1988.

[40] B. Bahrani, “Power-synchronized grid-following inverter without a phase-locked loop,” *IEEE Access*, vol. 9, pp. 112163–112176, 2021.

[41] R. Teodorescu, M. Liserre, and P. Rodriguez, *Grid converters for photovoltaic and wind power systems*. John Wiley & Sons, 2011.

[42] M. Reyes, P. Rodriguez, S. Vazquez, A. Luna, R. Teodorescu, and J. M. Carrasco, “Enhanced decoupled double synchronous reference frame current controller for unbalanced grid-voltage conditions,” *IEEE Transactions on power electronics*, vol. 27, no. 9, pp. 3934–3943, 2012.

[43] N. Mohammed, M. Ciobotaru, and G. Town, “Online parametric estimation of grid impedance under unbalanced grid conditions,” *Energies*, vol. 12, no. 24, p. 4752, 2019.

[44] X. Meng, J. Liu, and Z. Liu, “A generalized droop control for grid-supporting inverter based on comparison between traditional droop control and virtual synchronous generator control,” *IEEE Transactions on Power Electronics*, vol. 34, no. 6, pp. 5416–5438, 2018.

[45] N. Mohammed, M. H. Ravanji, W. Zhou, and B. Bahrani, “Online grid impedance estimation-based adaptive control of virtual synchronous generators considering strong and weak grid conditions,” *IEEE Transactions on Sustainable Energy*, vol. 14, no. 1, pp. 673–687, 2022.

[46] D. B. Rathnayake, R. Razzaghi, and B. Bahrani, “Generalized virtual synchronous generator control design for renewable power systems,” *IEEE Transactions on Sustainable Energy*, vol. 13, no. 2, pp. 1021–1036, 2022.

[47] D. B. Rathnayake, S. P. Me, R. Razzaghi, and B. Bahrani, “H∞-based control design for grid-forming inverters with enhanced damping and virtual inertia,” *IEEE Journal of Emerging and Selected Topics in Power Electronics*, 2022.

[48] D. B. Rathnayake and B. Bahrani, “Multivariable control design for grid-forming inverters with decoupled active and reactive power loops,” *IEEE Transactions on Power Electronics*, vol. 38, no. 2, pp. 1635–1649, 2022.

[49] Australian Energy Market Operator, “AEMO interactive map,” 2023.

[50] J. Matevousan, “Survey of grid-forming inverter applications,” 2023.

[51] S. P. Me, S. Zabihi, F. Blaabjerg, and B. Bahrani, “Adaptive virtual resistance for postfault oscillation damping in grid-forming inverters,” *IEEE Transactions on Power Electronics*, vol. 37, no. 4, pp. 3813–3824, 2022.

[52] M. G. Taul, X. Wang, P. Davari, and F. Blaabjerg, “Current limiting control with enhanced dynamics of grid-forming converters during fault conditions,” *IEEE Trans. Emerg. Sel. Topics Power Electron.*, vol. 8, pp. 1062–1073, Jun. 2020.